

# Distribution and dynamics of charged particle-induced DNA double-strand breaks

Vom Fachbereich Biologie der Technischen Universität Darmstadt  
zur Erlangung des akademischen Grades eines *Doctor rerum naturalium* genehmigte

## **Dissertation**

von  
Dipl.-Phys.

**Jörn Splinter**

aus Darmstadt

Berichterstatter: Prof. Dr. Marco Durante

Mitberichterstatter: Prof. Dr. Gerhard Thiel

Tag der Einreichung: 08.03.2010

Tag der mündlichen Prüfung: 11.05.2010

Darmstadt 2010

D 17



*"Two roads diverged in a wood and I,  
I took the one less traveled by,  
And that has made all the difference."*

Robert Frost



## Acknowledgement

First, I would like to thank Prof. Dr. Marco Durante for the opportunity to carry out this project in his department at the GSI and for his support and encouragement in the course of manuscript writing and editing. Further I want to thank Prof. Dr. Thiel for his assumption of the second opinion on this thesis.

I thank Dr. Gisela Taucher-Scholz to offer me the opportunity to work in her lab and for the supervision during the thesis together with Dr. Burkhard Jakob. I really appreciate the prolific work flow and think we made up a really good team.

I am thankful to the members of the Biophysics department, especially my colleagues of the DNA repair group, for the nice working atmosphere and their help. Sorry, for the efforts the unaware physicist put on your shoulders and thanks for the fun in beam-free beamtimes.

Dear Wolfgang, I'll give you a call when a cup of wisdom is needed.

Dear Anna Lena, please hold out cracking them up.

Dear Burkhard, thank you for the last 53 months. I have been a lucky guy to get such an advisor.

My deepest gratitude is to my girl-friend Nicole Staiber for her support, her encouragement and distraction. Thank you for being the way you are, especially for your appreciation.

This work is dedicated to my brother and parents.  
Ohne euch wäre das alles nicht gegangen. Danke...



## Summary

The efficient repair of DNA double-strand breaks (DSBs) is clearly decisive in determining the ‘fate’ of damaged cells, but the spatiotemporal organisation of repair events that might explain the formation of chromosomal misrejoining and genome instability is not yet clear.

Following generation of DSBs the histone variant H2AX is phosphorylated ( $\gamma$ H2AX) comprising megabase-pair regions of the chromatin around the DSB (Rogakou *et al.* 1998; Rogakou *et al.* 1999) that can be visualized by immunostaining. Irradiation of cell nuclei with charged particles leads to the spatially defined production of DSBs along the particle trajectory, thus facilitating studies on the dynamics of ionizing radiation-induced foci (IRIF) associated with lesion processing.

Microscopic imaging of ion-induced IRIF patterns in fixed and living cells revealed that lesion density has only a minor impact on the pattern and number of  $\gamma$ H2AX IRIF (Chapter Four) and showed a general positional stability of DNA lesions (Chapter Five), respectively.

The former finding demonstrates that the number of visualized IRIF following ion irradiation is below the amount expected for the applied doses and it was suggested that single IRIF might contain several damage sites corresponding to the high lesion density induced by ions (Jakob *et al.* 2003; Costes *et al.* 2007). We addressed this question using repair-related proteins forming smaller (micro-)foci compared to  $\gamma$ H2AX, but despite some  $\gamma$ H2AX IRIF containing multiple micro-foci its number was still lower than expected. Therefore, high-resolution 4Pi microscopy was applied (AG Hell, DKFZ Heidelberg) to resolve a potential substructure of micro-foci. However, a substructure was only observed for  $\gamma$ H2AX and 53BP1 signals, but not for the micro-foci forming repair-proteins RPA and hMre11 (Chapter Six).

Nevertheless, despite the restricted dynamic range of foci numbers following ion irradiation of different LETs the application of micro-foci marker allowed a rough estimation of the dose deposited by UVA laser microirradiation. For this laser-induced RPA IRIF patterns were compared with patterns induced by low angle ion irradiation (Jakob *et al.* 2003) of different LETs (Chapter Six). The laser dose was estimated to be in the range of hundreds of Gray.

As a further aspect of IRIF patterns an influence of chromatin structure on the foci positions was recently discussed by Costes *et al.* (2007) reporting a preferential localization of  $\gamma$ H2AX signals at the interface between regions of low and high intensive DNA staining. In agreement with the here described slow and confined damage motion (Chapter Five), these authors hypothesized that a potential small range damage translocation might occur. To elucidate such a dynamic process we used low angle and targeted single ion irradiation to induce DSBs spatially confined inside heterochromatic compartments in mammalian cells and analyzed the 3D geometry of induced  $\gamma$ H2AX and XRCC1 signals at different time point post-irradiation (Chapter Seven). We demonstrate that, contrary to the current notion, phosphorylation of H2AX is indeed possible within heterochromatin and that damage sites induced in the interior of heterochromatic compartments are expelled to the periphery within 20 min. We further show that this relocation is independent of ATM, a protein previously reported to be involved in the repair of heterochromatin-associated damages (Goodarzi *et al.* 2008).

Taken together, the here described results suggest that chromatin structure and not an repair-related directional mobility of damage sites is responsible for the preferentially localization of IRIF at the border of intensively stained chromatin regions and for the characteristic gap structure of ion-induced IRIF patterns.





## Zusammenfassung

Die effiziente Reparatur von DNA-Doppelstrangbrüchen (DSBs) ist entscheidend für das Schicksal beschädigter Zellen. Trotzdem ist die räumliche und zeitliche Organisation der Reparaturabläufe, die das Entstehen chromosomaler Fehlverknüpfungen und genomischer Instabilität erklären könnten, bisher nicht verstanden. Nach der Generierung von DSBs wird die Histonvariante H2AX in einem Megabasenpaar-Bereich um den Bruch zu  $\gamma$ H2AX phosphoryliert (Rogakou *et al.* 1998; Rogakou *et al.* 1999), das durch immunozytochemische Färbung sichtbar gemacht werden kann. Die Bestrahlung von Zellkernen mit geladenen Teilchen führt entlang der Teilchenbahn zu einer räumlich begrenzten Induktion von DSBs. Dies ermöglicht Untersuchungen zur Dynamik von DNA Schäden, die indirekt über  $\gamma$ H2AX oder andere akkumulierende Reparatur-relevante Proteine beobachtet werden.

Mikroskopaufnahmen dieser Akkumulationen (Foci) zeigen nach Ionen Bestrahlung charakteristische Muster in fixierten und lebenden Zellen. Wir zeigen hier, dass die Schadensdichte nur einen geringen Einfluss auf die Verteilung und Anzahl der  $\gamma$ H2AX Foci hat (Kapitel Vier) und die Position einer Schadensstelle generell stabil ist (Kapitel Fünf).

Ersteres demonstriert, dass die Anzahl beobachteter Foci nach Ionenbestrahlung unterhalb der Menge liegt, die bei entsprechend applizierter Dosis angenommen werden kann. Es wurde vorgeschlagen, dass entsprechend der hohen Schadensdichte entlang der Ionentrajektorie, einzelne Foci möglicherweise mehrere Schadensstellen enthalten (Jakob *et al.* 2003; Costes *et al.* 2007). Wir gingen dieser Frage nach, indem wir Reparaturproteine beobachteten, die im Vergleich zu  $\gamma$ H2AX kleinere (Mikro)foci bilden. Obwohl sich in manchen  $\gamma$ H2AX Foci mehrere Mikrofoci fanden, blieb auch die Mikrofocizahl hinter den Erwartungen zurück. Deswegen verwendeten wir hoch-auflösende 4Pi Mikroskopie (AG Hell, DKFZ Heidelberg), um eine potentielle Substruktur der Mikrofoci aufzulösen. Solch eine Substruktur konnte in  $\gamma$ H2AX und 53BP1 Signalen beobachtet werden, nicht jedoch in den Signalen der Mikrofoci-bildenden Reparaturproteine RPA und hMre11 (Kapitel Sechs).

Obwohl die Anzahl Ionen-induzierter Foci nur schwach von den jeweiligen LETs der Ionen abhängt, erlaubte die Verwendung von Mikrofoci-Markern eine grobe Abschätzung der deponierten Dosis bei UVA Laser Mikrobestrahlungen. Dafür wurden RPA Foci Muster verglichen, die entweder durch Laserbestrahlung oder Schmalwinkel-Bestrahlung mit Ionen unterschiedlicher LETs (Jakob *et al.* 2003) induziert wurden (Kapitel Sechs). Die abgeschätzte Laser-Dosis liegt im Bereich mehrerer hundert Gray.

Kürzlich wurde von Costes *et al.* (2007) ein Einfluss der Chromatinstruktur auf die Focipositionierung diskutiert. Dieser berichtete von einer bevorzugten Lokalisierung von  $\gamma$ H2AX Signalen am Übergang zwischen DNA Färbungen niedriger und hoher Intensität. Die Autoren nehmen an, dass in Übereinstimmung mit der hier beschriebenen langsamen und begrenzten Schadensbewegung (Kapitel Fünf), eine kurzreichweitige Schadenstranslokation stattfindet. Um einen solchen dynamischen Prozess zu verfolgen, benutzten wir Schmalwinkel- und Einzel-Ionen-Bestrahlung, die DSBs räumlich begrenzt innerhalb heterochromatischer Kompartimente induzieren. Wir analysierten die Geometrie induzierter  $\gamma$ H2AX und XRCC1 Signale zu verschiedenen Zeitpunkten nach der Bestrahlung von Säugerzellen (Kapitel Sieben). Die Ergebnisse zeigen, dass entgegen der weitläufigen Meinung, die Phosphorylierung von H2AX auch in Heterochromatin möglich ist, und dass Schadensstellen, die im Innern heterochromatischer Regionen generiert werden innerhalb von 20 min ausgestülpt werden. Dieser Prozess ist unabhängig von ATM, einem Protein, das in der Reparatur Heterochromatin-assoziiierter DNA Schäden involviert ist (Goodarzi *et al.* 2008).

Zusammengefasst deuten die hier beschriebenen Resultate darauf hin, dass die bevorzugte Lokalisierung der Foci am Rande stark gefärbter Chromatinregionen und die Lücken in Ionen-induzierten Focimustern nicht auf eine Reparatur-bezogene gerichtete Bewegung von Schadensstellen sondern auf die Struktur des Chromatins zurückzuführen sind.

Following publications are incorporated into this dissertation:

Jakob B, Splinter J and Taucher-Scholz G (2009) Positional stability of damaged chromatin domains along radiation tracks in mammalian cells. *Radiat. Res.* **171**:405-418.

Jakob B, Splinter J, Durante M and Taucher-Scholz G (2009) Life cell microscopy analysis of radiation-induced DNA double-strand break motion. *Proc. Natl. Acad. Sci. U S A* **106**:3172-3177.

Splinter J, Jakob B, Lang M, Yano K, Engelhardt J, Hell SW, Chen DJ, Durante M and Taucher-Scholz G (2010) Biological dose estimation of UVA laser microirradiation utilizing charged particle-induced protein foci. *Mutagenesis* (epub ahead of print).

Splinter J, Jakob B, Conrad S, Voss K-O, Zink D, Durante M, Löbrich M and Taucher-Scholz G (submitted to *Nat. Cell Biol.*) DNA lesions within heterochromatin induce phosphorylation of histone H2AX and are expelled to euchromatic regions.

## Table of contents

<b>Acknowledgement</b> .....	i
<b>Summary</b> .....	iii
<b>Zusammenfassung</b> .....	v
<b>Table of contents</b> .....	vii
<b>Abbreviations</b> .....	ix
<hr/>	
<b>Section A – Introduction</b> .....	1
Chapter One: Ionizing radiation .....	3
Chapter Two: DNA damage induction and repair .....	7
Chapter Three: Motivation .....	11
<hr/>	
<b>Section B – Spatiotemporal analysis of charged particle-induced DNA damages</b> ...	14
Chapter Four: Spatial distribution of damage signals induced by low energy carbon and uranium ions .....	17
Chapter Five: Life cell microscopy of ion-irradiated cells describes the positional stability of damage sites .....	37
<hr/>	
<b>Section C – Application of ion-induced foci patterns and their dynamic behavior within heterochromatin</b> .....	52
Chapter Six: Biological dosimetry of UVA laser microirradiation based on the comparison of DNA damage patterns .....	55
Chapter Seven: DNA lesions within heterochromatin induced phosphorylation of histone H2AX and are expelled to euchromatic regions .....	73
<hr/>	
<b>Bibliography</b> .....	85
<b>Curriculum vitae</b> .....	93
<b>Eidesstattliche Erklärung</b> .....	95



## Abbreviations

1BR3	normal human fibroblast cell line
53BP1	p53-binding protein 1
AG1522	normal human fibroblast cell line
ATM	ataxia telangiectasia mutated
BSA	bovine serum albumin
DMEM	Dulbecco's modified Eagle medium
DNA	Deoxyribonucleic acid
DNA-PKcs	catalytic subunit of the DNA protein kinase
DSB	DNA double-strand break
EBSS	Earle's balanced salt solution
Alpha/D/EMEM	Alpha/Dulbecco's/Eagle's minimum essential medium
FCS	fetal calf serum
FCS2	Focht chamber system 2
GFP	green fluorescent protein
$\gamma$ H2AX	histone variant H2AX phosphorylated at Ser139
Gy	Gray
H2A(X),H2B,H3,H4	histone variants
H3-K9met3	histone H3 three times methylated at its lysine 9
HeLa	human cell line derived from a cervical adenocarcinoma
(h)Mre11	MRE11 mutants exhibit defective meiotic recombination (h – human)
HR	homologous recombination
HZE	high charge and high energy
IR(IF)	ionizing radiation(-induced foci)
KAP-1	KRAB domain-associated protein 1
LDE	laser dose equivalent
LET	linear energy transfer
LMI	laser microirradiation
LSS	Lindhard-Scharf-Schott
MDC1	mediator of DNA damage checkpoint protein 1
MEF	murine embryonic fibroblast
MSD	mean square displacement
NBS1	Nijmegen breakage syndrome 1
NHEJ	non-homologous end joining
RPA	replication protein A
RPMI	cell medium named after Roswell Park Memorial Institute
p-ATM	phosphorylated ATM
PCNA	proliferating cell nuclear antigen
PMMA	Polymethylmethacrylate
SEM	standard error of the mean
Ser139	C-terminal serine of H2AX
SSB	single-strand break
<i>STD</i>	radial spreading parameter
TRF1 / 2	telomeric repeat-binding factor 1 or 2, respectively
U2OS	human osteosarcoma cell line
UV(A)	ultraviolet (A)
XRCC1	X-ray repair cross complementation protein 1
YFP	yellow fluorescent protein



## Section A

### **Introduction**

#### **Chapter One:**

Ionizing radiation (p. 3)

#### **Chapter Two:**

DNA damage induction and repair (p. 7)

#### **Chapter Three:**

Motivation (p. 11)





## Chapter One

### Ionizing radiation

In the decay of unstable atomic nuclei, radiation is released in form of electromagnetic waves ( $\gamma$ -rays) or subatomic particles ( $\beta$ - and  $\alpha$ -particles). If this radiation transfers enough energy to liberate electrons from target atoms it is referred to as ionizing radiation. The basic unit for ionizing radiation is the dose, measured in Gray (Gy) that is defined as the radiation energy absorbed per mass unit of the irradiated matter:  $1 \text{ Gy} = 1 \text{ J/kg}$ .

Beside the process of atomic decay ionizing radiation can be artificially produced e.g. in X-ray tubes resulting in photon irradiation with lower energy compared to  $\gamma$ -rays. Alternatively, atoms can be ionized and accelerated in electric fields that allow particle irradiation similar to  $\alpha$ -particles but with higher energies and a variety of ion species.

Depending on the energy deposition, ionizing radiation is either sparsely (X- and  $\gamma$ -rays) or densely ionizing (charged particles) with a low or high linear energy transfer (LET), respectively. The LET ( $\text{keV}/\mu\text{m}$ ) gives the energy deposited by a particle per unit penetration length and is derived from the calculation of particle energy loss.

#### 1.1 Spatial distribution

Since the energy of a single particle is much higher compared to a single photon, particles induce more ionization events and therefore many  $\delta$ -electrons. For that reason such kind of radiation is called densely ionizing. In contrast, photon radiation (X- and  $\gamma$ -rays) is called sparsely ionizing radiation, because a single photon with sufficient energy reacts only in a single ionization event. I.e., the same amount of energy is applied either by a few charged particles as illustrated in Fig. 1-1a or by many photons resulting in a homogeneous energy distribution (Fig. 1-1b).

#### 1.2 Charged particle irradiation

According, to the inhomogeneous dose distribution of charged particles the applied doses are difficult to interpret. The mean dose deposited in a certain area is proportional to the number of traversals within the given area (Fluence;  $F$ ), the energy deposited per particle and track length (linear energy transfer;  $LET$ ) and the reciprocal target density ( $1/\rho$ ):

$$D [\text{Gy}] = 1.619 \cdot 10^{-9} \cdot LET [\text{keV}/\mu\text{m}] \cdot F [\text{cm}^{-2}] \cdot (1/\rho) [\text{cm}^3/\text{g}]$$

However, for the calculation of the energy deposition in the center of the particle track its specific energy and energy loss  $dE/dx$  have to be considered.

The specific energy of accelerated charged particles is reduced when the ion encounters matter. This energy reduction happens successively by many single interactions in which typically low amounts of energy are transferred and the particle mainly interacts with the electrons of the surrounding matter in ionization events ('electronic stopping'). For high ion energies ( $> 10 \text{ MeV/n}$ ) the energy loss is given by Bethe-Bloch formula (Bethe 1930; Bloch 1933). Ongoing interaction events reduced the energy and, accordingly, the velocity of the ion. Therefore, electron capture occurs and the effective charge of the ion is reduced (Barkas 1963). As a consequence, the frequency of ionization events and the amount of energy

transferred per event is also retarded. This energy region (0.1 – 10 MeV/n) is called Lindhard-Scharf-Schott (LSS) region in which energy loss is proportional to the ion velocity in units of lightspeed  $\beta = v/c$ . For energies below 0.1 MeV/n ions begin to interact with whole atomic nuclei of the target material and the amount of energy transferred per interaction event dramatically increases (nuclear stopping).

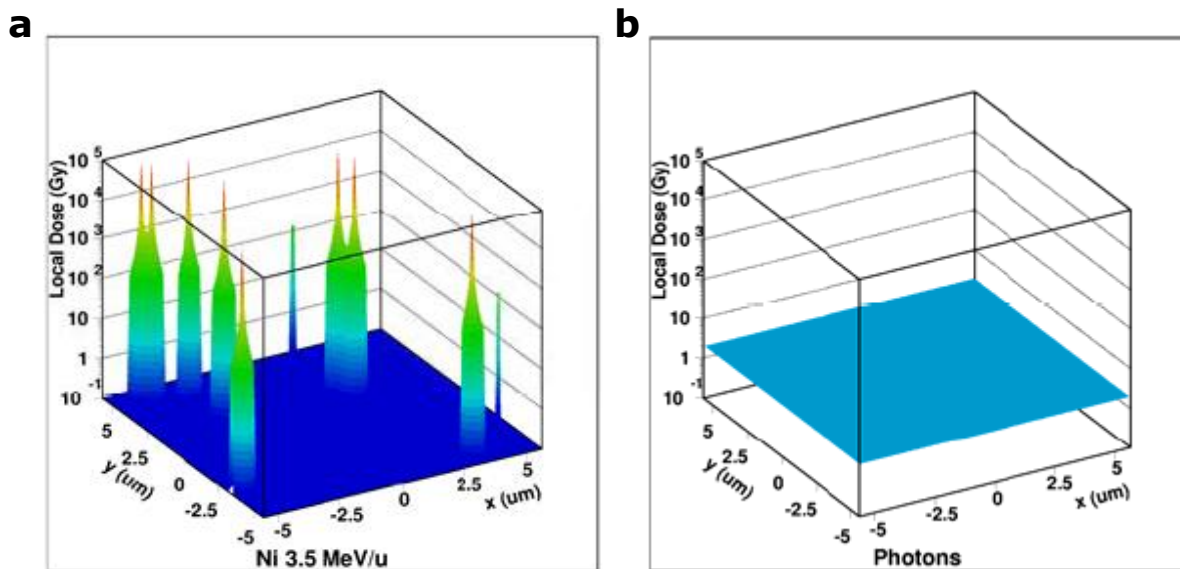


**Fig. 1-1.** Simulated distribution of a deposited dose of 2 Gy following either low-energy Ni-ion irradiation (a, inhomogeneous dose distribution) or sparsely ionizing radiation (b, homogeneous dose distribution). Local doses are additionally visualized using different colors.

(pictures were kindly provided by Dr. Michael Scholz, GSI, Darmstadt)

### 1.3 Application of accelerated charged particles

In the following applications for ion irradiation are described that can be distinguished in the research fields of cancer therapy (carbon tumorthrapy) and cancer risk (human space exploration). For both fields irradiation of cell monolayers were accomplished as also described here.

#### **Tumorthrapie and human space exploration**

The initial specific energies of ions used in tumor therapy irradiation are typically in the range of a few hundreds of MeV/n. Thus, their energy loss can be described by the Bethe-Bloch formula. The formula describes an increase of the energy loss with decreasing specific energy ( $10^1 - 10^4$  MeV/n) resulting from an increase in reaction time when the velocity of the ion is reduced. According to this correlation the dose-depth profile of charged particles is inverted compared to photons. In Figure 1-2 two so-called Bragg curves for different energies of carbon ions are shown. The curves represent the relative deposited energy in different depths in water. For comparison the energy deposition of photons of different energies are also depicted. The graph clearly demonstrates the advantage of charged particles in the precision of dose deposition in depth and legitimates its application in the treatment of tumors surrounded by critical organs.

These graphics also demonstrate that high energy charged particle can easily penetrate material and efficient shielding is needed to stop particles. Efficient shielding in the case of heavy ions is typically accomplished by materials of high density. Such kind of heavy shielding materials cannot be used in outer space, since weight is critical in the design of vehicles for space exploration. Hence, artificial charged particles produced in ion accelerators are a tool to test newly developed shielding materials and to study cellular responses on the galactic cosmic radiation.

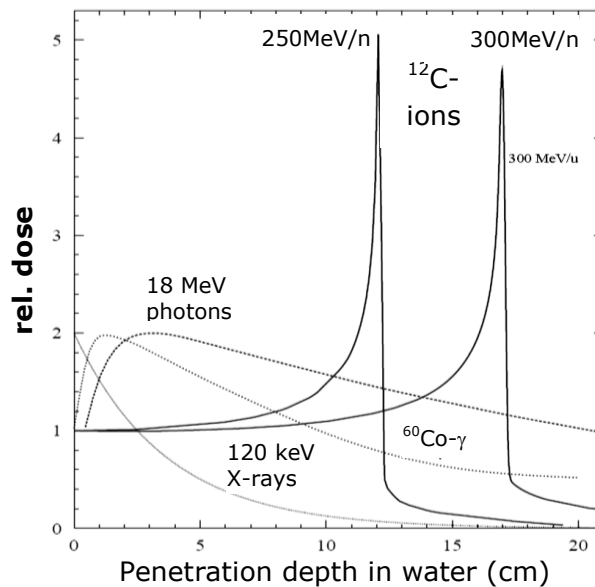


**Fig. 1-2.** Bragg curves of carbon ions with given specific energies in comparison to the dose deposition of photons of different energies.

(picture: Kraft 2000)

### Irradiation of cells

As a further application, charged particles are used as a tool to induce DNA lesions very localized within cell nuclei. The spatially confined induction of damages and the geometry of linear ion tracks enable the spatiotemporal analysis of cellular damage response processes. Especially for the typically irradiated mono cell layers the energy loss of the penetrating particles is assumed to be constant. In that case the energy loss is called linear energy transfer (LET) describing the deposited energy per unit track length ( $\text{keV}/\mu\text{m}$ ).

According to the high amount of ionization events along the ion trajectory, a nucleus traversed by ions contains irradiated and non-irradiated regions as schematically shown in Fig. 1-3. A magnified view on the ion track reveals the already shown distribution of ionization and  $\delta$ -electron production events, but for a comparison of  $\delta$ -electron range and the dimensions of the most critical target a schematic drawing of the DNA double helix is added. The actual ionization of the DNA molecule happens either directly by primary or secondary ionization products of the projectile (typical for densely ionizing radiation) or indirectly by hydrolysis and the production of diffusing radicals (the major process for sparsely ionizing

radiation). Both mechanisms have the potential to induce DNA double-strand breaks (DSBs) the most critical DNA lesion.

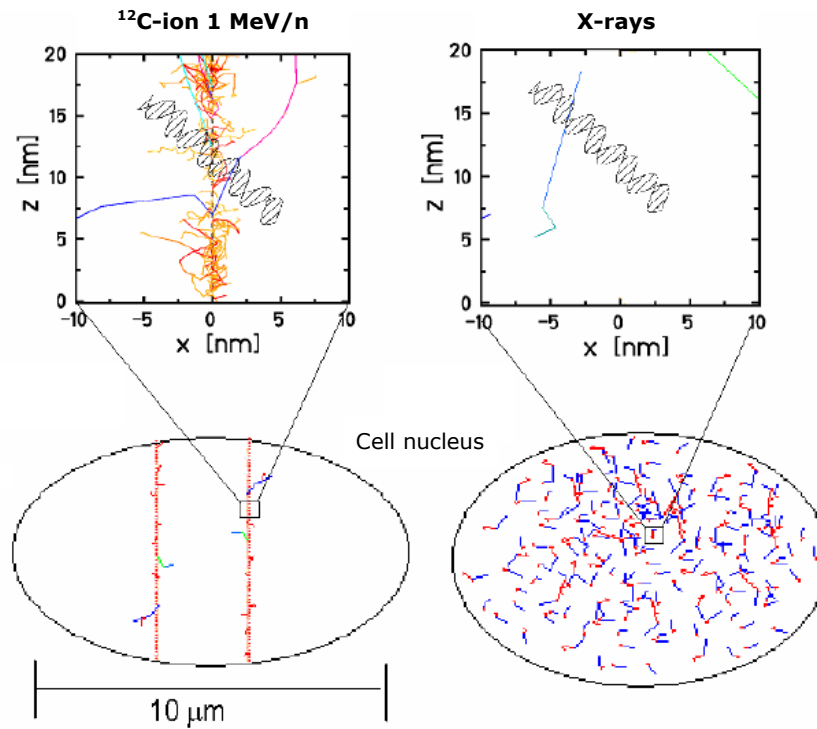


**Fig. 1-3.** Comparison of densely and sparsely ionizing radiation in terms of the distribution of ionization events within the nucleus. Magnified images of the simulated  $\delta$ -electron trajectories are illustrated together with the DNA double-helix demonstrating the higher probability of clustered DNA damages following ion irradiation.

(pictures were kindly provided by Dr. Michael Krämer and Dr. Michael Scholz, both GSI, Darmstadt)

## Chapter Two

### DNA damage induction and repair

Since DNA is the most critical part in living matter when exposed to ionizing radiation, cells which are not able to repair the DNA correctly, cannot sustain the genomic stability and mutations accumulate. In addition to exogenously induced DNA damages also several thousands of spontaneous damages per day frequently occur (Friedberg 1995). To preserve genomic stability and efficient repair cells possess several pathways to repair the different lesion types (reviewed in Sancar *et al.* 2004). Therefore, damages were detected by specific sensor proteins initiating the corresponding repair pathway by activating and stabilizing other repair proteins.

#### 2.1 Types of ionizing radiation-induced DNA damages

It has been estimated that low-LET radiation creates approximately 40 DSBs, 1000 single-strand breaks and 2700 base damages per Gray in a mammalian nucleus (Ward 1988, Ward 1995; Newman *et al.* 2000; Jenner *et al.* 2001). Densely ionizing radiation induces similar numbers of DSBs (Heilmann 1995), but lesions are closer together forming “clustered DNA damage” with higher complexity (Fig. 2-1) (Ward 1994; Goodhead 1994; Rydberg *et al.* 1994). The repair of these clustered DNA damages is shown to be more difficult (Taucher-Scholz *et al.* 1996).

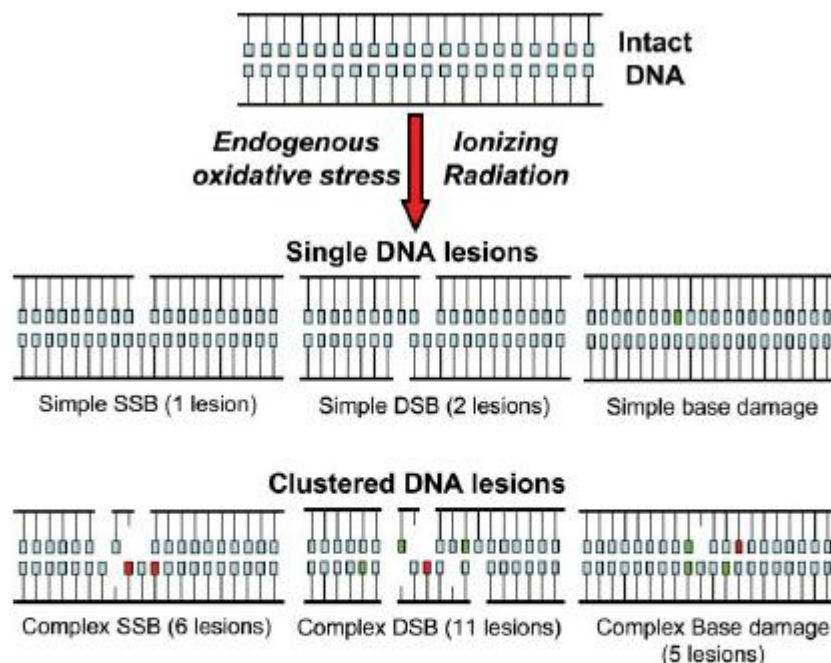


**Fig. 2-1.** Examples of single and complex DNA lesions induced by ionizing radiation or endogeneous oxidative stress. Light squares denote undamaged bases. Damage to individual nucleotides comprise missing or damaged (red squares) bases and strand breaks (accompanied by base loss). As shown many neighboring lesions can accompany SSBs or DSBs (complex DNA lesions).

(picture: Georgakilas 2008)

In the case of DSB repair, when loose DNA ends have to be ligated, pathway choice is not solely determined by the lesion type, but also by cell cycle phase. In S- and G2-phase the repair pathway of homologous recombination (HR) using sequences of the newly replicated sister chromatids for error-free DNA repair, act redundantly to non-homologous endjoining (NHEJ) (reviewed by Jackson 2002). The latter repair pathway is cell-cycle-independent (Hinz *et al.* 2005) and error-prone, since no homologous template is used and DNA sequences get lost in the course of DSB end processing that is necessary for its ligation. Additionally, NHEJ might rejoin wrong DSB ends, especially if several DSBs are proximate to each other.

The ability of cells to repair DSBs appears to depend on the proximity, distribution and number of the ionization. Recently, a further factor was added to this impact factors: chromatin density (Falk *et al.* 2007; Goodarzi *et al.* 2008).

## 2.2 Chromatin organization

DNA is compacted in several steps: first 146 base-pairs of DNA are wrapped around the histone octamer forming the 10nm-fibre. The octamer consist of twice of the histones H2A, H2B, H3 and H4 each. Higher-order chromatin structures as the 30nm-fibre result from further winding. In metaphase nuclei the highest level of compaction is achieved when 46 chromosomes, comprising the diploid human genome of 6 billion base-pairs, form their typical x-shaped structure. However, most of the time the cell is in interphase in which chromatin is less densely compacted.

Even in this relaxed chromatin state, single chromosomes occupy defined nuclear volumes (chromosomal territories; reviewed in Cremer & Cremer 2001). The spatial distribution of these distinct territories within the nucleus appears to be dependent on the gene density of the respective chromosome in spherical nuclei (Boyle *et al.* 2001; Küpper *et al.* 2007) and its size in nuclei with ellipsoidal shape (Sun *et al.* 2000). Furthermore, heterochromatic and gene-poor chromatin regions were typically found at the periphery of the nucleus and around the nucleoli forming “sub-chromosomal foci” (Ferreira *et al.* 1997; Zink *et al.* 1998; Sardoní *et al.* 1999). The distribution of chromosomal territories is shown in Fig. 2-2 using R-, G- and C-bands from mitotic chromosome staining to distinguish between transcriptionally active, euchromatic (R-band) and gene-poor, heterochromatic (G- and C-bands) regions.

In murine embryonic fibroblasts (MEFs) pericentromeric heterochromatin compartments are comparably large forming so-called chromocenters (Guenatri *et al.* 2004) that are easily visible following DNA staining or immunocytochemical staining for H3-K9me3, a marker for constitutive heterochromatin (Fig. 2-3). This histone modification is a conserved in mammalian cells defining heterochromatic regions. In addition, acetylation of histones is reduced in these compartments. While the latter modification is correlated to the closer positioning and therefore higher condensation of adjacent nucleosomes, the methylation motif appears to function as an anchor for other heterochromatin associated proteins like HP1 (Bannister *et al.* 2001). The grade of condensation is supposed to influence the accessibility of transcription factors (Horn & Peterson 2002) supported by the fact that facultative heterochromatin is formed to silence gene transcription. That heterochromatic chromatin is, in addition late replicating, might also be due to its dense structure and a hindered accessibility.

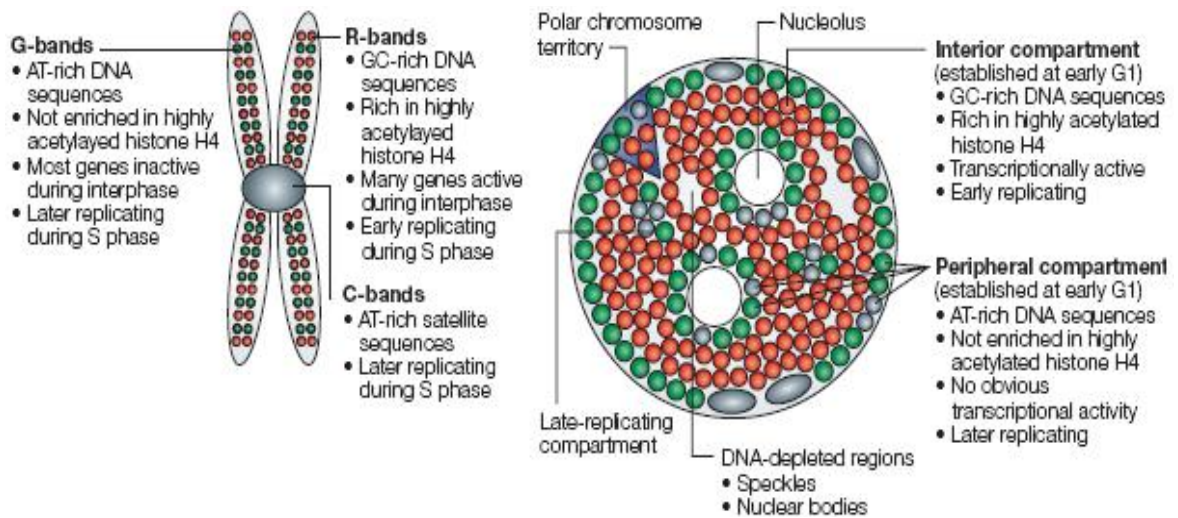


**Fig. 2-2.** Nuclear genome organization. The alternating arrangement of different mitotic chromosome bands and their specific features are shown for their chromosomal (left panel) and nuclear (right panel) position. R-band (red dots), G-band (green dots) and C-bands sequences (grey spheres).

(picture: Zink *et al.* 2004)

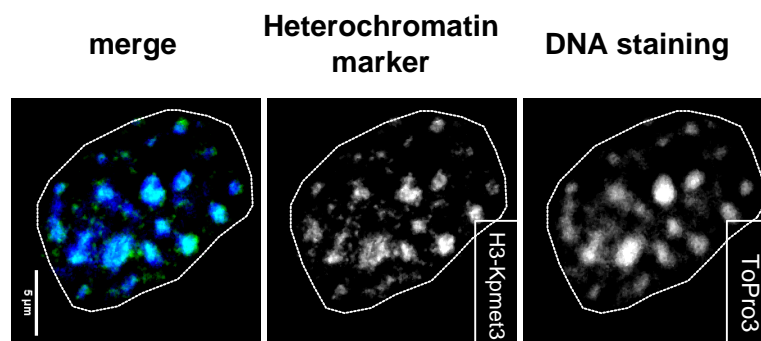


**Fig. 2-3.** Defining pericentromeric heterochromatin. MEF nucleus after fixation and immunostaining for H3-K9met3 (green) a marker specific for constitutive heterochromatin. Upper panels: Split channels for DNA (ToPro3) and H3-K9met3 signal. Bottom panel: Image of the merged signals revealing the co-localization of regions with intense DNA staining (blue) and the heterochromatin marker (green).

(our own data)

### 2.3 DNA damage within heterochromatin

Despite the compaction of DNA on either the nucleosome- or higher order level, its accessibility has to be assured for transcription and replication. For both processes, chromatin has to be relaxed and unwrapped from their histone scaffold. Different chromatin remodeling complexes are known to act in companion with transcription factors and the replication machinery. Such chromatin remodellers as SWI/SNF and INO80 are also reported to act in the repair of DNA (Downs *et al.* 2007). It is supposed that chromatin remodeling facilitate access of repair factors to the damage site. However, according to the current knowledge (Cowell *et al.* 2007; Goodarzi *et al.* 2009), repair factors are not able to access highly compacted heterochromatin, since in mammalian cells no  $\gamma$ H2AX damage signals could be observed within heterochromatic regions 1h after sparsely ionizing radiation (Kim *et al.* 2007; Cowell *et al.* 2007; Vasireddy *et al.* 2009). Nevertheless, following UVA laser microirradiation higher-order chromatin exhibit a local and damage-induced relaxation (Kruhlak *et al.* 2006) and recently, the general accessibility of compacted chromatin was demonstrated (Bancaud *et al.* 2009). A model suggested by Falk *et al.* (2007) accommodate the damage-induced chromatin relaxation and the exclusion of damage signals from dense chromatin considering the relaxation as a fast process followed by localization of damage signals adjacent to dense chromatin regions that remain condensed at later times following damage induction.

In addition to the question of accessibility, damages associated to heterochromatic regions in murine and human cells were demonstrated to repair in an ATM- (Goodarzi *et al.* 2008) and 53BP1-dependent (Noon *et al.* 2010), respectively. In both studies the retarded repair of heterochromatin-associated damages was abolished under KAP-1 knock-down conditions. The role of KAP-1 in heterochromatic DNA repair was previously shown by Ziv *et al.* (2006).



## Chapter Three

### Motivation

DNA double-strand breaks are one of the most deleterious types of DNA damage. Even more detrimental is DNA damage generated by low energy charged particles, because it combines DSBs with additional lesions in so-called multiple damage sites due to the dense spacing of ionization events (Ward 1994; Goodhead 1994; Krämer & Kraft 1994). Comparatively little is known about the spatiotemporal organization of repair events after generation of DSBs, although these events are clearly decisive in determining the ‘fate’ of the damaged cells. In fact, the interaction of DNA lesions leads to chromosomal aberrations, which are eventually responsible for early and late cellular effects. Understanding of lesion processing following charged particles is of great interest for particle therapy, where protons or C-ions are used to treat solid cancers (Schulz-Ertner & Tsujii 2007), and for radiation protection in space, because charged particles are present in the cosmic radiation and represent a major risk for human space exploration (Cucinotta & Durante 2006; Durante & Cucinotta 2008).

Our aim is to shed light on the spatiotemporal organization of the DNA repair mechanism. For that purpose we used charged particle irradiation as a tool to generate a localized and strictly linear channel of ionization that leads to spatially confined production of DNA damage along the particle trajectory (Jakob *et al.* 2003). As a consequence of damage induction, DNA damage-associated proteins accumulate forming ionizing radiation-induced foci (IRIF) whose dynamics can be monitored during the process of DNA repair.

Although local damage induction can also be achieved by laser microirradiation (reviewed by Lukas *et al.* 2005 and Taucher-Scholz & Jakob 2007), the physical nature of laser damage generation has still to be elucidated, whereas charged particle interactions are well-defined and, except for their spatial distribution, similar to the interactions of sparsely ionizing radiation (X- or  $\gamma$ -rays). Furthermore, the density of DNA lesions can be calculated according to the energy and charge of the particle used (Jakob *et al.* 2003). This is not possible for laser microirradiation that lack reliable dose calculations.

Following generation of DSBs the nucleosomal histone variant H2AX is phosphorylated at its C-terminal serine (Ser139) comprising megabase-pair regions of the chromatin around the DSB (Rogakou *et al.* 1998; Rogakou *et al.* 1999). Phosphorylated H2AX ( $\gamma$ H2AX) can be detected within minutes after DSB induction and it serves as a platform for the recruitment and retention of other repair-related proteins such as 53BP1, NBS1 and MDC1 (Celeste *et al.* 2002; Celeste *et al.* 2003; Ward *et al.* 2003; Stewart *et al.* 2003). Alternatively, the phosphorylation of H2AX modifies the surrounding chromatin and thus indirectly facilitates the accumulation of repair proteins (Fernandez-Capetillo *et al.* 2003). These IRIF involving larger DNA regions has been classified as “DSB flanking chromatin”-type (macrofoci), whereas proteins considered to be bound directly to the vicinity of the DNA lesion or subsequent processing stages (like single-stranded DNA) form smaller “microcompartments” (microfoci) (Bekker-Jensen *et al.* 2006). Overall, the distribution and dynamics of chromatin define the spatiotemporal organization of DNA repair events, which can be followed by these focal markers. Recently, a limited ‘movement’ associated with local chromatin decondensation and protrusion of DSBs into the low-density chromatin was described after local UV-laser (Krulak *et al.* 2006) or  $\gamma$ -irradiation (Falk *et al.* 2007). Aten *et al.* (2004) discussed the

formation of repair clusters containing several DSBs after linear track  $\alpha$ -particle irradiation requiring substantial motion of damaged chromatin sites. This motion might facilitate a long-range homology search, but at the same time it could contribute to the formation of tumorigenic chromosome translocations. In contrast, experiments using focused ultrasoft X-rays (Nelms *et al.* 1998) or single DSBs (Soutoglou *et al.* 2007) revealed apparently immobile DSBs. As a possible explanation, DSBs were suggested to be embedded in a dense cloud of adhesive  $\gamma$ H2AX domains that prohibited movement (Aten *et al.* 2004). The different views of repair-associated chromatin motion were reviewed recently (Soutoglou & Misteli 2007).

The major questions addressed in this PhD thesis were derived from the experiments described in Chapter Four and Five. In these chapters the influence of lesion density on  $\gamma$ H2AX formation and the mobility of damaged chromatin sites were analyzed after exposure to high-LET ionizing radiation. For the former analysis, cells were irradiated with ions of different charge and mass but similar low specific energy to keep the radial extension of the track small and fairly constant. Cells were irradiated at low angle (Jakob *et al.* 2003) so that induced IRIF patterns representing the linear tracks of traversing ions were easy to visualize. Beside other parameters fixed samples were analyzed for the distance between the distinct IRIF (**Chapter Four**). The latter analysis uses live cell imaging of cells transfected with a fluorochrom-tagged repair protein and irradiated with ions either at low angle (observation time up to 12 h) or perpendicular to the cell layer (short term observation directly after irradiation) (**Chapter Five**). The obtained results raise further questions, two of which are addressed in this PhD thesis: i) Do  $\gamma$ H2AX IRIF exhibit a substructure and ii) what influences the positioning of IRIF along the ion traversal?

The former question arises, because the number of ion-induced IRIF was below the expected amount calculated for the applied doses (calculation: Jakob *et al.* 2003). According to a previous report of Costes *et al.* (2007) comparing simulated IRIF positions with patterns following 1 GeV/n Fe-ion irradiation, single IRIF might contain several damage sites corresponding to the high lesion density induced by ions. We addressed this question using repair-related proteins forming smaller (micro-)foci compared to  $\gamma$ H2AX, but even though some  $\gamma$ H2AX IRIF contained multiple micro-foci, as also reported by Falk *et al.* (2007) following  $\gamma$ -irradiation, the overall micro-focus number was still lower than expected. Therefore, high-resolution 4Pi microscopy was applied in collaboration with AG Hell of the DKFZ (Heidelberg) to resolve a potential substructure of RPA and hMre11 micro-foci. However, a substructure was only observed for  $\gamma$ H2AX and 53BP1 signals revealing that the original damage site marked by a micro-focus is surrounded by several compartments stained for  $\gamma$ H2AX or 53BP1 that were even smaller than the micro-focus (**Chapter Six**).

Although ion-induced IRIF pattern showed only slight deviations after ion irradiation with different LETs, we compared such patterns with patterns following local UVA-laser microirradiation (UVA-LMI) to estimate the local dose applied by laser irradiation (**Chapter Six**). Unfortunately, a direct measurement of the absorbed laser energy fails due to the thin target of cell monolayers and the low absorption rate of DNA at wavelengths used in most LMI systems (Sutherland & Griffin 1981). Furthermore, the so far applied approaches yielded locally applied laser doses between 10 Gy (Bekker-Jensen *et al.* 2006) and 800 Gy (calculated by Paull *et al.* 2000). Motivated by these extreme differences in estimates of the laser dose equivalent (LDE), we revisited the idea of a previously established biological dosimetry in

which the numbers of X-ray- and laser-induced RPA foci were compared to define an X-ray equivalent laser dose (Bekker-Jensen *et al.* 2006). Beside X-rays, we used charged particles of different species as an ionizing reference radiation. In order to account for the non-homogeneous dose distribution of LMI and charged particles, the volume in which the RPA foci were counted was restricted to the irradiated part of the nucleus. According to our previous findings of the restricted dynamic range of IRIF patterns the resulting dose-response curve for charged particle-induced RPA foci saturated and the local LDE could not be accurately determined. However, the locally applied LDE can be estimated to be comparable to or even higher than the dose delivered by high-LET U-ions. Further evidence for a high LDE was achieved by recruitment studies of the telomere repeat-binding factors TRF1 and TRF2 both showed local accumulation after LMI as reported previously for TRF2 (Williams *et al.* 2007; Bradshaw *et al.* 2005), but no significant recruitment after Xe-ion irradiation.

The further question addressed in this thesis was motivated by the characteristic gaps observed between the foci of single ion track, despite the high lesion density within the track. In addition, a chromatin structure-dependent localization of IRIF was reported recently (Costes *et al.* 2007; Falk *et al.* 2007): Costes *et al.* (2007) described a non-random distribution of repair-related proteins in human epithelial cells after exposure to 1 GeV/n Fe-ions or  $\gamma$ -rays. IRIF were found preferentially at the interface of different chromatin densities in the nucleus and, as a rationale, the authors suggest a rapid, short range translocation of damage sites consistent with the here described slow diffusion-driven motion (**Chapter Five**), but influenced in its direction by chromatin density. Similar results of an exclusion of damage signals from condensed chromatin regions were reported for  $\gamma$ H2AX in human (Cowell *et al.* 2007, Vasireddy *et al.* 2009, Noon *et al.* 2010) and murine (Kim *et al.* 2007; Goodarzi *et al.* 2008; Noon *et al.* 2010) cell lines following sparsely ionizing radiation. To explain these observations it was suggested that the accessibility of the responsible kinases to these highly compacted chromatin regions might be hindered (Cowell *et al.* 2007; Goodarzi *et al.* 2009). However, in a recent study dextrans of a size comparable to DNA-PKcs and ATM were shown to access chromocenters (Bancaud *et al.* 2009). Thus, the reason for the exclusion of  $\gamma$ H2AX signals from heterochromatic regions is currently unclear. We addressed early damage response processes within constitutive heterochromatin using the GSI single ion microprobe that allows targeted irradiation and localized induction of DSBs within murine chromocenters. We show that, in contrast to the current notion, H2AX is indeed phosphorylated within this highly compacted chromatin regions. Moreover, we observed the subsequent relocation of the damage site from the center to the border of irradiated chromocenters (**Chapter Seven**).

Most interestingly, recent studies describe a retarded (Falk *et al.* 2008, Noon *et al.* 2010) and ATM-dependent (Goodarzi *et al.* 2008) repair kinetic for IRIF associated with heterochromatic compartments in human and murine cell lines and similar results were obtained by our collaboration partners (AG Löbrich, TU Darmstadt) after carbon ion irradiation of wild-type and ATM knock-out MEF cells. However, even under ATM knock-out conditions the relocation of damages from the interior to the periphery of chromocenters could still be observed. Finally, we hypothesized that lesion movement is physically driven by entropic forces resulting from an observed local chromatin decondensation at the damage site in the center of still condensed chromocenters.

## Section B

### **Spatiotemporal analysis of charged particle-induced DNA damages**

#### **Chapter Four:**

Spatial distribution of damage signals induced by low energy carbon and uranium ions

- Introduction (p. 17)
- Material and methods (p. 19)
- Results (p. 21)
- Discussion (p. 32)

#### **Chapter Five:**

Live cell imaging of ion-irradiated cell describes a positional stability of damage sites

- Introduction (p. 37)
- Material and methods (p. 39)
- Results (p. 41)
- Discussion (p. 49)

## Section abstract

Irradiation of cell nuclei with charged particles leads to the spatially defined production of DNA damage along the particle trajectories, thus facilitating studies on the dynamics of radiation-induced protein foci associated with lesion processing. Here we used visual inspection and computational analysis of the track morphology after immunodetection to describe the patterns of formation of  $\gamma$ H2AX foci and the repair-related proteins 53BP1 and RPA. We addressed the influence of lesion density on  $\gamma$ H2AX formation and the mobility of damaged chromatin sites by using low-angle irradiation of cell monolayers with low-energy carbon or uranium ions. We show the discrete formation of  $\gamma$ H2AX foci and the recruitment of repair-related proteins along ion trajectories over an LET range from 200 to 14300 keV/ $\mu$ m in human fibroblasts and in HeLa cells. The marked DSBs exhibited a limited mobility that was independent of the LET. The moderate extent of mobility in human fibroblasts pointed to a relatively stable positioning of the damaged chromatin domains during repair, in contrast to HeLa cells, which showed significant changes in the streak patterns in a fraction of cells, suggesting greater mobility in the local processing of DSBs. Our data indicate that the presence of single or multiple DSBs is not associated with an altered potential for movement of damaged chromatin. We infer that the repair of high-LET radiation-induced DSBs in mammalian cells is not coupled to an increased motional activity of lesions enhancing the probability of translocations. Nevertheless, data derived from fixed samples have severe limitations for tracking the dynamical behaviour of repair events, thus making the analysis of dynamic changes difficult. To circumvent these limitations, we studied the spatiotemporal organization of DNA damage processing by live cell microscopy analysis in human cells. In unirradiated U2OS osteosarcoma and HeLa cancer cells, a fast confined and Brownian-like motion of DNA repair protein foci was observed, which was not altered by radiation. By analyzing the motional activity of GFP-53BP1 foci in live cells up to 12 h after irradiation, we detected an additional slower mobility of damaged chromatin sites showing a mean square displacement of  $\approx 0.6 \mu\text{m}^2/\text{h}$  after exposure to densely- or sparsely-ionizing radiation, most likely driven by normal diffusion of chromatin. Only occasionally, larger translational motion connected to morphological changes of the whole nucleus could be observed. In addition, there was no general tendency to form repair clusters in the irradiated cells. We conclude that long-range displacements of damaged chromatin domains do not generally occur during DNA double-strand break repair after introduction of multiple damaged sites by charged particles. The occasional and in part transient appearance of cluster formation of radiation-induced foci may represent a higher mobility of chromatin along the ion trajectory. These observations support the hypothesis that spatial proximity of DNA breaks is required for the formation of radiation-induced chromosomal exchanges.



## Chapter Four

### Spatial distribution of damage signals induced by low energy carbon and uranium ions

#### 4.1 Introduction

Double-strand breaks (DSBs) are one of the most deleterious types of DNA damage. Clustered lesions in the form of multiple damage sites, where a DSB is accompanied by other forms of damage, are especially detrimental (Ward 1994; Goodhead 1994; Rydberg 1996; Rydberg 2001). These multiply damaged DNA sites are expected to occur especially after exposure to densely ionizing radiation due to the close spacing of ionizing events. Irradiation with heavy ions provides this type of densely ionizing radiation, where the local dose deposition can be calculated according to the specific energy and linear energy transfer (LET) of the selected particle (Kraft *et al.* 1992; Krämer & Kraft 1994; Holey & Chatterjee 1996). In addition, ion radiation generates a localized and strictly linear channel of ionization that leads to localized production of DNA damage along the particle trajectory (Jakob *et al.* 2003). The radial extension of the track is defined by the short range of  $\delta$  electrons at low specific energies and a limited range of diffusion of highly reactive radical species. As a consequence of this localized damage, DNA damage-associated proteins accumulate and their dynamics can be monitored during the process of DNA repair. In eukaryotes, the DNA is packed within nucleosomes and is further folded into a 30-nm chromatin fiber and higherorder structures, resulting in chromosomes organized in chromosomal territories (Cremer *et al.* 2000). Soon after the generation of DSBs, the histone H2AX, a variant of H2A, is phosphorylated at its C-terminal serine (Ser139) comprising megabase-pair regions of the chromatin around the DSB (Rogakou *et al.* 1998; Rogakou *et al.* 1999). Phosphorylated H2AX ( $\gamma$ H2AX) can be detected within minutes after the induction of DSBs, and it serves as a platform for the recruitment and retention of other repair-related proteins such as 53BP1, NBS1 and MDC1 to the sites of DSBs (Celeste *et al.* 2002; Celeste *et al.* 2003; Ward *et al.* 2003; Stewart *et al.* 2003). Alternatively, the phosphorylation of H2AX modifies the surrounding chromatin and thus indirectly facilitates the accumulation of repair proteins (Fernandez-Capetillo *et al.* 2003). These ionizing radiation-induced foci involving larger DNA regions has been classified as “DSB flanking chromatin”-type (macrofoci), whereas proteins considered to be bound directly to the vicinity of the DNA lesion or subsequent processing stages (like single-stranded DNA) form smaller “microcompartments” (microfoci) (Bekker-Jensen *et al.* 2006). Overall, the distribution and dynamics of chromatin define the spatiotemporal organization of DNA repair events, which can be followed by these focal markers. Recently, a limited “movement” associated with local chromatin decondensation and protrusion of DSBs into the low-density chromatin was described after low-LET  $\alpha$  or local UV-laser irradiation (Kruhlak *et al.* 2006; Falk *et al.* 2007). Furthermore, Aten *et al.* (2004) discussed the formation of repair clusters containing several DSBs after linear track  $\alpha$ -particle irradiation requiring substantial motion of damaged chromatin sites. This motion might facilitate a long-range

homology search, but at the same time it could contribute to the formation of tumorigenic chromosome translocations. In contrast, experiments using focused ultrasoft X rays (Nelms *et al.* 1998) or single DSBs (Soutoglou *et al.* 2007) revealed apparently immobile DSBs. As a possible explanation, DSBs were suggested to be embedded in a dense cloud of adhesive  $\gamma$ H2AX domains that prohibited movement (Aten *et al.* 2004). The status of the different views of repair-associated chromatin motion was reviewed recently (Soutoglou & Misteli 2007). In a recent study, Costes *et al.* (2007) described a nonrandom distribution of repair-related proteins in human epithelial cells in the patterns obtained after exposure to 1 GeV/nucleon high-energy iron particle radiation or  $\gamma$  rays, leading to the conclusion that the induced foci are found preferentially at the interface of different chromatin densities in the nucleus. The aim of this study was to determine the spatiotemporal organization of DNA damage processing to clarify the extent of chromatin motion after exposure to high-LET ionizing radiation. The emphasis of our experiments was the comparison of the influence of lesion density (based on different LETs) on  $\gamma$ H2AX formation and the mobility of damaged chromatin sites. For this purpose, we produced linear radiation tracks (Jakob *et al.* 2003) with ions of different charge and mass but similar low specific energy to keep the radial extension of the track small and fairly constant. Our results show that in human fibroblasts as well as in HeLa cells the distribution of discrete foci of  $\gamma$ H2AX and other repair-related proteins along the ion trajectories was largely independent of the LET for low-energy particles. The deduction of motional activity of damaged domains in fixed human fibroblasts points to a relatively stable positioning of these domains during repair that is independent of LET. In HeLa cells, damaged chromatin domains displayed a higher degree of variation in the  $\gamma$ H2AX patterns observed at later times post-irradiation, indicating greater mobility during the processing of DSBs. Taken together, our data support the hypothesis that a large motional activity of damaged chromatin sites is not a general prerequisite for DNA repair.



## 4.2 Material and Methods

### 4.2.1 Cell Culture

Confluent normal human foreskin fibroblasts (AG1522D, Coriell Cell Repository, Camden, NJ; passage 13 to 16) and HeLa cells (kindly provided by M. Lavin, Queensland Institute of Medicine, Brisbane, Australia) were used for the experiments. Cells were grown on glass cover slips (24 x 24 mm) submerged in 35-mm petri dishes at 37°C, 100% humidity and 95% air/5% CO<sub>2</sub> in EMEM (Biochrome, Berlin, Germany) supplemented with 15% fetal calf serum (FCS) or RPMI 1640 medium (Biochrome) supplemented with 10% FCS. The fibroblast medium also contained 1% glutamine and 0.5% penicillin/streptomycin. Cells were checked regularly for mycoplasma contamination.

### 4.2.2 Irradiation

The irradiation was done at the UNILAC facility at the GSI Helmholtzzentrum für Schwerionenforschung (GSI, Darmstadt, Germany) with low-energy carbon ions (9.5 MeV/nucleon; LET 200 keV/μm at target) or uranium ions (3.0 MeV/nucleon; LET 14,300 keV/μm). For the immunofluorescence studies, square glass cover slips with cells at a density of about 80,000 cm<sup>-2</sup> were inserted upside down into plastic (PMMA) holders and placed in the corresponding medium in a multi-sample rack. For irradiation, holders were automatically grabbed and cells were exposed to the beam under a small angle. After exposure to the beam, which lasted about 30 s, cells were immediately placed back into the medium. Mock-irradiated cells or cells shielded in the lower half of the sample were used as controls. According to the calculations of Jakob *et al.* (2002), the mean nuclear cross section was about 90 μm<sup>2</sup> under the experimental conditions described (angle 15°). Thus the applied fluence of 2.2 x 10<sup>6</sup> cm<sup>-2</sup> results in a Poissonian distribution with an average of two traversals per nucleus for both fibroblasts and HeLa cells. The ions and corresponding parameters used are given in Table I. Doses are calculated for constant LET and may vary in individual nuclei according to the actual number of hits.

### 4.2.3 Immunofluorescence Assay

For the immunocytochemical staining experiments, cells were fixed in 2% formaldehyde and permeabilized as described previously (Jakob *et al.* 2002). Mouse monoclonal anti-phospho-(Ser139)H2AX primary antibody (clone JBW301; Upstate Biotechnology, Hamburg, Germany) was used at a dilution of 1:500 in 0.2% BSA in PBS together with rabbit polyclonal anti-XRCC1 (1:400; Serotec, Morphosys Düsseldorf, Germany) or mouse monoclonal anti-RPA (p34) (1:40; Lab Vision, Wedel, Germany) in combination with rabbit polyclonal anti-53BP1 (Ab1; 1:500; Oncogene, VWR Darmstadt, Germany), as indicated. For the colocalization experiment shown in Fig. 1C, mouse monoclonal anti-phospho-(Ser139)H2AX was used in combination with rabbit polyclonal Anti-53BP1 under the same conditions. Primary antibodies were detected with 5 μg ml<sup>-1</sup> Alexa 488 goat anti-mouse IgG conjugate (green) (Invitrogen, Karlsruhe, Germany) and counterstained with 1 μM ToPro3 (blue). In triple-stained samples, 5 μg ml<sup>-1</sup> Alexa 488 goat anti-mouse F(ab)<sub>2</sub> conjugate

(green) together with 5  $\mu\text{g ml}^{-1}$  Alexa 568 goat anti-rabbit IgG conjugate (red) and counterstaining with 1  $\mu\text{M}$  ToPro3 (blue) (all Invitrogen, Karlsruhe, Germany) were used.

#### 4.2.4 Microscopy

Microscopic imaging was done on a Leica TCS confocal system equipped with a DM IRBE inverted microscope (lens: HCX PlanApo 63x/1.32) and an argon-krypton laser. Visual inspection of several hundred cell nuclei per sample was done at 630x magnification. From each sample, images containing in total 30 to 100 nuclei were taken as sets of 12 to 20 optical sections. The optical sections were recorded in increments of about 0.2  $\mu\text{m}$  to 0.4  $\mu\text{m}$  across the thickness of cells, which was usually about 2–3  $\mu\text{m}$ .

#### 4.2.5 Quantitative Image Analysis

Analysis of track morphology was done in mean projections of acquired confocal stacks for more than 30 traversed nuclei for each point using IDL (V6.0; Research Systems Inc.)-based software developed in house in collaboration with the department of image processing of the University of Applied Science Darmstadt (Germany) (R. Schäfer, D. Schubert, K. Sandau). Briefly, tracks were recognized semi-automatically using radon transformation after segmentation of nuclei and extraction of signals above background. Track elements were detected using adaptive bimodal thresholds and fitted by 2D intensity projections of spheres with increasing radii. Overlapping radii were merged if the distance between the centers was less than 60% of the sum of the radii and were counted as a multi-centered *Cluster*. Four parameters were selected: *STD*, radial spreading perpendicular to the track based on the standard deviation of the fluorescence distribution; *Distance*, spacing between the observed (merged) focal structures; *Area* of the (merged) foci; and *Cluster*, representing the mean number of local intensity maxima being binned to a larger object by overlapping of more than 60% of their radii. For a schematic flow diagram of image processing, see Figure 4-4.

**TABLE I**  
**Irradiation Parameters**

Ion species	LET (keV/ $\mu\text{m}$ )	Fluence ( $\text{P cm}^{-2}$ )	Calculated mean number of traversals per average nucleus	Dose (Gy) calculated for constant LET
Carbon, 9.5 MeV/nucleon	200	$2.2 \times 10^6$	2.0	0.70
Uranium, 3.0 MeV/nucleon	14300	$2.2 \times 10^6$	2.0	50

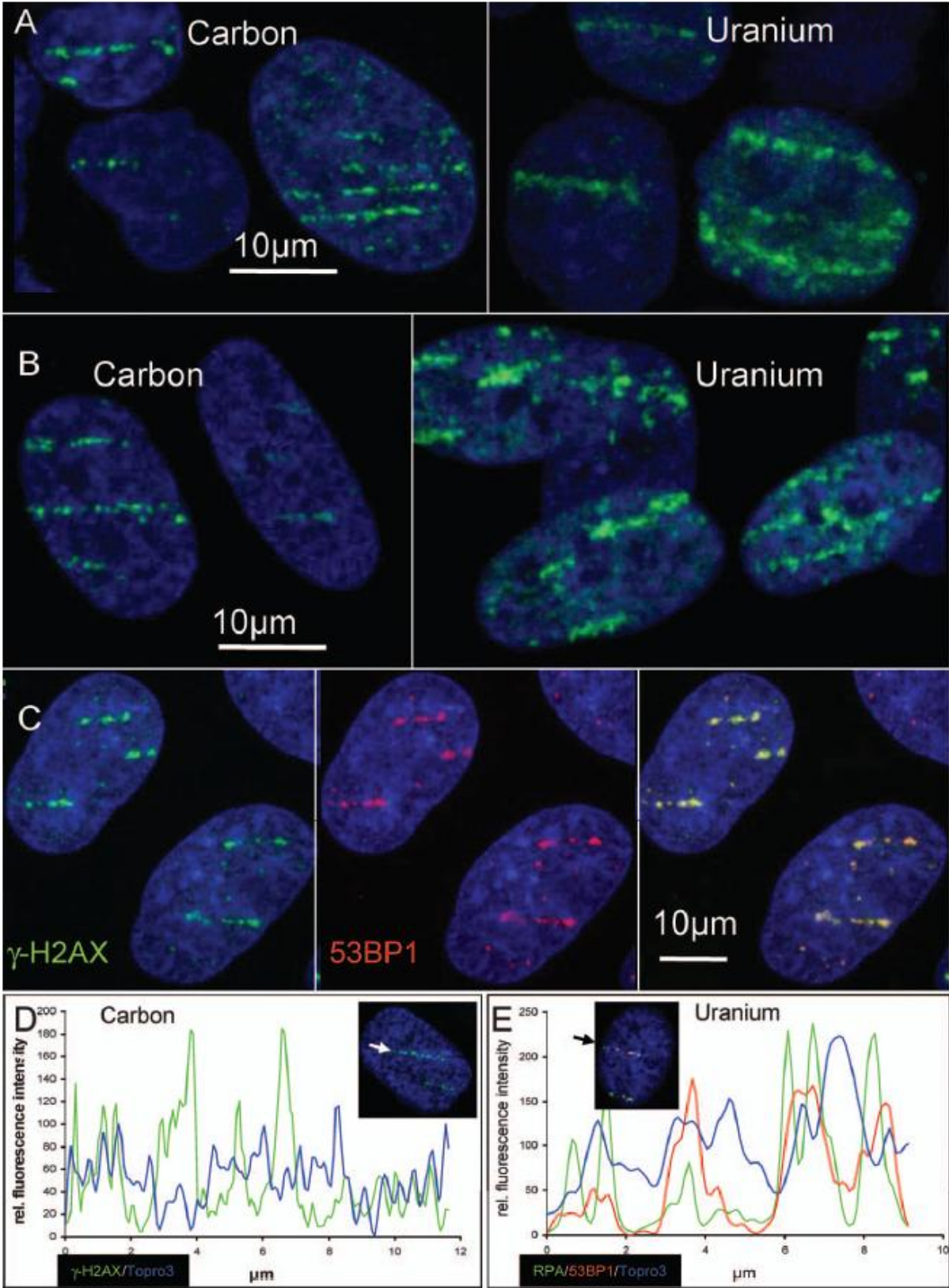
## 4.3 Results

This study was aimed at determining the mobility of damaged DNA sites in mammalian cell nuclei as indicated by the motion of radiation-induced foci. In the context of higher-order chromatin structure, the motion of the damaged DNA strands will inevitably be coupled to the dynamic properties of the surrounding chromatin domains. To facilitate the analysis of spatiotemporal organization of lesion processing, we took advantage of the localized nuclear response obtained after heavy-ion irradiation.

### 4.3.1 Localized Linear Streaks of $\gamma$ H2AX Induced by Heavy-Ion Tracks Show Slight Variations with LET but are Independent of Cell Type

We irradiated normal human AG1522 fibroblasts or HeLa cells with low-energy charged particles under a small angle to produce linear tracks of damage. After irradiation of cell nuclei with carbon or uranium ions at a fluence of  $2.2 \times 10^6$  particles/cm<sup>2</sup>, leading to a mean of around two traversals per nucleus, we stained for the DSB marker  $\gamma$ H2AX (Fig. 4-1). In all cases, each traversing ion led to a streak of phosphorylated H2AX along the single ion trajectory 10 min post-irradiation (Fig. 4-1A and B). The patterns of distribution of  $\gamma$ H2AX were similar in fibroblasts and HeLa cells (compare Figs. 4-1A and B). 53BP1 always showed the same distribution as  $\gamma$ H2AX along the ion trajectories, as indicated by the complete colocalization of the two signals in HeLa cell nuclei 1 h after irradiation with carbon ions (Fig. 4-1C). The observed gapped structure of  $\gamma$ H2AX is correlated to the underlying chromatin distribution. In Figs. 4-1D and E, single deconvoluted optical confocal slices (Huygens essential; SVI, The Netherlands) of fibroblast nuclei (DNA: blue) are shown overlaid by the corresponding  $\gamma$ H2AX signal (green) 10 min after irradiation with carbon ions (Fig. 4-1D) or RPA (green) and 53BP1 (red) 1 h after irradiation with uranium ions. The tracks marked by the arrows are displayed as intensity profiles for the different channels. In both cases, the protein signals can be detected either at chromatin peaks or, more often, adjacent to the DNA maxima. This behavior is most obvious for the sharp RPA staining after uranium-ion irradiation. The detection of DSB-dependent protein signals at the border of highly and less stained chromatin is consistent with previous observations in epithelial cells after high-energy ion irradiations (Costes *et al.* 2007).

When comparing  $\gamma$ H2AX formation induced by carbon (LET: 200 keV/ $\mu$ m) and uranium ions (LET: 14300 keV/ $\mu$ m), some differences in the distribution became apparent despite major similarities. Visual inspection of  $\gamma$ H2AX patterns for at least 100 tracks for each cell line and time revealed a slight LET dependence of the packing of  $\gamma$ H2AX-labeled domains along the ion trajectories at short times post-irradiation (e.g., see Figs. 4-1 and 4-2 for carbon ions and Figs. 4-1 and 4-3 for uranium ions). Based on a homogeneous nuclear DNA distribution and calculating with the assumption of 35 DSBs induced per Gy of ionizing radiation (Prise *et al.* 1998), the expected values for DSB production along the trajectories were 2.6 DSBs/ $\mu$ m for carbon ions and 187 DSB/ $\mu$ m for the low-energy uranium-ion tracks. In the case of carbon-ion tracks (Fig. 2), roughly 0.5 to 1 focus per  $\mu$ m track length could be detected 10 min after irradiation, with a mean of 0.63 focus/ $\mu$ m evaluated in more than 100 tracks. These values are similar to those reported previously for hMRE11 after bismuth-ion irradiation (Jakob *et al.* 2003). In the case of uranium ions, the  $\gamma$ H2AX foci appear denser and



fuzzier during the first hour, making the counting of distinct foci quite difficult (Fig. 4-3 upper row, green). To overcome the problems of potential overlapping of stained megabasepair domains in the case of very high-LET particles and to stain and distinguish the locations of the lesions inside individual domains more precisely, we used different protein markers. Staining of XRCC1 led to well-defined small spots embedded within the  $\gamma$ H2AX-

**Figure 4-1.** Low-energy particle irradiation leads to linear tracks of  $\gamma$ H2AX in cell nuclei. Panel A: HeLa cell nuclei 10 min after low-angle irradiation with carbon ions (LET: 200 keV/ $\mu$ m, left) or uranium ions (LET: 14,300 keV/ $\mu$ m, right) and immunostained for  $\gamma$ H2AX (green). DNA counterstain: TOPRO3 (blue). Panel B: Normal human AG1522 fibroblasts were irradiated with low-energy carbon ions (LET: 200 keV/ $\mu$ m, left) or uranium ions (LET: 14300 keV/ $\mu$ m, right) and immunostained for  $\gamma$ H2AX (green) (blue: TOPRO3).  $\gamma$ H2AX staining represents the distribution of DSB-containing chromosomal domains along the ion trajectories. Panel C: Colocalization of  $\gamma$ H2AX (green) and 53BP1 (red) in HeLa cell nuclei 1 h after low-angle irradiation with carbon ions (LET: 200 keV/ $\mu$ m). Both markers stain the damaged chromatin domains identically as indicated by the yellow color of the overlay (right). DNA counterstain: TOPRO3 (blue). Panels D and E: Intensity line scans of the fluorescence of a single optical confocal slice [deconvoluted by Huygens essential (SVI, The Netherlands)]. The intensities along the respective trajectories marked by the arrows are displayed in the profiles. The images of the single slices are shown as insets. Correlation of  $\gamma$ H2AX (green) and chromatin stained by TOPRO3 (blue) in AG1522 fibroblast nuclei 10 min after low-angle irradiation with carbon ions (LET: 200 keV/ $\mu$ m; panel D). Correlation of RPA (green), 53BP1 (red) and chromatin stained by TOPRO3 (blue) in AG1522 fibroblast nuclei 1 h after low-angle irradiation with uranium ions (LET: 14,300 keV/ $\mu$ m; panel E).

stained domains after ion irradiation (Fig. 4-3, upper row, inset, red). The appearance of the small XRCC1 spots is comparable to that of proteins described to form radiation-induced microcompartments after laser irradiation. This type of marker had been proposed to directly stain the site and closer surroundings of the lesion and not the DSB flanking chromatin (Bekker-Jensen *et al.* 2006). Surprisingly, counting of individual XRCC1 foci along the trajectories also yielded values of around 1 microfocus per  $\mu$ m of track length (mean value for 65 tracks: 0.96 focus/ $\mu$ m) 10 min after irradiation with uranium ions, which was only slightly higher than the numbers obtained for carbon ion irradiation despite the large difference in LET. The small XRCC1 foci were always exactly correlated with  $\gamma$ H2AX staining. Surprisingly, very large gaps well above the resolution limit of the optical setup were observed between these microfoci even inside the  $\gamma$ H2AX areas, where the presence of chromatin can be assumed. Thus XRCC1 also shows only a limited number of discrete foci and does not represent the expected values for DSBs (187/ $\mu$ m) or even higher numbers for SSBs that should lead to a more continuous DNA-based signal due to the limited resolution of a light microscope. Similar results were obtained after 1 h post-irradiation incubation and staining for RPA as a more DSB-specific microfocus marker as outlined below.

To summarize, the initial distributions of DNA DSBs generated by charged particles of different LET but the same low specific energy and detected by H2AX phosphorylation were strikingly similar in the cell lines studied here, in addition to the higher intensity of  $\gamma$ H2AX staining during the first hour of observation after exposure to very high-LET radiation. Clearly, variations in LET (lesion density) are not directly related to the number of radiation-induced foci observed. This was confirmed using different proteins known to bind to DSBs and is in agreement with our previous results for repair-related proteins (Jakob *et al.* 2003; Jakob & Taucher-Scholz 2005; Taucher-Scholz & Jakob 2006).

#### 4.3.2 $\gamma$ H2AX-Stained Domains along Heavy-Ion Trajectories Show Focus Loss with Time at Lower LET

Because the lesion density was not represented accurately by the initially observed protein patterns, we evaluated the influence of the ionization density on linear track morphology

during the processing of DSBs. For this purpose, we analyzed the  $\gamma$ H2AX staining patterns along the carbon- and uranium-ion trajectories as a function of incubation time. In the case of carbon-ion irradiation of human fibroblasts, the individual tracks could be identified easily up to at least 5 h, even if the whole cell rotated (Fig. 2, 3h, middle). At later times, identification of the original trajectory became increasingly difficult, mainly because of loss of foci. Thus, at 18 h post-irradiation, the remaining radiation-induced foci could be assigned to defined

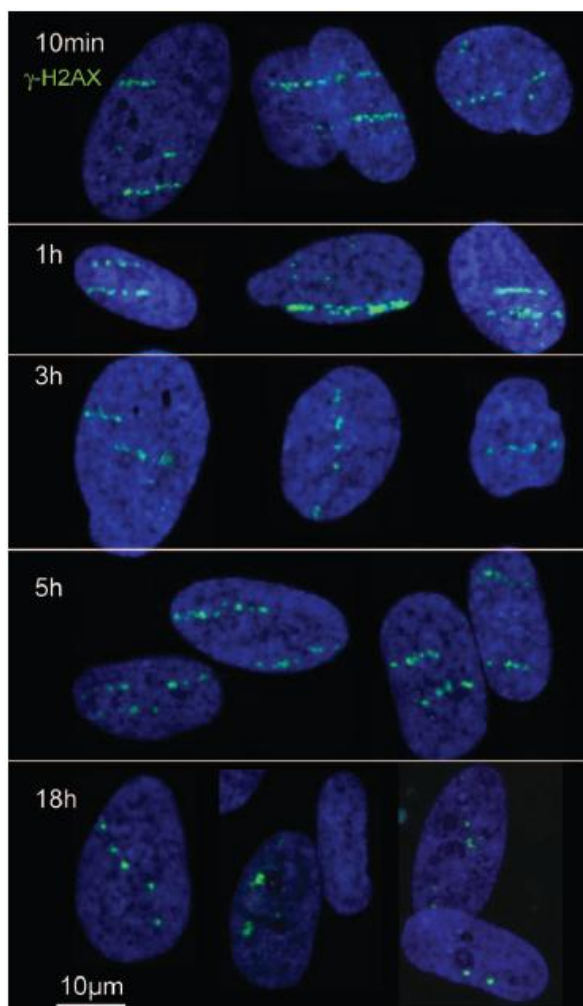


**Figure 4-2.** Limited mobility of DSBs within carbon-ion tracks in human fibroblasts. Normal human AG1522 fibroblasts were irradiated with low-energy carbon ions (LET: 200 keV/μm) using small-angle irradiation. Cells were fixed at different post-irradiation incubation times as indicated and immunostained for  $\gamma$ H2AX (green).  $\gamma$ H2AX staining represents the distribution of DSB-containing chromosomal domains along the ion trajectories. DNA counterstain: TOPRO3 (blue).

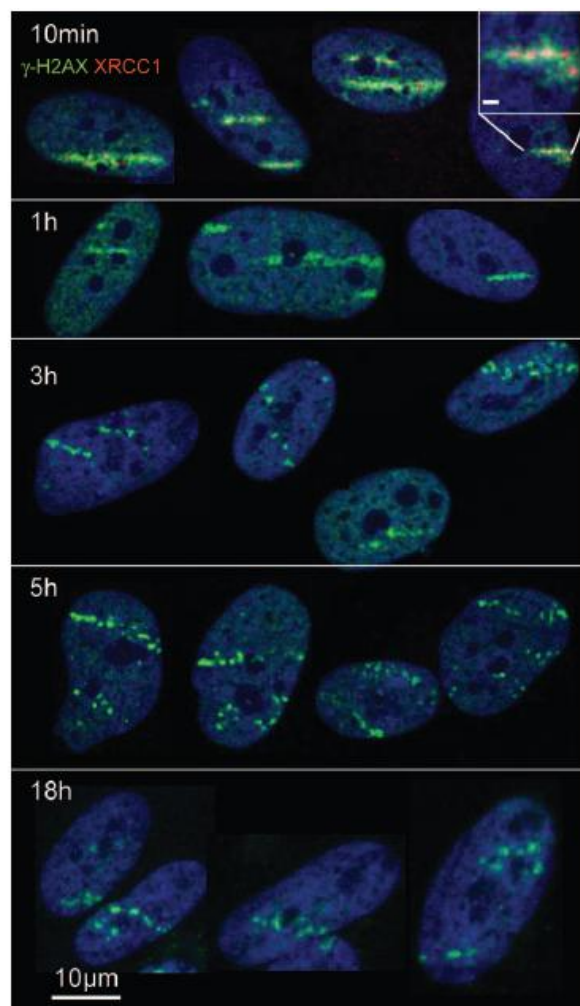


**Figure 4-3.** “DSBs” in human fibroblasts produced along uranium-ion tracks are largely immobile and are not repaired. Human AG1522 fibroblasts were irradiated with low-energy uranium ions (LET: 14,300 keV/μm) using small-angle irradiation as in Figs. 1 and 4-2. Cells were fixed at different post-irradiation incubation times as indicated and immunostained for  $\gamma$ H2AX (green).  $\gamma$ H2AX staining reflects the distribution of DSB-containing chromosomal domains along the ion trajectories. At 10 min post-irradiation, XRCC1 was immunostained additionally in red, showing only a few microfoci in the  $\gamma$ H2AX-stained domains despite the expected high lesion density. DNA counterstain: TOPRO3 (blue). Inset: Magnification of the XRCC1 (red) within the region of  $\gamma$ H2AX (green). Bar: 1 μM.

trajectories in only 25–30% of the nuclei, giving a bias to nuclei and possible foci showing less efficient repair. Even here, at 18–24 h post-irradiation, only about 0.3 focus/ $\mu\text{m}$  persisted (>100 trajectories evaluated), indicating the loss of more than 50% of the initially observed  $\gamma\text{H2AX}$  foci in the detected trajectories. Taken together, the loss of foci and the fraction of nuclei with defined trajectories indicate ongoing but impaired repair of carbon-ion-induced DSBs, with more than 80% of the total number of initial  $\gamma\text{H2AX}$  foci being resolved 24 h after irradiation.

In the case of lesions generated by uranium-ion trajectories, with increasing time post-irradiation, the originally fuzzy  $\gamma\text{H2AX}$  signal gained contrast and structure, leading to more distinct  $\gamma\text{H2AX}$  foci evident at 3 h post-irradiation incubation and later. Loss of foci within the tracks was less pronounced for uranium-ion irradiation (Fig. 4-3), leading to clear detection of streaks in nearly all hit fibroblast nuclei. When we compared the uranium-ion-induced tracks to those induced by carbon ions (Figs. 1-2 and 4-3), LET-dependent differences became apparent with increasing incubation time, with closer spacing of foci after higher-density initial DNA damage (higher LET) most evident at the latest time of 18 h. The mean number of  $\gamma\text{H2AX}$  foci was 0.59 focus/ $\mu\text{m}$  (>100 tracks) at 18 to 24 h post-irradiation. For long-term follow-up of damaged chromatin sites, high-LET radiation has the advantage of longer observation periods. Similar observations were made for HeLa cells after irradiation with low-energy uranium ions as outlined below. The  $\gamma\text{H2AX}$ -stained domains along low-energy ion trajectories show only slight variations with LET over the range of 200 to 14300 keV/ $\mu\text{m}$  at short times post-irradiation despite the expected scaling of DSBs. Differences in focus distribution along tracks became evident with longer incubation time, showing a substantial loss of  $\gamma\text{H2AX}$  foci after carbon-ion irradiation.

### 4.3.3 Quantitative Image Analysis Reveals Only Moderate Spreading and Clustering of Radiation-Induced Foci

To overcome the limitations and subjective classification resulting from the visual inspection of  $\gamma\text{H2AX}$  formation along the ion trajectories, a newly developed semi-automatic software algorithm was applied for the evaluation process (see the Material and methods and Fig. 4-4). In addition to the recognition and fitting of the trajectory angle using radon transformation, the software provides quantitative information about the structural features of the aggregate distribution along the ion tracks. Quantitative results are summarized in Fig. 5. The  $\gamma\text{H2AX}$  signal produced by carbon-ion trajectories (Fig. 5A–D, sample images in Fig. 4-2) showed about a twofold increase in the interfocal distance (*Distance*) parameter [from around 1.5  $\mu\text{m}$  (10 min) to >2.5  $\mu\text{m}$  at 18 h; Fig. 4-5A], reflecting the loss of foci and repair with time also described above. The interfocal distance of 1.5  $\mu\text{m}$  corresponds well with the manually counted 0.5 to 1 focus/ $\mu\text{m}$ . In addition, a moderate increase in the radial spreading (*STD* parameter) was found within the 18-h observation time (Fig. 4-5B), going from slightly below 1  $\mu\text{m}$  to 1.3  $\mu\text{m}$ . The modest increase in the *STD* parameter indicates the very slow diffusion of the damaged chromatin. There was a transient approximately twofold increase of the area of the  $\gamma\text{H2AX}$  foci from approximately 0.6  $\mu\text{m}^2$  at 10 min after irradiation to a maximum of 1.2  $\mu\text{m}^2$  at 3 h after irradiation. Obviously, the phosphorylation of H2AX around the breaks is not finished at the earliest time (10 min), leading to successively larger areas of radiation-

**Raw data: confocal image stacks: Leica TCS NT**

Software was developed in IDL in collaboration with the department of image processing of the Univ. of Applied Science Darmstadt (Germany) (R.Schäfer, D. Schubert, K.Sandau)

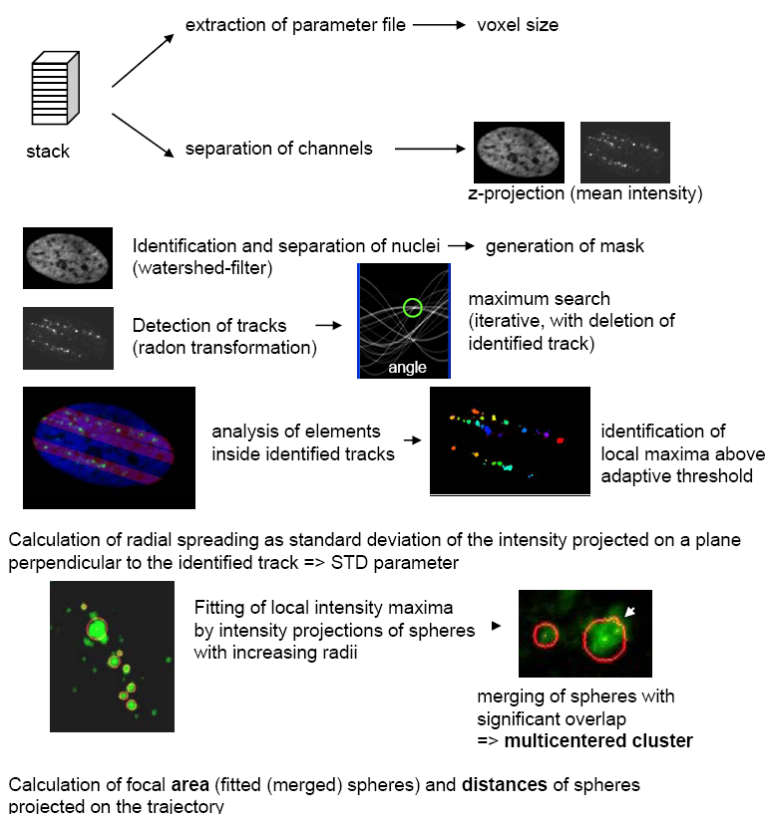


**Figure 4-4.** Schematic flow diagram showing the different steps of the quantitative image analysis. Analysis of track morphology was done in mean projections of acquired confocal stacks (Leica TCS NT) by IDL (V6.0; Research Systems Inc.)-based software developed in collaboration with the department of image processing of the University of Applied Science Darmstadt (Germany). After separation of channels and parameters, tracks were recognized semi-automatically using radon transformation after segmentation of nuclei and extraction of signals above background. Track elements were detected using local maxima search using an adaptive bimodal threshold, and 2D intensity projections of spheres with increasing radii were fitted to the identified objects. Overlapping objects were merged if the distance between the centers was less than 60% of the sum of their radii and counted as a multicentered *Cluster*. Four parameters were selected: *STD*, radial spreading perpendicular to the track based on the standard deviation of the fluorescence distribution; *Distance*, spacing in between the observed (merged) focal structures; *Area* of the (merged) foci; and *Cluster*, representing the mean number of local intensity maxima being binned to a larger object by overlapping of more than 60% of their radii.

induced foci. Later, starting after 3 h, the focal area of  $\gamma$ H2AX inside the carbon-ion-induced trajectories decreased to around  $0.85 \mu\text{m}^2$  (Fig. 4-5C). A small part of the initial increase and the later decrease in size might be explained by a transient tendency to form larger multicentered clusters, which can be seen in the *Cluster* parameter (for definition, see the Material and Methods section). However, this tendency was not very pronounced, comprising 8% of all detected focal structures at 10 min post-irradiation and a maximum of 15% at 1 to 3 h post-irradiation. Afterward the cluster parameter dropped back to around 8% (18 h) (Fig. 4-5D).

Similar trends were obtained for  $\gamma$ H2AX foci along the densely ionizing uranium-ion tracks (Fig. 4-5E–H, sample images in Fig. 4-3). However, compared to carbon-ion radiation, an increased initial signal density is revealed by the reduced distance parameter of approximately

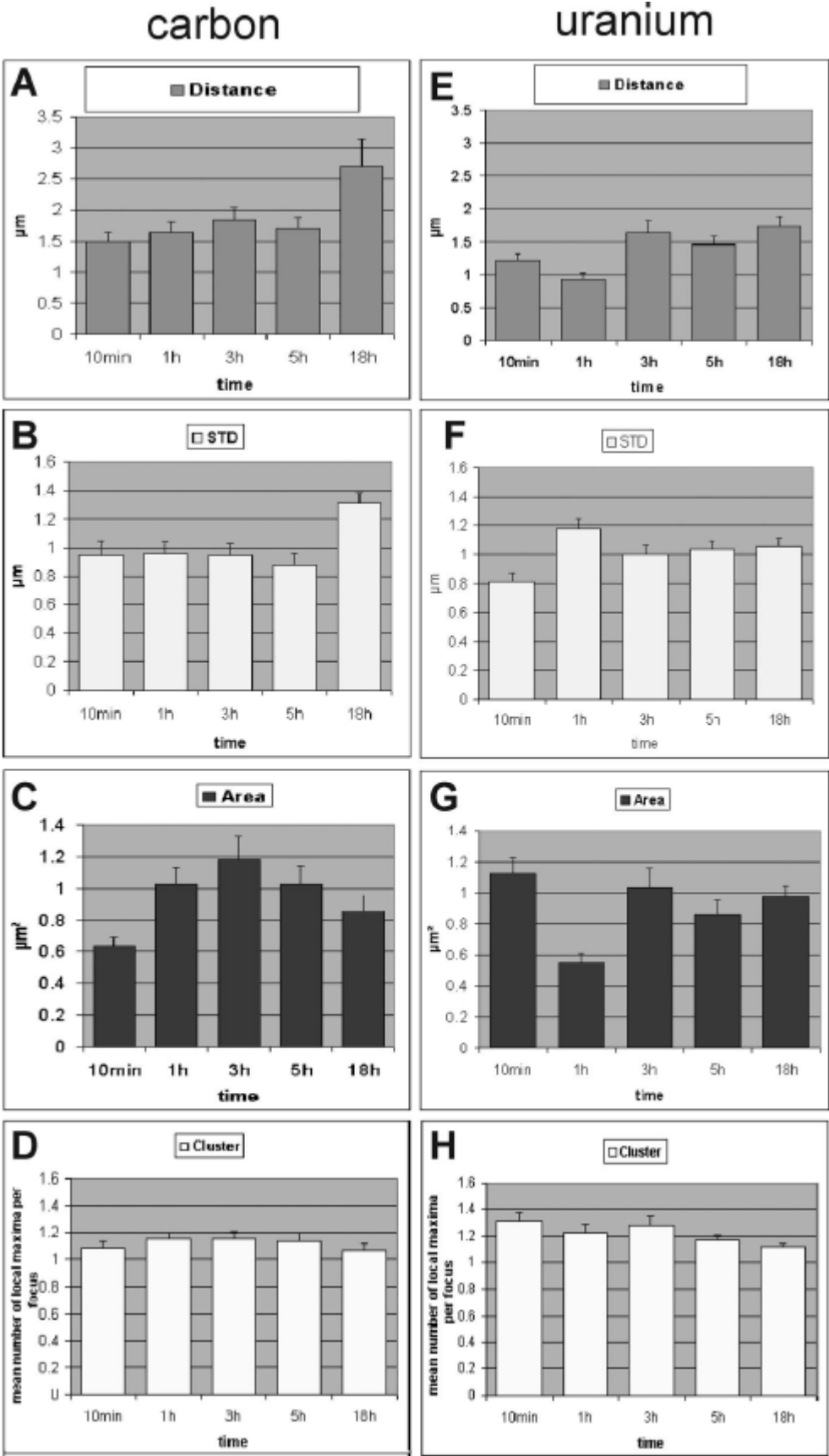


1  $\mu\text{m}$  during the first hour (Fig. 4-5E) and the increased cluster parameter (Fig. 4-5H). The interfocal distance (*Distance*) increased only slightly to 1.7  $\mu\text{m}$  18 h post-irradiation (Fig. 4-5E), reflecting reduced loss of foci. The radial spreading (*STD*) of the signal was found to increase from 0.8 to 1.2  $\mu\text{m}$  in the first hour and to remain stable around 1  $\mu\text{m}$  over the 18-h time course (Fig. 4-5F). Thus the radial distribution was in the same range as that after carbon-ion irradiation (Fig. 4-5B). Figure 4-5H shows an increased fraction of multicentered clusters (around 20–40% of all focal structures during the first hours) in the case of high-LET uranium-ion irradiation directly at the first observation; later this value decreased to 12%. The focal area parameter decreased from around 1.1  $\mu\text{m}^2$  to slightly below 1  $\mu\text{m}^2$  when the outlier at 1 h post-irradiation is disregarded (Fig. 4-5G). This outlier comes from a single experiment, whereas the values for all other times are from two independent radiation experiments. It can also be explained at least in part by the poor definition of single elements in the fuzzy tracks observed at short times (see Fig. 4-3) in combination with the automatic background suppression in the computational analysis. In summary, the quantitative analysis of the  $\gamma\text{H2AX}$  patterns along the ion trajectories confirmed the observations of the visual inspection, showing a striking similarity of the initial focal spacing of carbon- and uranium-ion tracks despite the difference in LET of a factor of 70. The structural parameters indicate a positional stability of damaged DNA sites, revealing only a transient tendency to form clustered aggregates and a very moderate spreading of the localized signal with time for both ion species. It must be stated, however, that at later times the quantified changes were slightly underestimated, because isolated residual foci (occurring in about 35% of nuclei analyzed 18 h post-irradiation) could no longer be uniquely attributed to a defined trajectory and thus were excluded from the analysis. In addition, fitting the most probable trajectory by using the angle as a free parameter tends to minimize the radial spreading (*STD*).

#### 4.3.4 Similar Distribution but Varying Substructure of Ion-Induced Repair Protein Foci

To compare the structure of  $\gamma\text{H2AX}$  repair foci that respond within a DSB flanking megabase-pair domain (Rogakou *et al.* 1999) with other DSB markers, we stained AG1522 fibroblasts for 53BP1 and RPA after irradiation with low-energy carbon and uranium ions (Fig. 4-6). 53BP1 is a key component of the genome surveillance network activated by DNA DSBs through phosphorylation by ATM, and it binds to the DSB flanking chromatin regions, forming macrofoci (Bekker-Jensen *et al.* 2005; Bekker-Jensen *et al.* 2006).

Here we demonstrate the colocalization of 53BP1 with  $\gamma\text{H2AX}$  along the trajectories of low-energy ions (Fig. 1C), in agreement with the results obtained after irradiation with HZE (high-energy and high-Z) particles (Asaithamby *et al.* 2008). The 53BP1 signal (red) in Fig. 4-6 resembles the structural information of  $\gamma\text{H2AX}$  with regard to the gapped structure. In contrast to these macrofocus markers that are distributed around the damaged sites, RPA binds to single-stranded intermediates resulting from enzymatic DSB resection, which occur during homologous recombination (Bekker-Jensen *et al.* 2006) but may also be produced during the processing of multiply damaged DNA sites. RPA has been shown to bind directly to the single-stranded DNA, and it is considered not to mark the flanking chromatin regions but to form smaller microcompartments (Bekker-Jensen *et al.* 2006). The different behavior of the two classes of DSB marking proteins can be seen clearly in the results of the co-



staining experiment in Fig. 4-6 (see also line scans in Fig. 4-1E), confirming different binding modalities. Figure 4-6 shows the time-dependent changes in radiation-induced protein aggregation patterns for the co-staining of RPA (green) and 53BP1 (red) after irradiation with carbon and uranium ions, respectively. Being spatially connected to the region of traversing

**Figure 4-5.** Quantitative analysis of the distribution pattern of  $\gamma$ H2AX along the ion trajectories. Tracks produced by carbon ions (panels A–D) or uranium ions (panels E–H) in AG1522 fibroblasts as shown in Fig. 4-2 or 4-3, respectively. Trajectories were defined automatically by a best linear fit and were subjected to quantitative analysis of the signal pattern. Four parameters were extracted: *Distance* (panels A and E), denoting the spacing in between the observed focal structures; *STD* (panels B and F), representing the radial spread perpendicular to the track; *Area* (panels C and G) of the (merged) foci; and *Cluster* (panels D and H), representing the mean number of local intensity maxima being binned to a larger object when overlapping more than 60% of their radii. Panels A–D: Irradiation with low-energy carbon ions (sample images in Fig. 1). The increase in the *Distance* between foci at 18 h post-irradiation indicates a loss of foci due to repair (panel A). In addition, a radial broadening of the track (represented by the increase of the *STD* parameter at 18 h (panel B) and a transient increase in focal area (panel C) could be observed. This increase in the focal area was due in part to the slight tendency of formation of overlapping foci (*Cluster*) (panel D). Panels E and F: irradiation with low-energy uranium ions (sample images in Fig. 4-2). Data are mean values taken from two independent experiments except at 1 h. Irradiation with uranium ions leads to a fuzzy signal at 10 min and 1 h post-irradiation, which is measured as a greater tendency of formation of overlapping foci (panel H) and reduced interfocal distance (panel E). The moderate increase in the *Distance* parameter reflects the impaired repair. Despite an increase in the radial spreading during the first hour (panel F), there was no change of the further radial distribution. The size of individual foci decreased slightly with time (panel G). The outlier of the area parameter at 1 h post-irradiation is most probably due to the poor definition of individual elements and a high background staining at this time.

←

ions, RPA (green) forms small aggregates embedded in the larger 53BP1 signal (red) along the trajectories, similar to the observed XRCC1 microfoci within the  $\gamma$ H2AX domains (Fig. 4-3, 10 min). It should be noted that each RPA microfocus always colocalized with a 53BP1 signal, which in most cases occupied a larger area. In about 5 to 7% of the cases, two or three tiny RPA foci were observed inside a single 53BP1 focus (inset in Fig. 4-6B). Both 53BP1 and RPA show clear streaks along the path of the ion traversal up to 5 h post-irradiation independent of LET (Fig. 4-6), confirming the spatial stability of the damaged chromatin domains in human fibroblasts suggested by  $\gamma$ H2AX staining (Figs. 4-2 and 4-3). At 18 h post-irradiation incubation time, the patterns of both 53BP1 and RPA are characterized by focus loss in the case of carbon ions, even if these foci do not represent individual DSBs, whereas uranium-ion-induced DNA damage can still be seen in the form of streak patterns in most hit nuclei (Fig. 4-6). These observations provide evidence for an LET-dependent impairment of repair of DSBs. It must be emphasized that at short times, the similarities of the patterns and numbers of foci along the carbon- and uranium-ion tracks are also retained for the microfoci displaying RPA signal despite differences in the amounts of DSBs induced. In the case of high-lesion-density uranium-ion irradiation, the RPA foci clearly also do not represent the expected numbers of DNA DSBs.

In agreement with previous observations, our results obtained with different markers for DNA DSBs all point to a spatial stability of damaged chromatin domains. Two different types of markers, one tightly localized to the sites of DNA DSBs like RPA and the other also staining the adjacent chromatin, showed a distribution along the tracks that is nonlinearly correlated with damage density. Thus all DSB markers examined have in common that they do not represent the total number of expected DSBs after ion irradiation.

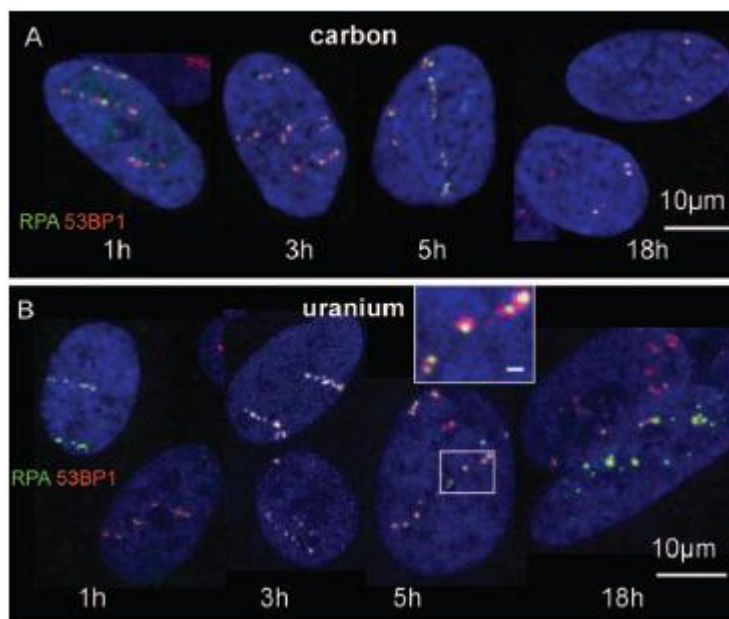


**Figure 4-6.** Distribution and colocalization of RPA and 53BP1 in human fibroblasts after carbon- or uranium-ion irradiation. Human AG1522 fibroblasts were irradiated with low-energy carbon (LET: 200 keV/ $\mu\text{m}$ ) (panel A) or uranium ions (LET: 14,300 keV/ $\mu\text{m}$ ) (panel B) (irradiation images as in Fig. 1 or 4-2, respectively). Cells were fixed at different post-irradiation incubation times and immunostained for RPA (green) and 53BP1 (red). RPA staining represents the distribution of single-stranded DNA, whereas 53BP1 marks the DSB-containing chromosomal domains along the ion trajectories. DNA counterstain: TOPRO3 (blue). Inset: Magnification of the RPA microfoci (green) inside the 53BP1 domains (red).

#### 4.3.5 High Inter- and Intranuclear Variability/Heterogeneity of Ion-Induced Repair Protein Patterns in HeLa Cells Reveals Lesion Mobility

To avoid the loss of analyzable tracks at later times, which restricted the deduction of a dynamic behavior of damaged chromatin sites, and in view of the previous results showing LET-independent dynamics in fibroblasts, we used high-LET uranium ions to study repair processing in HeLa cells (Fig. 4-7). As described above (Fig. 4-1), traversing uranium ions led to a linear track of generated lesions indicated by fast phosphorylation of H2AX (Fig. 4-7, 10 min). At 3 h post-irradiation, a significant bending of these linear structures was observed in a fraction of nuclei. Later, 25 to 30% of nuclei showed a disaggregation of some streaks (marked by arrows in Fig. 4-7, 5 h and 10 h), although occasionally more than one ion traversal in the near vicinity could also be the cause of the observed pattern. After 10 h post-irradiation incubation, the heterogeneity of possible radiation responses became most obvious (Fig. 4-7; 10 h). Whereas about one half of the nuclei showed nearly continuous and linear streaks of  $\gamma\text{H2AX}$  (Fig. 4-7; 10 h left), the others showed clearly separated foci (Fig. 4-7; 10 h right). Again, around 25 to 30% of streaks were characterized by disaggregation and poor definition (Fig. 4-7; 10 h right, arrow).

The comparison of changes in track morphology displayed by  $\gamma$ H2AX-marked domains is based on the assumption of a similar pattern being produced at a given LET and time. However, a considerable degree of heterogeneity in the observed patterns of a selected protein can be found from the beginning and at all times of observation. This heterogeneity becomes obvious in the different manifestations of the punctuate structures, showing regularly separated or rather aggregated types of foci. This variability can be observed in different nuclei and at different positions in the same nucleus. It is clearly apparent in the HeLa cells but was also observed to a somewhat lower degree in the fibroblast nuclei (Figs. 4-2 and 4-3). The variety of response patterns of protein aggregates found even in one nucleus makes a precise deduction of internal migration of lesions with time difficult using fixed nuclei at different incubation times. Nevertheless, the fact that clear track structures can be found even after incubation times of several hours in the great majority of nuclei points to a stable positioning of damaged chromatin sites in both HeLa cells and human fibroblasts.

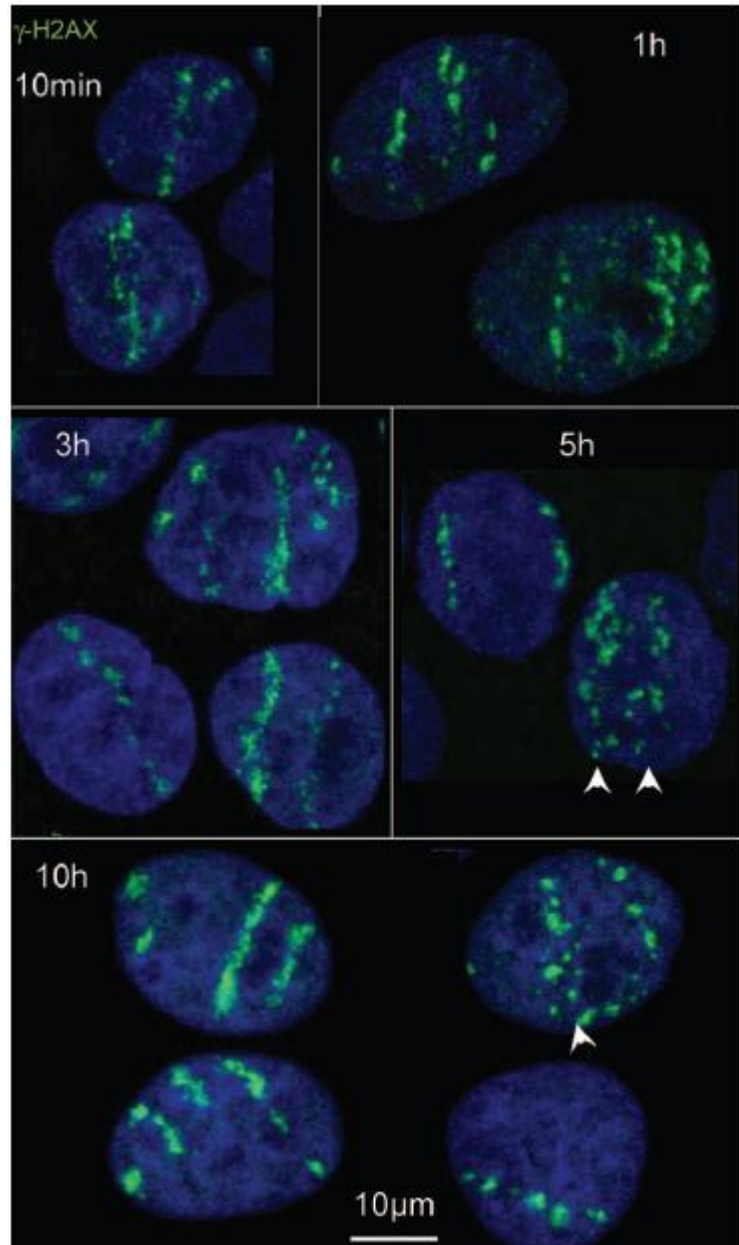


**Figure 4-7.** Time-dependent DSB distribution in HeLa cells after uranium ion irradiation. HeLa cells were irradiated with low-energy uranium ions (LET: 14,300 keV/ $\mu$ m) and fixed at different post-irradiation incubation times as indicated. Cells were immunostained for  $\gamma$ H2AX (green). Variability in the observed  $\gamma$ H2AX patterns is apparent with increasing incubation time, indicating enhanced chromatin mobility in a fraction of nuclei and tracks, most evident at 5 and 10 h post-irradiation. Tracks indicating enhanced mobility or disaggregation are marked by arrows. In most nuclei, a general positional stability can still be observed. DNA counterstain: TOPRO3 (blue).

## 4.4 Discussion

The mobility of chromatin in the context of repair was reviewed recently (Soutoglou & Misteli 2007). However, questions and controversy remain regarding the dynamics of damaged chromatin after high-LET irradiation, a topic covered in only a few studies up to now (Aten *et al.* 2004; Costes *et al.* 2007).

In this work we addressed the mobility of sites of DNA DSBs, focusing on potential differences in the migration behavior relative to the higher lesion density after the introduction of spatially correlated damage by densely ionizing radiation. One goal of this work was to determine whether, in contrast to  $\alpha$  particles, heavier particles with higher LETs would restrict the mobility of damaged chromatin, as proposed by Aten *et al.* (2004), possibly by a more extensive phosphorylation of the histone H2AX. As shown previously by our group and others, using low-energy ion irradiation under a small angle between the cell layer and the incoming particles leads to the accumulation of a series of repair-related proteins and the formation of phosphorylated H2AX (Jakob *et al.* 2003; Aten *et al.* 2004; Jakob & Taucher-Scholz 2005). In this study, different LETs were achieved using low-energy particles of different mass and charge states to restrict the deposited dose to a small nuclear volume along the trajectory of the particle, in contrast to experiments using HZE particles (Desai *et al.* 2005; Jakob & Taucher-Scholz 2005; Costes *et al.* 2007; Asaithamby *et al.* 2008). Taking into account the physico-chemical mechanism of damage generation in common with sparsely ionizing radiation, mainly by coulomb interaction and the production of fast electrons, charged-particle radiation leads to the expectation of types of lesions normally produced by ionizing radiation and accordingly, similar subsequent lesion processing. In this respect, heavy-ion irradiation might differ from UVlaser microirradiation, especially because this technique is generally used in combination with DNA sensitization (Rogakou *et al.* 1999; Tashiro *et al.* 2000; Celeste *et al.* 2003). One additional advantage of using ions instead of laser microirradiation is that, in the case of charged particles, the density of lesions can be scaled directly according to the specific energy and LET of the particle used. The strictly localized generation of DSBs indicated by  $\gamma$ H2AX formation and the colocalization with 53BP1 and RPA along the low-energy ion trajectories could be demonstrated during this study using particles with different LETs. An important finding was that the amount of  $\gamma$ H2AX domains observed (Figs. 4-1 to 4-3) and the measured interfocal *Distance* (Fig. 5) 10 min after irradiation did not agree with the expected values for DSBs generated along the trajectories for high-LET particles. Calculating 35 DSBs per gray of ionizing irradiation (Prise *et al.* 1998), the expected values were 2.6 DSBs/ $\mu\text{m}$  for carbon ions and 187 DSBs/ $\mu\text{m}$  for uranium ions, assuming a homogeneous distribution. Experimentally, less than 1 DSB/ $\mu\text{m}$  was found in each case for AG fibroblasts, which was slightly below the 2.2 DSBs/ $\mu\text{m}$  observed by Aten *et al.* (2004) after  $\alpha$ -particle irradiation (estimated LET around 100 keV/ $\mu\text{m}$ , which would correspond to the expectation of 1.3 DSBs/ $\mu\text{m}$ ) in HeLa cells. These differences could be explained by the different DNA content of the two cell lines examined. However, comparing the images in Fig. 4-1, no obvious difference in the  $\gamma$ H2AX patterns of the two cell lines can be seen. Using a lower estimation of 20 DSBs/Gy (Kegel *et al.* 2007) resulted in values closer to our data for carbon ions (1.5 DSBs/ $\mu\text{m}$ ), but calculated values for the uranium-ion tracks (107 DSBs/ $\mu\text{m}$ ) are still higher than the observed structures. Similar results had been obtained using low-energy bismuth and carbon ions and staining for

hMRE11, PCNA or p21, respectively (Jakob *et al.* 2003). In addition, the observed patterns also showed a striking similarity to the  $\gamma$ H2AX signals obtained after high-energy particle irradiation (Desai *et al.* 2005; Jakob & Taucher-Scholz 2005; Asaithamby *et al.* 2008), even though fewer DSBs are expected along the track cores at higher specific energies. Therefore, the similarity of  $\gamma$ H2AX-stained chromatin domain distributions despite the increasing LET in our experiments indicates saturation in the local response of  $\gamma$ H2AX at higher DSB densities. A possible explanation is the overall phosphorylation response of the complete DSB-containing megabase-pair domain (Rogakou *et al.* 1999) independent of the production of one or more DSBs in such a domain. Gaps observed in this case most likely represent variations in chromatin density and are more likely to be found at the border of intensively stained (heterochromatic) chromatin regions (Fig. 4-1D), in agreement with the observation of Costes *et al.* for high-energy iron ions (Costes *et al.* 2007). Nevertheless, the observed moderate gain in signal intensity in combination with the small but significant difference in focus spacing between carbon- and uranium-ion tracks indicates that, at least for carbon ions (and potentially other ions at an LET around 200 keV/ $\mu$ m), the phosphorylation of H2AX is yet not fully saturated. Starting at 3 to 5 h post-irradiation, clear LET-dependent differences in the amount of focal  $\gamma$ H2AX could be observed along the ion trajectories, indicating a loss of foci in the case of carbon ions (Fig. 4-2), whereas the focus number remained more stable in the case of uranium ions (Fig. 4-3). The observed loss of foci along the trajectories might be due to repair processes and together with nuclear rotation made an assignment of residual foci to defined ion tracks more difficult at later times. Because the quantitative analysis depends on the geometric definition of the trajectory, this leads to a slight underestimation in the values of the interfocal distance and radial dispersion for the carbonion data shown in Fig. 5 for 18 h post-irradiation. However, visually evident focus loss in the case of carbon ions is supported by the increase in the focal distance parameters in the quantitative analysis (Fig. 5). Taken together, these results show repair of DSBs after carbon-ion irradiation, which leads to the dephosphorylation of H2AX in the surrounding chromatin domains. In contrast to the evidence of disintegration of the carbon-ion tracks, the generated  $\gamma$ H2AX streaks resulting from high-LET uranium-ion irradiation preserve their pattern at least up to 18 h. The observed LET-dependent differences in focus loss support the concept of less dense and less complex lesions that are more likely to be repaired in the case of carbon ions, whereas the foci that persist after uranium-ion traversals are indicative of the formation of so-called multiple damage sites that are more difficult to repair (Goodhead 1994; Sutherland *et al.* 2000; Paap *et al.* 2008). However, one must be particularly careful in using the number and loss of  $\gamma$ H2AX foci as a direct measurement of repair kinetics for individual DSBs under these conditions. First, the initial number of foci clearly does not represent the number of DSBs, as shown in this study, and second, loss of a focus might occur only after the repair of the last break of that particular domain if there had been more than one initially. The formation of multicentered focus clusters were seen only occasionally in normal human fibroblasts, suggesting that LET-dependent differences in the pattern of  $\gamma$ H2AX staining over time most likely reflect the loss of foci due to repair rather than merging of foci. For a better resolution of foci induced shortly (1 h) after irradiation with high-LET uranium ions,  $\gamma$ H2AX was replaced by microfocal markers like XRCC1 or RPA. Counting of these markers also led to focus numbers of around one per  $\mu$ m track length (Figs. 4-3 and 4-6). At this density, the counting is not limited by the

resolution of the confocal microscope. Therefore, the detected protein aggregates also do not represent or approach the expected number ( $>100$  DSBs/ $\mu\text{m}$  for uranium ions) of individual DSBs, which would lead to a more or less continuous streak due to optical limitations, thus providing a discrepancy to the previous suggestion of Bekker-Jensen *et al.* (2006) after laser microirradiation. In most cases one microfocus can be found per  $\gamma\text{H2AX}$ - or 53BP1-stained megabase-pair domain after heavy-ion irradiation, but occasionally two to three were observed. The formation of  $\gamma\text{H2AX}$  domains containing more than one microfocus has been described after  $\alpha$ -particle irradiation (Aten *et al.* 2004) or  $\gamma$  irradiation (Falk *et al.* 2007) and can be interpreted as the formation of repair clusters. It is not clear whether this accumulation is an event of several lesions occupying the same chromatin hole formed by decondensation by chance, as suggested by Falk *et al.* (2007). Alternatively, it may represent a functional unity like the repair factories observed in yeast cell nuclei (Lisby *et al.* 2003; Lisby & Rothstein 2004). If a single repair factory would comprise the megabase-pair domain of  $\gamma\text{H2AX}$  or 53BP1 as a functional unit, it seems questionable whether the individual DSBs inside could be discriminated by normal light-microscopic resolution after high-LET irradiation. The observed distinguishable microfoci inside a single chromatin megabase-pair domain are separated by several hundred nanometers; this distance is probably too large to be covered by a common repair factory during lesion processing. On the other hand, because these microfoci do not represent individual DSBs (see above), it is tempting to speculate that each microfocus may represent a type of repair factory within a chromosomal subunit, where the actual processing of lesions is taking place. This repair factory might then contain multiple DSBs, which cannot be resolved by standard light microscopic techniques, or, less likely, might point to a sequential processing of individual lesions. The chromosomal subunit containing these microfoci would be similar in size to the ones in a yeast cell nucleus, where repair factories have been described for DSB processing (Lisby *et al.* 2003), and could be reached by fast constrained motion without the need for a long-range movement. However, in mammalian cells, they are unlikely to exist on a larger nuclear scale, enforcing enhanced lesion mobility. This view would fit both the observed general positional stability and a fast confined (below  $1\ \mu\text{m}$ ) motion (Marshall *et al.* 1997; Mearini & Fackelmayer 2006) enabling the contact of lesions in the near vicinity.

Detailed clarification of this point is the subject of further ongoing live cell microscopy studies. We must stress that these types of cluster formation (several microfoci inside a  $\gamma\text{H2AX}$ -stained domain and multiple DSBs in a microfocus) are not represented in the cluster parameter of our quantitative image analysis at present (Fig. 5), because in the first case it does not necessarily lead to overlapping  $\gamma\text{H2AX}$  domains with clearly separated intensity centers and in the second case it cannot be resolved.

The visual observation of structural changes within the trajectories (Figs. 4-2, 4-3 and 4-6) and the quantification of the radial spreading (Fig. 4-5) led to the conclusion that, in addition to the loss of foci observed for carbon ions, there was only a limited radial spreading observed in AG1522 human fibroblast cells, which is indicative of a very moderate motion of damaged chromatin sites. This holds true even if the cells move and rotate. There was little difference in the  $\gamma\text{H2AX}$  distribution and the mobility of DSBs during the first hours post-irradiation between carbon ions with an LET similar to the  $\alpha$  particles used by Aten *et al.* (2004) and uranium ions with an about 70-fold higher LET. In both cases, there was only a slight and



transient tendency of the formation of bigger, partially overlapping  $\gamma$ H2AX clusters. This was confirmed in our first experiments with ion-irradiated living cells (manuscript accepted for publication) and is in agreement with the findings of others who used living cells where some transient merging of repair protein foci inside a chromatin domain has been described after  $\gamma$  irradiation (Kruhlak *et al.* 2006; Falk *et al.* 2007). After of 10 Gy  $\gamma$  irradiation of mouse embryonic fibroblasts, Kruhlak *et al.* (2006) observed multiple 53BP1-GFP foci in proximity that frequently interacted and separated again during the 50-min observation time. Falk *et al.* (2007) described an occasional merging of NBS1-GFP foci in human MCF7 cells. Whether this merging or temporal interaction reflects an active search for homology in homologous recombination (HR) or a concerted processing in some type of repair factory remains an open question. However, because our fixed samples provide only a static snapshot, it cannot be ruled out that the few  $\gamma$ H2AX clusters observed in our study occurred by chance due to simple constrained diffusion and are not related to DSB processing. From our data, we must conclude that lesion density and complexity have no major influence on chromatin mobility. Therefore, it seems unlikely that high-LET radiation actively triggers a long-range homology search. However, the closeness of multiple DSBs in such a cluster or merged focus might enhance the probability of misrepair of DSB ends leading to a translocation.

To assess the possible influence of the cell type on mobility and clustering as suggested by a previous study (Aten *et al.* 2004), we included HeLa cells in our experiments. To ensure proper assignment of tracks, we irradiated the cells with high-LET uranium ions (Fig. 4-7) and evaluated the changes in the generated  $\gamma$ H2AX streaks with post-irradiation incubation time. Whereas at short times post-irradiation the signal pattern was very similar to that observed in fibroblasts (Fig. 4-1), at later times (10 h), HeLa cells showed a higher degree of variability, leading to the formation of disaggregated tracks in about 25 to 30% of nuclei. This observation may be the result of a greater mobility of the nucleus itself or indicate a subfraction of nuclei with greater internal mobility, as supported by the observed bending of streaks at earlier times (Fig. 4-7, 3 h). The observed greater mobility and variability of damaged DNA sites in HeLa cells compared to the fibroblasts may partly explain the rearrangement seen by Aten *et al.* (2004) after  $\alpha$ -particle irradiation of HeLa cells. One could speculate that this mobility is connected to a certain cell cycle phase. In addition, the greater mobility of damaged chromatin domains in some of the HeLa cells might lead to a loss of the positional stability and subsequent misrepair and might thus be related to elevated genomic instability, a hallmark of tumor cells. However, the observed intra- and internuclear variations of the protein patterns together with the uncertainty of proximal hits make a direct analysis of motion events in fixed samples difficult. This aspect will be addressed in more detail in live cell experiments after low-angle particle irradiation. Despite greater heterogeneity, the mobility in HeLa cells was limited such that during the 10 h observation period, the direction of the original trajectories could still be attributed to the focal patterns in most nuclei. This is in accordance with the general view of a restricted mobility in the course of repair processes (Soutoglou & Misteli 2007). However, the results in HeLa cells do not support the hypothesis of a more restricted mobility of DSBs by extensive H2AX phosphorylation after higher-LET irradiation as proposed by Aten *et al.* (2004). Taken together, the data from the present study lead to the conclusion that in human fibroblasts the structure and the mobility of  $\gamma$ H2AX domains along the trajectories are only mildly affected by the original lesion density over a

wide range of LETs. However, clear differences were seen in the ability of cells to repair DSBs along ion trajectories of different LETs, indicating different lesion complexity. In addition to the staining of distinct foci in the case of the microfocus-forming proteins, none of the DSB marker proteins examined could reproduce or resolve the expected number of DSBs along the ion trajectories for high-LET particles, indicating either a saturation of the response or the staining of only a subset of lesions.

HeLa cells showed a similar  $\gamma$ H2AX distribution but a greater variability in the migration behavior of damaged chromatin domains. All together, these results do not support the hypothesis of damage-induced stiffening after high-LET irradiation.

Whether the observed differences between cell types are a hallmark of cancer cells or reflect the influence of the cell cycle distribution will be a matter of further studies.

## Chapter Five

# Live cell microscopy of ion-irradiated cells describes the positional stability of damage sites

### 5.1 Introduction

Double-strand breaks (DSBs) are considered the most critical cellular lesions induced by ionizing radiation. Even more deleterious is DNA damage generated by heavy nuclei, because it combines DSBs with additional lesions in so-called multiple damaged sites, because of the dense spacing of ionization events (Ward 1994; Goodhead 1994; Krämer & Kraft 1994). Relative little is known about the spatiotemporal organisation of repair events after generation of DSBs, although these events are clearly decisive in determining the “fate” of the damaged cells. In fact, the interaction of DNA lesions leads to chromosomal aberrations, which are eventually responsible for early and late cellular effects. UV micropore or laser microirradiation have been recently used to generate localized DNA damage (reviewed by Lukas *et al.* 2005 and by Taucher-Scholz & Jakob 2007). Heavy nuclei also produce highly-localized DNA damage (Uematsu *et al.* 2007), but in contrast to UV lasers the physical nature of damage generation is the same as for sparsely-ionizing irradiation (X- or  $\gamma$ -rays). Furthermore, the density of DNA lesions (i.e., the number of DNA breaks per unit track length) can be scaled according to the energy and charge of the particle used. These features make heavy ion irradiation a useful tool for the spatiotemporal analysis of repair processes. In addition, understanding of lesion processing following heavy ions is of great interest for hadrontherapy, where charged particles are used to treat solid cancers (Schulz-Ertner & Tsujii 2007), and radiation protection in space, because heavy ions are present in the galactic cosmic radiation and represent a major risk for human space exploration (Cucinotta & Durante 2006; Durante & Cucinotta 2008).

Most of our current knowledge is derived from studies on fixed cells and immunostaining of DSB-flanking  $\gamma$ H2AX histone or other damage response proteins (Jakob *et al.* 2003; Aten *et al.* 2004; Costes *et al.* 2007; Asaithamby *et al.* 2008; Jakob *et al.* 2009a). Recently, a limited “movement” of DNA DSBs associated with chromatin decondensation and protrusion of the DSBs into low-density chromatin was described to occur after  $\gamma$ -rays (Falk *et al.* 2007) or local UV-laser irradiation (Kruhlak *et al.* 2006). Furthermore, Aten *et al.* (2004) discussed the formation of repair clusters after  $\alpha$ -particle irradiation, which requires a substantial motion of damaged chromatin sites.

In contrast, experiments using focused ultrasoft X-rays revealed apparently immobile DSBs (Nelms *et al.* 1998), and our recent data of pattern changes of  $\gamma$ H2AX foci along heavy ion tracks in fixed human cells point to a stable positioning of DSBs (Jakob *et al.* 2009a).

However, data derived from fixed samples have severe limitations for tracking the dynamical behaviour of repair events. Images of fixed and immunostained samples offer only a static view of a selected point in time, thus making the analysis of dynamic changes difficult. To circumvent these limitations, we elected to use live cell imaging covering time

regimes from a few minutes up to several hours after irradiation. We used human osteosarcoma cells (U2OS) stably-expressing GFP-tagged 53BP1. 53BP1 is one of the components of the genome surveillance network activated by DNA DSBs via phosphorylation by ataxia telangiectasia mutated (ATM) protein (Jowsey *et al.* 2007). After irradiation, 53BP1 is readily recruited to the surrounding of DSBs and binds dimethylated lysine 79 of histone H3 via its Tudor domain (Bekker-Jensen *et al.* 2005). 53BP1 had been shown to co-localize with  $\gamma$ H2AX-stained chromatin domains along heavy ion tracks (Asaithamby *et al.* 2008; Jakob *et al.* 2009a). The same osteosarcoma cell line (U2OS) stably-expressing GFP-tagged NBS1 (a member of the DSB processing MRN complex; van den Bosch *et al.* 2003) or HeLa cells expressing Aprataxin-GFP (Gueven *et al.* 2004) were used for the short time mobility measurements at the beamline. These proteins were chosen because they are rapidly recruited to sites of DNA damage after irradiation.

## 5.2 Material and methods

### 5.2.1 Cell culture and irradiations

Human osteosarcoma cells (U2OS) stably expressing 53BP1-GFP were grown on round glass coverslips (40 mm diameter) submersed in 60 mm Petri-dishes at 37 °C, 100% humidity and 5% CO<sub>2</sub> in DMEM (Biochrome, Berlin, Germany) supplemented with 10% FCS and 1% penicillin/streptomycin. Cells were regularly checked to be free of mycoplasma contamination. For the measurement of protein recruitment and short time dynamics at the beamline microscope U2OS cells stably expressing tandem GFP-tagged NBS1 or HeLa cells expressing Aprataxin-GFP were used. These cells were cultivated on polycarbonate foil (18 mm diameter; 40 µm thickness) and irradiated at the beamline microscope as described previously (Jakob & Taucher-Scholz 2005). The irradiation was performed at the UNILAC facility of the GSI Helmholtzzentrum für Schwerionenforschung (Darmstadt) with low energy heavy ions and a fluence of  $2 \times 10^6$  particle/cm<sup>2</sup> (Tab. V-I).

**Table V-I. Irradiation parameters**

Ion	Energy, MeV/n	LET, keV/µm	Dose, Gy	DSBs/µm
<sup>48</sup> Ca	7.4	1,850	5.9	24
<sup>52</sup> Cr	6.5	2,630	8.4	33
<sup>59</sup> Ni (low-angle irradiation)	6.0	3,430	11	45
<sup>150</sup> Sm	4.2	10,290	33	132
<sup>238</sup> U	3.0	14,300	46	184

Particle fluence was  $2 \times 10^6$  particles/cm<sup>2</sup> in all experiments. Calculation of DSBs per µm of track length is based on the assumption of 35 DSBs/Gy (Prise *et al.* 1998) and a nuclear volume of 500 µm<sup>3</sup>.

### 5.2.2 Live cell imaging

For time-lapse live cell experiments, U2OS cells grown on 40-mm round coverslips were irradiated with Ni-ions under a low angle as described (Jakob & Taucher-Scholz 2005). Mock-irradiated cells were used as controls. According to the calculations in Jakob *et al.* (2003) the mean nuclear cross-sections was  $\approx 90$  µm<sup>2</sup> in the case of an angle of 15° under the experimental conditions. Thus, a fluence of  $2 \times 10^6$  particles/cm<sup>2</sup> corresponds to an average of 1.8 traversals per nucleus. For the analysis of the fast motion at the beamline microscope, cells were irradiated perpendicular to the cell layer with low-energy Ca, Cr, Sm, or U ions, respectively.

Live cell observation after irradiation was done in a temperature-controlled Focht chamber (FCS2; Bioptechs-Chromaphor). This chamber was mounted on a Leica IRE2 inverted microscope equipped with a HCXPlanApo 63x/1.32 oil objective and a PCO Sensicam CCD-camera (PCO). An 1.5x internal magnification was used in combination with a 2 x 2 binning of the CCD sensor, leading to a corresponding pixel scaling of 137 nm. During observation, phenol-red free fully supplemented DMEM buffered with 10 mM Hepes was slowly, but continuously, pumped through the chamber. After selection of  $\approx 30$  positions, each position

was automatically revisited at given time intervals and a fluorescence image stack (5 slices at a distance of 0.7  $\mu\text{m}$ ) together with a phase-contrast image (also used for the autofocus routine) was recorded. To avoid the generation of illumination-induced perturbation of cellular processes, especially in the case of GFP-tagged proteins in the vicinity of predamaged DNA, light output was reduced by additional neutral density gray and UV/IR blocking filters and image frequency was adapted to the experimental task. Additionally, irradiated samples were kept in the incubator and imaged after finishing of the time-lapse series for comparison. For the short time observation of Figure 5-1, the beamline microscope was used as described earlier (Jakob & Taucher-Scholz 2005).

Motional analysis was done in ImageJ (<http://rsb.info.nih.gov/ij>). Briefly, live cell imaging datasets were loaded into image5D macro (Joachim Walter, BIZ Universität München, Germany) and maximum z projection was performed. Translational and rotational motion of whole nuclei was corrected by rigid body transformation (Macro StackReg by Philippe Thévenaz, Biomedical Imaging Group, Swiss Federal Institute of Technology Lausanne) (Thévenaz *et al.* 1998). The resulting motion of foci should thus be independent on nuclear motion. Tracking of individual focal structures was done by the macro M-TrackJ (Erik Meijering, Biomedical Imaging Group Rotterdam, Erasmus MC, Netherlands). Briefly, the intensity center of each selected focus was tracked over time and the trajectory and displacement of each focus relative to its original position were calculated. In total 140 foci from 24 nuclei were analyzed over the whole time frame (12 h) in the Ni experiment and 60 foci in a similar number of nuclei were measured for the X-ray data. Measured values were exported to Excel and mean MSD was calculated as the squared displacement of these structures. Diffusion coefficients for a “random Brownian motion” of individual foci were calculated from linear regression of MSD according to  $\text{MSD}(\Delta t) = 6D \times \Delta t$  (Bornfleth *et al.* 1999) and multiplying D by a correction factor of 1.22 taking into account the 2D projection to 3D conversion (Chubb *et al.* 2002).

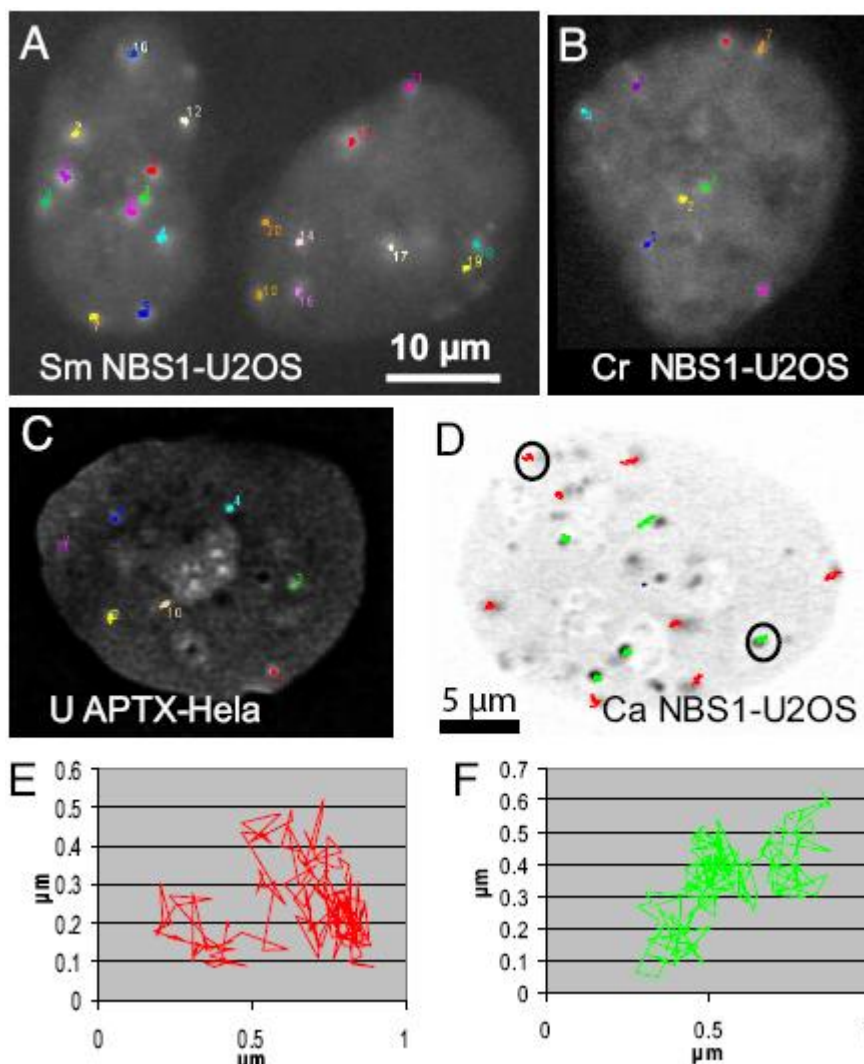


**Figure 5-1.** Damaged chromatin sites show a fast constrained motion during the first minutes after irradiation. Live cell imaging directly at the beamline allowed measuring the motion of radiation-induced foci at sites of ion traversals (perpendicular to the cell layer). Time-lapse imaging started shortly before irradiation. Motional tracks were recorded 5 s after irradiation up to 30 min. (A–C) The small-scale spatially confined quivering movement of NBS1-GFP or Aprataxin-GFP foci (superimposed motional tracks; different colors and numbers represent individual measured trajectories) in U2OS or HeLa-cells, respectively, during a 5-min observation time (one frame every 5 s) after the irradiation with charged particles. Motion of foci was within 0.5  $\mu\text{m}$  in all cases (A: U2OS NBS1-GFP; Sm 10290 keV/ $\mu\text{m}$ ; B: U2OS-NBS1-GFP; Cr 2630 keV/ $\mu\text{m}$ ; and C: HeLa Aprataxin-GFP; U 14,300 keV/ $\mu\text{m}$ ). (D) Motion of NBS1-GFP foci in U2OS cells during a time course of 30 min (1 frame every 10 s) after the irradiation with Ca ions (1,850 keV/ $\mu\text{m}$ ). Superimposed red trajectories indicate movement of radiation-induced foci; green trajectories indicate movement of preirradiation aggregates. (E and F) Enlargement of 2 trajectories of D (marked by circle) showing the quivering nondirected motion on a scale  $\sim 1 \mu\text{m}$ . Motion of the whole nucleus was compensated by alignment of the center of intensity (indicated by the blue dot-like trajectory in D). No significant difference in motional scale could be observed between the traversal-induced foci containing DSBs and preirradiation aggregates.

## 5.3 Results

### 5.3.1 Fast Confined Movement of Damaged Chromatin Within Minutes After Irradiation

For the short time mobility analysis, we selected the GFP-tagged proteins Aprataxin and NBS1, that had shown a fast accumulation at sites of ion impacts reaching maximum intensities  $\approx 1$  and 2 min after irradiation, respectively. In addition, the selected proteins showed a more pronounced and therefore better traceable formation of ionizing radiation-induced foci (IRIF) at ion-induced lesions compared with the also fast accumulating DNA-PK<sub>cs</sub> (Uematsu *et al.* 2007). These facts made these proteins especially suitable for following up the early kinetics of the damaged DNA. Time-lapse imaging starting shortly before irradiation showed motion of IRIF already 5 s after irradiation. In Figure 5-1, the motion of individual NBS1 or Aprataxin foci is visualized with colored trajectories. Note that each “focus” in Figure 5-1 actually corresponds to a short track perpendicular to the cell plane including several IRIF and comprising varying numbers of DNA lesions. An estimate of the density of the DNA DSBs is given in Table V-I based on the number of DSBs/Gy from Jakob *et al.* (2005a). No major radiation-induced dislocation of damaged chromatin could be observed, with the foci showing only very limited spatial transitions. For that reason, the



superimposed trajectories appear as a spot at this spatial resolution during the first 5 minutes (Fig. 5-1 A–C). The observed fast dislocation was in the order of  $<0.5 \mu\text{m}$ , confirming previous results (Prise *et al.* 1998; Taucher-Scholz & Jakob 2007). The motional extent did not depend on the chosen protein as Aprataxin and NBS1 (Fig. 5-1 A–C) showed a very similar behaviour. There was also no significant difference in foci movement for the different tumor cell lines used (U2OS or HeLa). During analysis of this small-scale displacement in more detail up to 30 min, the path of the dislocation of the damage sites marked by NBS1 showed quivering motion (Fig. 5-1D). This behaviour resembles a fast nondirected confined random motion. The dislocation covered a space of  $\approx 0.5 \mu\text{m}$  in diameter (Fig. 5-1D, red trajectories) with jumps of  $\approx 0.075 \mu\text{m}$  between each frame (10s). The extent and path of motion were more clearly visualized by enlarging a sample trajectory (Fig. 5-1E). The motional trajectories of radiation-induced foci of NBS1-GFP were similar in respect to confinement and speed to those of observable pre-irradiation aggregates in the same nucleus (Fig 5-1D, green trajectories, and F). In addition, similar values have been described in the literature for the motion of undamaged chromatin locations (Marshall *et al.* 1997; Görisch *et al.* 2004).

### 5.3.2 Slow Migration of Damaged Chromatin

To facilitate the dynamic analysis of damaged chromatin domains, we generated long damage streaks in cell nuclei by using low angle Ni-ion irradiation as described in Jakob *et al.* (2003).

The use of live cell microscopy in a temperature controlled Focht-chamber and iterative revisiting of selected fields at a specialized microscope remote from the irradiation facility, allowed the frequent observation of ion trajectories inside the cell nuclei for several hours, limited mainly by cell migration. 53BP1-GFP showed irradiation dependent foci formation along the ion trajectories in living cells (representative images in Fig. 5-2A, 5-4A, 5-5) reaching a maximum of intensity within 10 min (own unpublished results). The streaks in the live cell experiments clearly showed a non-homogeneous, punctuate pattern of 53BP1 aggregation, similar to fixed and immunostained samples (Jakob *et al.* 2009a). At a radiation linear energy transfer (LET) of  $3430 \text{ keV}/\mu\text{m}$ , a traversing Ni ion is expected to produce 45 DSBs per  $\mu\text{m}$  of track, based on the estimation of 35 DSBs/Gy (Prise *et al.* 1998). The presence of a gap structure after high LET Ni irradiation in living U2OS cells thus confirms that this pattern is not introduced by fixation artefacts, but represents a biological phenomenon.

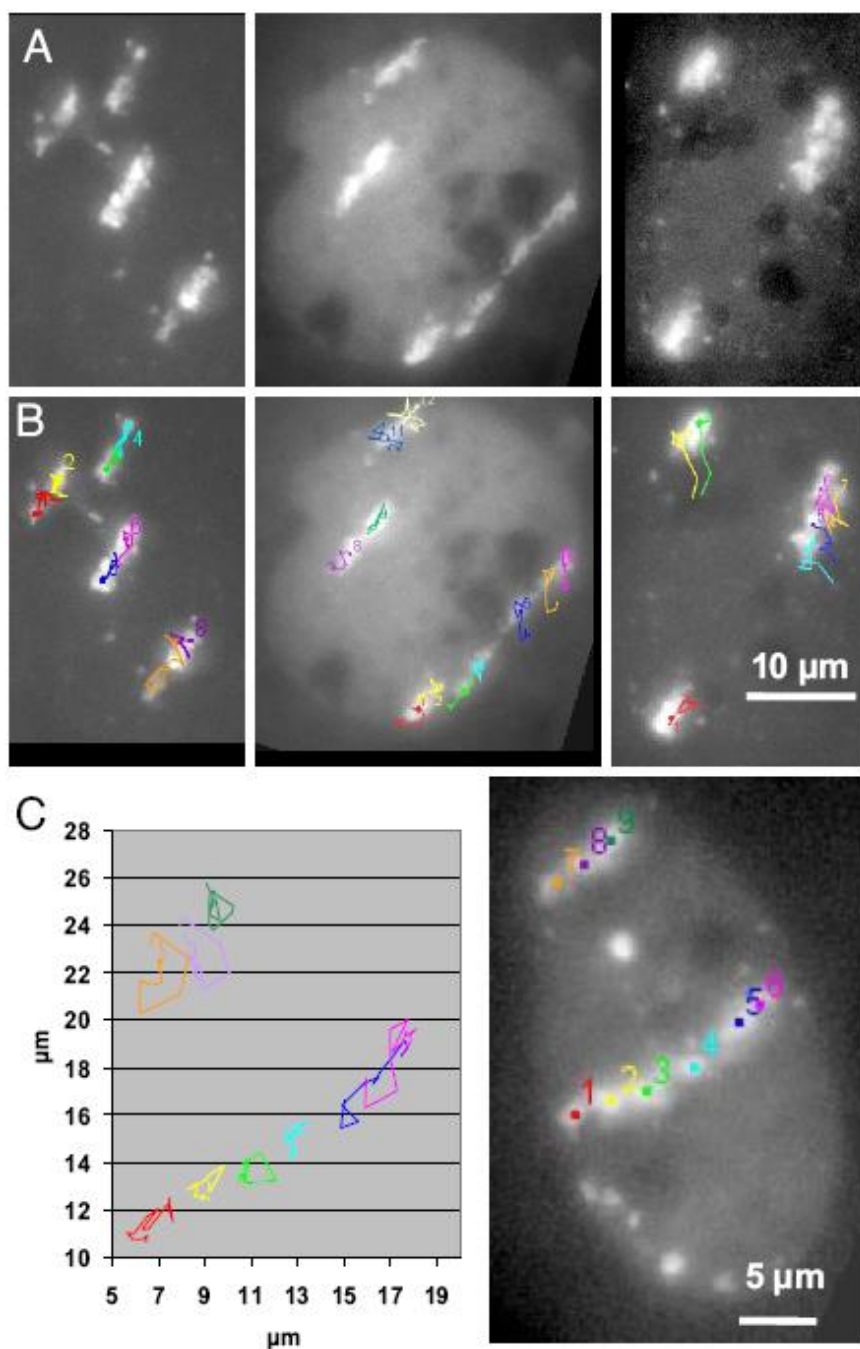
---

→

**Figure 5-2.** Motion of damaged chromatin sites inside individual trajectories generated by low-angle Ni irradiation (LET  $3,430 \text{ keV}/\mu\text{m}$ ). Live cell imaging of 53BP1-GFP in U2OS cells in a Focht chamber allowed measuring the motion of radiation-induced foci along ion trajectories  $>12\text{h}$ . (A) Representative images of 53BP1-GFP expressing U2OS nuclei traversed by Ni-ions 24–30 min after irradiation. Along the sites of ion trajectories, accumulation of foci can be observed forming a streak pattern. (B) Individual motional trajectories of foci inside these nuclei are represented by different colors and numbers and are super-imposed on the image shown in A. These overlays indicate the course of individual foci inside an ion track during the observation time of 12 h. In most cases only moderate displacements were observed, indicating the quite stable positioning of damaged chromatin. (C) Magnification of the motion of individual foci inside the traversal-induced streaks (*Left*) of a typical nucleus (*Right*) during the 12-h observation time. The tracks show a largely nondirected motion with a slight preference along the particle path. The overall displacements were in the range of 2 to 4  $\mu\text{m}$  (12 h).



The 53BP1 streaks could be identified beside a substantial migration (and partially rotation) of the whole cell nucleus, which was compensated by rigid body transformation (see Material and Methods), indicating a general positional stability of the foci. However, substantial motion of substructures could be frequently monitored (Fig. 5-2C). For each analysed focus of a trajectory in a nucleus, a number and a color were assigned as indicated in Figure 5-2B (colored overlays). The foci in these trajectories yielded a displacement of less than 3  $\mu\text{m}$  during the first 10 h of observation for more than 80 % of the observed foci and only about 2% of the foci displayed a migration exceeding 5  $\mu\text{m}$ . The behaviour of a typical ion- induced 53BP1 streak is displayed as a time series in Figure 5-4A, showing a moderate displacement of individual foci in the range of 2-3  $\mu\text{m}$  during the 12h observation time. The Mean Square Displacement (MSD) of the damaged chromatin sites calculated by linear regression of the



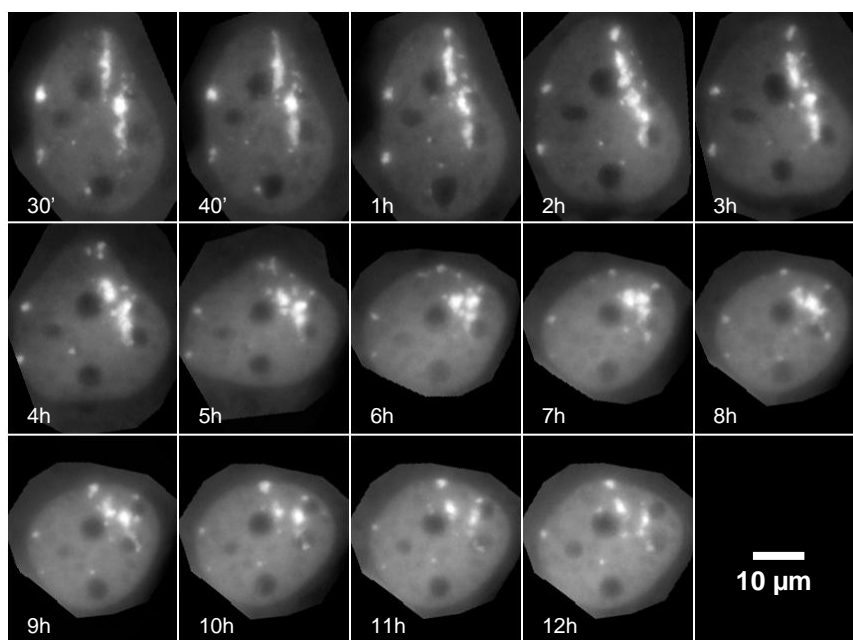


**Figure 5-3.** Observed larger changes of damaged chromatin patterns are frequently associated with changes of nuclear morphology. Nucleus of a 53BP1-GFP expressing U2OS cell after low-angle Ni irradiation displayed as consecutive images over time (12 h). This cell shows major displacements of 53BP1 foci and a contraction of the streaks accompanied and probably forced by major deformations of the whole nucleus.

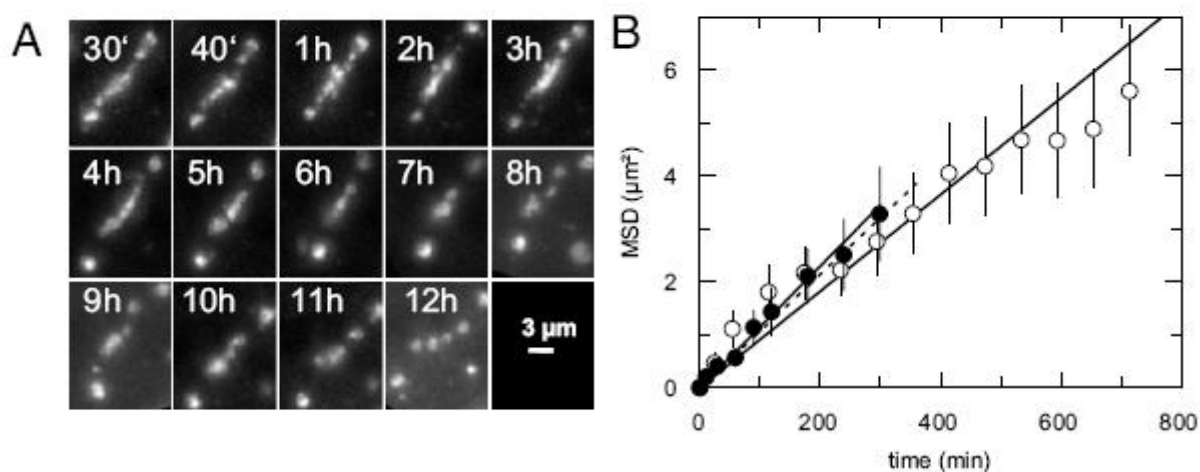


**Figure 5-4.** Quantitative analysis and comparison of the motion of DSBs after low and high LET irradiation. (A) Time-dependent changes of a single ion-induced 53BP1-GFP streak showing the typical motional behavior of individual foci along the trajectory over the time course of 12 h after irradiation. From the displacements of individual foci the MSD values were calculated after correcting for nuclear translocation and rotation. (B) Calculation of the MSD from the experiments described in Figs. 2 and 6. Motion of 140 or 60 foci were analyzed for the Ni (○) or X-ray (●) experiment, respectively. Error bars represent the 95% confidence interval. Calculation of the linear fit gives values of  $0.55 \pm 0.04 \mu\text{m}^2/\text{h}$  for high LET nickel and  $0.69 \pm 0.04 \mu\text{m}^2/\text{h}$  for X-rays. The data points used for the calculation of the MSD show a slight bending in the case of the Ni ion irradiation at later times, potentially indicating a larger-scale confinement set by chromosomal territories or the nuclear volume itself. If we restrict the values for the nickel experiments to the time frame of the first 6 h (like the X-ray-data), the linear fit (dashed line) yields a MSD of  $0.64 \pm 0.08 \mu\text{m}^2/\text{h}$ , very similar to the X-ray data.

displacement vectors was  $0.55 \pm 0.04 \mu\text{m}^2/\text{h}$  in the U2OS cells (Fig. 5-4B). From this MSD, a diffusion constant of about  $0.31 \times 10^{-12} \text{ cm}^2/\text{s}$  can be inferred. Larger displacements or significant compaction events were generally accompanied by morphological changes of the shape of the nucleus leading to an internal rearrangement and/or a loss of observed foci during the observation period (Fig. 5-3). Nevertheless, in some rare cases, large scale motion of damaged sites could be observed without dramatic changes of the nuclear outline (Fig. 5-5A).

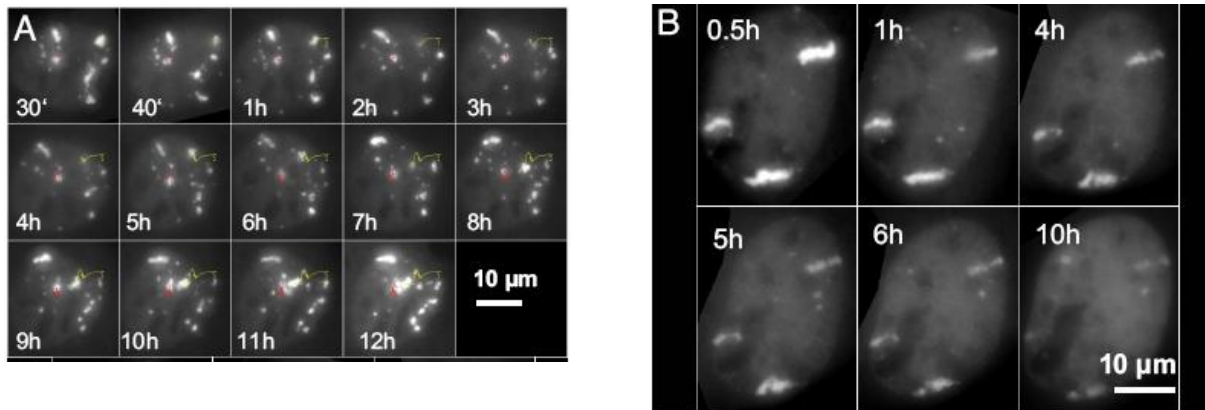


**Figure 5-5.** The migrational activity of damaged DNA domains after irradiation covers a broad range in individual nuclei. Samples of 53BP1-GFP-expressing U2OS cells displayed as consecutive images over time (12 h) after low-angle Ni irradiation. (A) Rare case of observed larger displacements of 53BP1-GFP foci without major deformations of the whole nucleus or changes in nuclear morphology. The long-range migration from a peripheral site to the interior of 1 single spot is marked by the yellow trajectory. Other foci like the one marked in red remained stably positioned. Variations in signal intensities of the tracked spot are due to migration out of the focal planes. (B) This particular nucleus shows only very minor changes of the short streak of Ni-induced 53BP1 foci. Both the absolute position and the internal pattern are maintained during the observation time.

In this particular case, a single spot from the peripheral region moves to the interior over a distance of about  $7 \mu\text{m}$  (Fig. 5-5A; yellow signal trajectory) whereas other foci (e.g. indicated by red trajectory) stayed quite stable. The intensity variations of the tracked focus are due to motion in z-direction and a slight focal drift. Other nuclei, as the one displayed in Figure 5-5B showed no variations during the observation period, with only very minor changes both in the nuclear positioning and appearance of the 53BP1 signal.

### 5.3.3 Repair Clusters

As no large displacement of damaged chromatin domains were observed in general after heavy ions, we tested whether merging of nearby foci would occur (“repair clusters” or “repaurosomes”). The living U2OS cells showed no general tendency to group the individual damaged domains into repair clusters (Fig. 5-2C, 5-4A, 5-5). Nevertheless, a trend for an enhanced migration along the ion trajectory could be observed (evident in Fig. 5-2C lower track). This behaviour led in some cases to the temporal observation of cluster formation (Fig. 5-6 and Fig. 5-7). In the selected nucleus of Figure 5-6A, the development of a more compact form of the 53BP1 aggregations resembling the formation of repair clusters could be observed. In the nucleus in Figure 5-6B, after a transient compaction (e.g. 3h to 9h) the foci pattern turned back to more or less the original streaks of the ion trajectory (Fig. 5-6B, most

obvious at 11 hours; streaks marked by arrows). Thus, the clustering/merging of distinct foci along the tracks was only apparent during the intermediate times in this particular nucleus. In general, this type of observations might point to a higher mobility of damaged chromatin sites along the ion trajectory compared to the perpendicular (radial) direction.

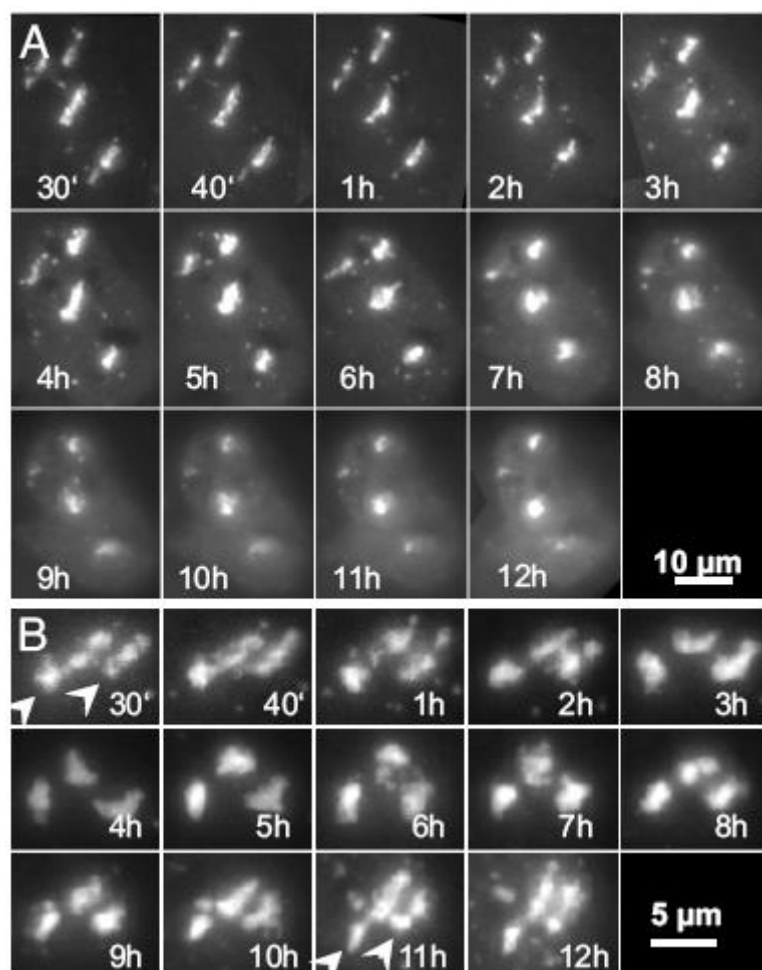


**Figure 5-6.** Motion of damaged chromatin sites inside individual Ni-ion trajectories points to a preferential motion within the track extension. 53BP1-GFP in U2OS cells after low-angle Ni-ion irradiation are displayed as consecutive images over time. Besides the preservation of the general local nuclear positioning of the streaks, motion could be observed affecting the track structure during the 12-h observation time. (A) In addition to the separation of focal structures in some cases this leads to the visualization of clustering. (B) A transient condensation of the 53BP1 foci resulting in the deformation of the original streaks (arrows at 30') into compact structures (3–9 h). After 9 h a decondensation phase is apparent, establishing again a streak pattern (arrows at 11 h) very similar to the original one.

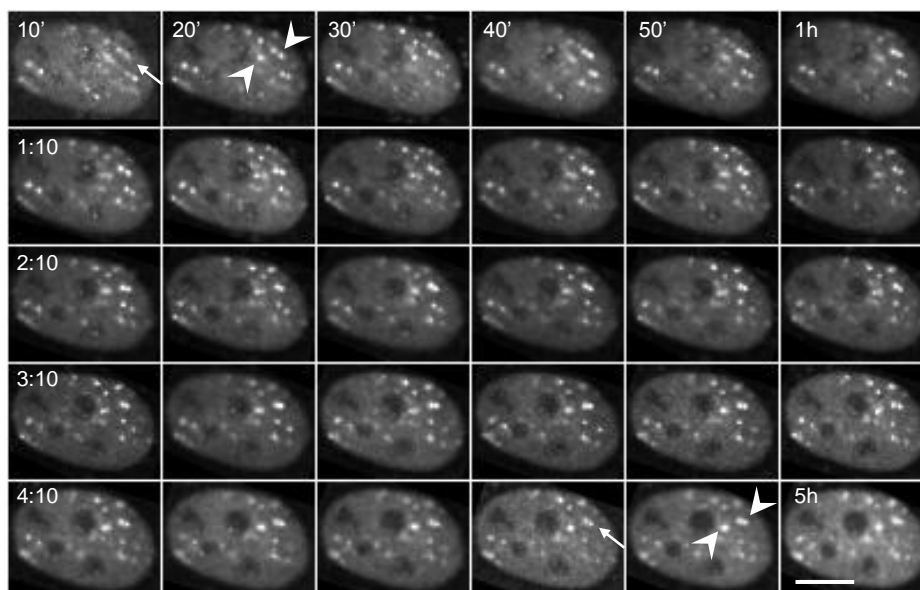


**Figure 5-7.** Motion of NBS1-GFP aggregates inside individual trajectories confirms the stable positioning of damaged chromatin. Live cell imaging of NBS1-GFP in U2OS cells after the irradiation with Krypton ions (LET 5,100 keV/\_m). Thirty consecutive images (frame every 10 min) covering 5h of observation and showing only a moderate displacement of damaged chromatin sites (comparing the position of the two foci marked by arrowheads). Also here, a slightly preferential motion within the linear track extension was observed (see track marked by arrow). Translation and rotational motion of the whole nucleus was compensated by rigid body transformation. (Bar: 10  $\mu$ m.).

### 5.3.4 Extent of Motion of Damaged Chromatin Does Not Depend on DSB Density

In order to assess the influence of DSB density on the mobility of damaged chromatin domains, we compared densely ionizing Ni-ions (Tab. V-I) to sparsely ionizing X-rays. After 2 Gy X-rays, most radiation-induced 53BP1 foci gained intensity 20 to 40 min post-irradiation, but in contrast to ion irradiation were not yet clearly visible at the first time-point (10 min) examined (Fig. 5-8B). Analysis of the motion of selected X-irradiation induced 53BP1 foci yielded a similar dynamical behaviour of damaged chromatin sites after sparsely ionizing irradiation (Fig. 5-8; motion of individual foci indicated by superimposed colored trajectories) compared to the irradiation with low energy Ni ions (Fig. 5-2). Nevertheless, loss of foci, most probably due to repair events, restricted the number of foci observable over longer times after X-rays. Notably, MSD ( $0.69 \pm 0.04 \mu\text{m}^2/\text{h}$ ; Fig. 5-4B, black dots) and diffusion coefficient ( $0.38 \times 10^{-12} \text{ cm}^2/\text{s}$ ; Fig. 5-4B, solid line) for X-rays were also similar to the heavy ion data, especially if we restrict the analysis to the first 5 to 6 hours (Fig. 5-4B dashed line), as in the X-ray experiment. In this case a MSD of  $0.64 \pm 0.08 \mu\text{m}^2/\text{h}$  and a diffusion constant of around  $0.36 \times 10^{-12} \text{ cm}^2/\text{s}$  were calculated for the Ni ion data.

The results for the motional analysis obtained in this live cell study are not dependent on the selected 53BP1-GFP protein construct. Similar results could be obtained using NBS1-GFP expressing U2OS cells after irradiation with krypton ions (LET 5100 keV/ $\mu$ m; Supplemental Fig. 5-2), thus confirming that the experimentally addressed motion is associated with the motion of chromatin sites damaged by irradiation.

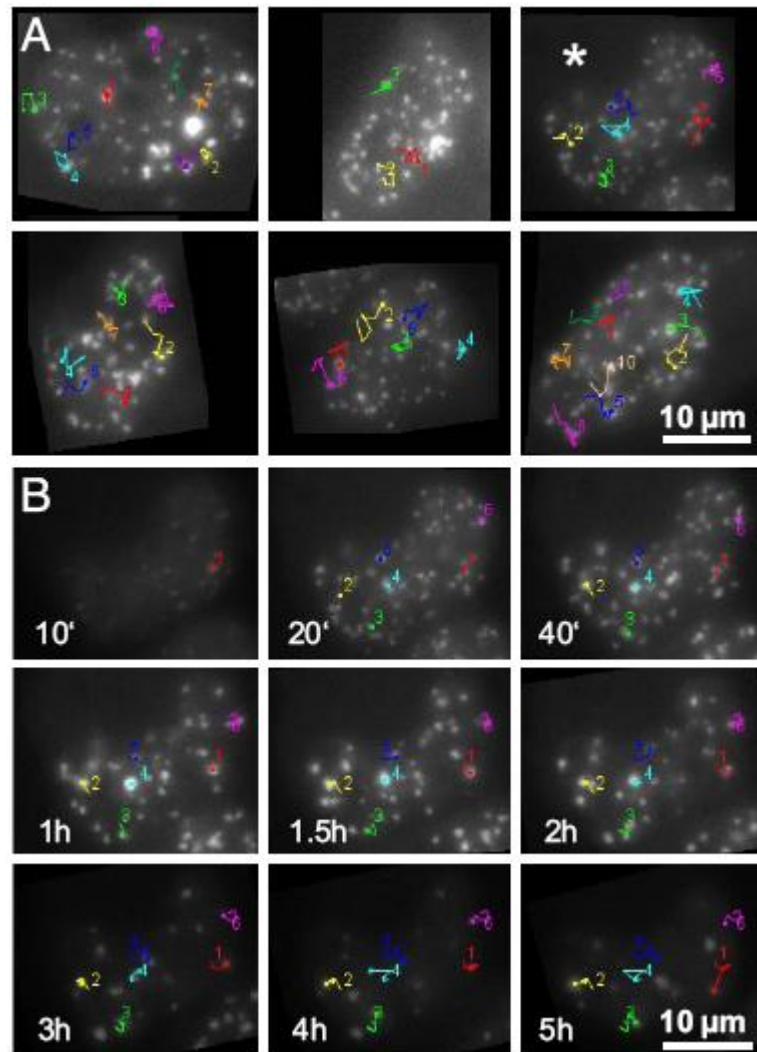


**Figure 5-8.** Motion of damaged chromatin after sparsely ionizing radiation. Live cell observation of 53BP1-GFP in U2OS cells after irradiation with 2 Gy X-rays imaged  $\leq 5$  h after irradiation incubation. (A) Superimposed trajectories on the images of representative nuclei (20 min after irradiation) indicate the course of individual foci during the observation time. In most cases only a moderate displacement was observed indicating the quite stable positioning of DSBs. Displacements were similar to the ones observed after high LET irradiation. (B) Consecutive images of 1 nucleus (A, \*) showing the slower accumulation of 53BP1 after X-rays that is hardly visible 10 min after irradiation (first image). Later, most foci disappear because of ongoing repair processes, thus restricting the observation time.

## 5.4 Discussion

Current knowledge on chromatin mobility has been recently reviewed (Soutoglou & Misteli 2007), leaving still several open questions regarding the dynamical behaviour of damaged chromatin domains. As shown previously by our group and others (Jakob *et al.* 2003; Aten *et al.* 2004; Desai *et al.* 2005; Costes *et al.* 2007; Asaithamby *et al.* 2008), traversals of charged particles lead to the localized accumulation of several repair related proteins and the formation of phosphorylated H2AX in the nucleus, referred to as ionizing radiation-induced foci (IRIF). Charged particles produce similar biological damage as X- or  $\gamma$ -rays, but the lesion density increases by increasing the LET (Krämer & Kraft 1994; Cucinotta & Durante 2006): the resulting multiple damaged sites are thought to be involved in misrepair and represent the main lesions leading to early and late radiation effects (Goodhead 1994; Durante & Cucinotta 2008).

As the quantification of small spatial changes is difficult to address in static snapshots obtained from fixed cells due to the inter- and also intranuclear variability of observable patterns, here, for the first time, we used live cell microscopy as a more direct approach to visualize and measure the dynamics of damaged DNA sites after charged particle and sparsely ionizing irradiation. We directly visualized the stable positioning of damaged DNA sites by observation of foci of the GFP-tagged repair related proteins Aprataxin and NBS1 (Fig.15) or XRCC1 (data not shown), during the first seconds and minutes after ion impacts. The lack of a long range motion up to 30 min post-irradiation (Fig. 5-1 D to F) for different proteins indicates that this result is not depending on the particular chosen protein, but rather represents a general feature of the damaged chromatin site, where the proteins are bound to. Noteworthy, the small range of motional activity observed allows only for a rather small extent of chromatin remodelling during repair, like a local decondensation as described recently (Kruhlak *et al.* 2006; Falk *et al.* 2007). However, we could observe a very fast spatially confined motion on a scale of less than 1  $\mu\text{m}$ , most likely representing the normal Brownian type motion of undamaged chromatin (Görisch *et al.* 2004; Mearini & Fackelmayer 2006; Chubb *et al.* 2002), but demonstrating that our experimental system is able to detect and resolve this range of small dynamical responses. A similar fast confined and radiation-independent motion was observed in pre-irradiation aggregates of NBS1-GFP (Fig. 5-1F), which could not be discriminated from irradiation-induced foci in terms of motional behaviour. These results are in agreement with our earlier observations (Jakob & Taucher-Scholz 2005), where this type of fast radiation-independent confined quivering motion was also monitored by fluorescently marked DNA sequences (scratch replication labeling) both at putative sites of ion traversals and at more remote areas of the nucleus. They also support recent reports in mouse embryonic fibroblasts exposed to  $\gamma$ -rays. Imaging of multiple 53BP1-GFP foci in close proximity, frequently interacting and separating again, yielded a MSD of around 0.9  $\mu\text{m}^2/\text{h}$  during the 50 min observation time (Kruhlak *et al.* 2006). In a recent study, the mobility of telomeres was found to be unaffected by irradiation (Dimitrova *et al.* 2008).

The streaks of particle-induced foci in the live cell experiments are similar to those observed for endogenous 53BP1 in fixed and immunostained cells (Jakob *et al.* 2009a), indicating a physiological response of the 53BP1-GFP construct. In this previous study, despite a generally very similar appearance of traversal-induced streaks at short time post-irradiation, different cell types (normal human fibroblasts and HeLa cells) revealed differences in the

spreading and diversity of patterns during longer incubation times, with fibroblasts showing a greater positional stability of the damaged DNA. Using live cell imaging, we were now able to quantify this motion in U2OS cells yielding MSDs and diffusion coefficients that were similar for densely and sparsely ionizing radiation, and within the range of diffusion constants found in the literature for undamaged chromatin ( $0.1$  to  $0.6 \cdot 10^{-12}$  cm<sup>2</sup>/s for HeLa and neuroblastoma cells) (Bornfleth *et al.* 1999; Edelmann *et al.* 2001). Recently, Wiesmeijer *et al.* (2008) described the mobility of non-damaged chromatin of U2OS cells measured by photoactivation of Pa-GFP H4. The maximal dispersion after 2h was described to be about 2  $\mu$ m and chromatin with different degrees of folding showed equal mobility. In addition, no significant differences in chromatin movement between cells in G1, S and G2 were observed (Wiesmeijer *et al.* 2008). Our data are in full agreement with these results and point to a non-altered migration behaviour of damaged chromatin after ionizing irradiation. Occasionally, we observed foci displacements after Ni irradiation exceeding 5  $\mu$ m in the 12h interval, but these events were occurring in less than 2% of the observed foci only. We have to point out here, that due to restriction of the optical resolution we are not able to measure the motion of individual DSBs inside a single stained mega basepair domain represented by a focus. Nevertheless, this type of movement would not contribute significantly to the long range motional activity of the whole damaged domain. Analyzing the changes in the 53BP1 streaks formed along the trajectories of the traversing ions, we can draw the conclusion that DSB processing is not associated with a directed transition of damaged sites over a larger distance. This is in accordance to earlier data showing that after 1.6 Gy of  $\gamma$ -irradiation, the majority of foci stayed near sites of their origin and did not noticeably move (Falk *et al.* 2007). Whether the slightly enhanced motion along the ion trajectory observed in our experiments (Fig. 5-2C) is related to a 53BP1 dependent increase in mobility as recently reported for unprotected telomeres (Dimitrova *et al.* 2008) remains the matter of further studies.

The lack of evidence for large-scale movements of DSBs in live cell imaging is consistent with the current models of nuclear architecture and formation of exchange-type chromosome aberrations, which require interaction of distinct DSBs (Cornforth 1998). The irradiated cell nucleus was erstwhile regarded as a "bag of broken chromosomes" with the severed ends free to move around and find partners with which to form illegitimate reunions (Savage 1993). This view was challenged by the studies on nuclear architecture, providing evidence that chromosomes occupy localized domains with limited movement (e.g. Meaburn *et al.* 2007). Moreover, the increased translocation frequency involving genes that are in close proximity in the interphase nucleus, such as the RET/PTC inversion in thyroid cells (Nikiforova *et al.* 2000), lend support to the so-called "contact-first" hypothesis, where it was supposed that the damaged chromatin must co-localize at the time of exposure for the exchange to occur (reviewed in Cornforth 2006). Our results in live cells show that the DNA breaks produced by radiation have limited diffusion in the nucleus. Is this consistent with the formation of radiation-induced chromosomal rearrangements? In fact, under the assumptions of limited movements and small interaction distance of DSBs, mathematical models of chromosome aberration formation are able to reproduce accurately the experimental data obtained after exposure to both sparsely ionizing radiation (Sachs *et al.* 1997; Wu *et al.* 2001; Hlatky *et al.* 2002; Cornforth *et al.* 2002) or heavy ions (Friedland *et al.* 2008; Ballarini *et al.* 2008). Besides, recent data on the human interphase chromosome territories suggest that the intermingling of different domains may be much higher than previously thought (Branco &



Pombo 2007). Therefore, increased mobility of the damaged chromatin is not required to reproduce the dose- and radiation quality-dependence of the yield of chromosomal exchanges introduced by ionizing radiation.

## Section C

### **Application of ion-induced foci patterns and their dynamic behavior within heterochromatin**

#### **Chapter Six:**

Biological dosimetry of UVA laser microirradiation based on the comparison of DNA damage patterns

- Introduction (p. 55)
- Material and methods (p. 57)
- Results (p. 61)
- Discussion (p. 68)

#### **Chapter Seven:**

DNA lesions within heterochromatin induce phosphorylation of histone H2AX and are expelled to euchromatic regions

- Introduction (p. 73)
- Material and methods (p. 74)
- Results and discussion (p. 76)

## Section abstract

The induction of localized DNA damage within a discrete nuclear volume is an important tool in DNA repair studies. Both charged particle irradiation and laser microirradiation (LMI) systems allow for such a localized damage induction, but the results obtained are difficult to compare, as the delivered laser dose cannot be measured directly. Therefore, we revisited the idea of a biological dosimetry based on the microscopic evaluation of irradiation-induced Replication Protein A (RPA) foci numbers. Considering that local dose deposition is characteristic for both LMI and charged particles, we took advantage of the defined dosimetry of particle irradiation to estimate the locally applied laser dose equivalent. Within the irradiated nuclear sub-volumes, the doses were in the range of several hundreds of Gray. However, the number of induced foci is below the expected amount corresponding to this high dose (Jakob *et al.* 2003). Thus, local dose estimation is limited by the saturation of the RPA foci numbers with increasing particle doses and even the use of high-resolution 4Pi microscopy did not abrogate saturation as it was not able to resolve single lesions within individual RPA foci. Nevertheless, 4Pi microscopy revealed multiple and distinct 53BP1- and  $\gamma$ H2AX-stained substructures within the lesion flanking chromatin domains. Our results indicate that the local dose delivered by UVA-LMI is extremely high and cannot be accurately translated into an equivalent ionizing radiation dose.

Since DSBs have the potential to induce chromosomal aberrations and carcinogenesis, their correct repair is crucial for genetic stability and depends on a functional damage signaling including formation of  $\gamma$ H2AX (Bassing *et al.* 2002; Celeste *et al.* 2002). This is however absent from heterochromatic chromatin regions after damage induction in both murine (Kim *et al.* 2007) and human (Cowell *et al.* 2007; Vasireddy *et al.* 2009) cells. Additionally, damage signals located adjacent to constitutive heterochromatin compartments are retarded in their repair kinetics (Goodarzi *et al.* 2008; Noon *et al.* 2010) raising questions on the underlying mechanisms. Here we use single ion microprobe irradiation to produce localized DSBs directly within murine heterochromatic compartments, so-called chromocenters (Guenatri *et al.* 2004) and address their early damage response. We demonstrate that, in contrast to widely held belief, H2AX is phosphorylated within this highly compacted chromatin. Strikingly, the damage site is subsequently expelled from the center to the periphery of irradiated chromocenters within ~20 min. While this relocation process is independent of the ataxia telangiectasia mutated protein ATM, the repair of DSBs relocated at the periphery of chromocenters clearly requires this DSB signaling factor. Finally, we describe a local decondensation of chromatin at the sites of ion hits supporting the notion of a physically driven lesion movement in heterochromatin.



## Chapter Six

# Biological dosimetry of UVA laser microirradiation based on the comparison of DNA damage patterns

### 6.1 Introduction

In the last decade, the use of laser microirradiation (LMI) as a tool to generate localized DNA damage has become increasingly popular. In the majority of studies, the recruitment of repair factors specific for DNA double-strand breaks (DSBs) are monitored, for example 53BP1 (1), members of the phosphatidylinositol 3 kinase-related kinases (Bekker-Jensen *et al.* 2006; Mari *et al.* 2006; Uematsu *et al.* 2007) and components of the Mre11-Rad50-Nbs1 complex (Bekker-Jensen *et al.* 2006; Paull *et al.* 2000). As a common marker for DSBs, the phosphorylated form of histone H2AX ( $\gamma$ H2AX) is also frequently monitored in LMI studies (Rogakou *et al.* 1999; Bekker-Jensen *et al.* 2006; Kruhlak *et al.* 2006). In addition to DSB repair, the recruitment of proteins associated to single-stranded DNA (ssDNA) such as the Replication Protein A (RPA) (Bekker-Jensen *et al.* 2006; Sartori *et al.* 2007) or proteins involved in single-strand break (Mortusevicz *et al.* 2007), nucleotide excision (Mortusevicz *et al.* 2006) or base excision repair (Haince *et al.* 2008) have also been the focus of several studies. The different LMI systems used in the respective studies combine all features of a research microscope – e.g. fluorescence and time-lapse imaging – with a very precise irradiation spot size of  $\sim 1 \mu\text{m}$  in diameter. This allows the targeted irradiation of defined subnuclear regions and the simultaneous observation of fast and early damage responses (Kruhlak *et al.* 2006; Mortusevicz *et al.* 2006). The implementation of a relatively low cost 405 nm diode laser in modern confocal laser scanning microscopes further contributes to the availability of such microirradiation systems (Hong *et al.* 2008).

A comparable experimental performance with respect to the discrete localization of DNA damage can also be realized by irradiation with  $\alpha$ - (Aten *et al.* 2004; Williams *et al.* 2007) or accelerated charged particles (Jakob *et al.* 2002; Jakob *et al.* 2003) that induce DNA lesions along the particle trajectories. In combination with the setup of single charged particle microprobes, predefined numbers of particles can be directed to the target volume with a sub-micrometer precision (Heiss *et al.* 2006). Using live cell microscopy at the beamline it is also possible to visualize in real time the recruitment of repair proteins after charged particle irradiation (Jakob *et al.* 2005; Jakob *et al.* 2009b).

In contrast to LMI systems, the spectrum of charged particle-induced DNA damage is better defined and can be correlated with a measurable energy deposition. Nevertheless, particle irradiation does suffer some disadvantages, such as a more complex experimental setup, restricted availability and higher costs compared to LMI systems.

Meanwhile, several different types of laser systems are frequently used to generate localized DNA damage, but a comparison between the obtained data is often difficult as the results depend strongly on the wavelength (Mohanty *et al.* 2002; Kong *et al.* 2009) and the energy (Rogakou *et al.* 1999; Kong *et al.* 2009) of the laser system used. With the application of multiphoton laser systems (Meldrum *et al.* 2003; Mari *et al.* 2006), the duration of laser

pulses also has a major impact on the damage outcome (Berns *et al.* 2000; Kong *et al.* 2009). To unify this diversity of impact factors, it would be useful to find a single parameter correlated with the amount of laser-induced DNA damage. An appropriate parameter could be the absorbed energy as it is typically used for IR. Unfortunately, the measurement of the absorbed laser energy fails due to the thin target of cell monolayers and the low absorption rate of DNA at wavelengths used in most LMI systems (Sutherland & Griffin 1981). To facilitate a comparison of different laser-obtained data, but also between laser and IR data, several attempts were made to estimate the absorbed laser energies. The approaches were based either on calculations using standard absorption rates yielding a locally applied laser dose of more than 800 Gy ( $\lambda = 390\text{nm}$ ;  $10 \text{ MJ/m}^2$ ; Paull *et al.* 2000) or on a biological dosimetry comparing DNA damage responses after LMI and sparsely IR with results ranging from 3 Gy to 30 Gy (Bekker-Jensen *et al.* 2006; Kruhlak *et al.* 2006; Haince *et al.* 2008; Hong *et al.* 2008).

Motivated by these extreme differences in estimates of the laser dose equivalent (LDE), we revisited the idea of a previously established biological dosimetry in which the numbers of X-ray- and laser-induced RPA foci were compared to define an X-ray equivalent laser dose (Bekker-Jensen *et al.* 2006). By using the same cell line (U2OS), the repair-related protein (RPA) and LMI system (pulsed nitrogen laser;  $\lambda = 337\text{nm}$ ), we ensured comparability with previous results (Bekker-Jensen *et al.* 2006). Beside X-rays, we used heavy charged particles as an ionizing reference radiation. In order to account for the non-homogeneous dose distribution of LMI and charged particles, the volume in which the RPA foci were counted was restricted to the irradiated part of the nucleus. Because the resulting dose-response curve for charged particle-induced RPA foci saturated, which even high-resolution 4Pi microscopy could not resolve, the local LDE could not be accurately determined. However, the locally applied LDE can be estimated to be comparable to or even higher than the dose delivered by very densely ionizing charged particles. Recruitment studies of the telomere repeat-binding factors TRF1 and TRF2 both showed local accumulation after LMI as reported previously for TRF2 (Williams *et al.* 2007; Bradshaw *et al.* 2005). However, no significant recruitment of TRF1 and TRF2 was observed after low energy xenon ion irradiation. These results support the assumption of an even higher LDE than previously estimated, although additional and not well-characterized differences between laser- and IR-induced DNA damage spectra cannot be ruled out.

## 6.2 Material and methods

### 6.2.1 Cell culture

Confluent normal human foreskin fibroblasts (AG1522; Coriell cell repository, Camden, NJ; passage 13 to 16), human osteosarcoma cells (U2OS; ATCC, Middlesex, UK) and human dermal fibroblasts (1BR3) stably expressing YFP-TRF1 or YFP-TRF2 were used. Cells were grown at 37 °C, 100% humidity and 5% CO<sub>2</sub> in EMEM, DMEM or Alpha-MEM, respectively (all Biochrome, Berlin, Germany). The media were supplemented with EBSS, 1% glutamine, 0.5% penicillin/streptomycin and 15% fetal calf serum (FCS), with 4.5 g/l glucose Na-pyruvate and 10% FCS or with 1% glutamine and 10% FCS, respectively. Cell lines were regularly checked to be mycoplasma free.

Directly before UVA-LMI, the cell samples were mounted in a Focht chamber system FCS2 (Bioprotechs Inc, Butler, PA, USA) filled with conditioned medium. For the laser experiments U2OS, cells were pre-sensitized towards UVA light by incubation with 10 µM BrdU for 24h (Limoli & Ward 1993; Bekker-Jensen *et al.* 2006). Pre-sensitization was omitted for 1BR3 cells.

### 6.2.2 Production of cells stably expressing YFP-TRF1 and -TRF2

Full-length human TRF1 or TRF2 cDNA was cloned in-frame in a FLAG-tag and YFP-containing plasmid construct derived from the retroviral vector pQCXIP (BD Biosciences, Franklin Lakes, NJ, USA). All constructs were verified by sequencing. Packaged YFP-TRF1 or YFP-TRF2 viruses were used to transfect the human fibroblast cell line 1BR3 to generate puromycin-resistant cells stably expressing YFP-TRF1 and YFP-TRF2.

### 6.2.3 Irradiation and dose calculation

For UVA laser irradiation, the Leica Microdissection System LMD AS was used. The upright Leica microscope is equipped with a pulsed (5 ns; 30 Hz) Nitrogen Laser (337nm). Measurements of the laser power were performed prior to irradiation with a UVA-sensitive photometer Orion/PD (Ophir Optotronics, Rohrsen, Germany) simulating the irradiation situation of a sample mounted in the FCS2. Irradiation was performed with a HCX PL Fluotar L 63x/0.70 Corr PH 2 objective focusing the laser beam spot to a diameter of ~2 µm. With the used laser setting a laser irradiance of 1.5 µW was applied corresponding to a radiant exposure of 0.3 MJ/m<sup>2</sup>. For UVA-LMI of 1BR3 cells, the laser irradiance was increased to 4.4 µW but the exposure time was reduced to keep the laser exposure constant. Multiple setting of targeting marks within the field of view allowed the almost simultaneous irradiation of several nuclei. The irradiation of multiple fields took up to half an hour.

The charged particle irradiation was done at the UNILAC facility at the GSI Helmholtzzentrum für Schwerionenforschung as described previously (Jakob *et al.* 2003; Jakob *et al.* 2005). The ions used, their specific energies and LETs are listed in Table VI-I. The deposited energy for each ion species was calculated as the product of a constant LET and the summed length of all traversals per nucleus. The total traversal length was further standardized to the average value of all analyzed nuclei (18 µm) to allow for a direct

comparison between ion species. The dose deposited per nucleus was calculated as the ratio of the deposited energy and the assumed average mass of a nucleus (855 ng, Fig. 6-1).

Irradiation with X-rays was performed in a 250 keV X-ray tube (Isovolt DS1, Seiffert, Germany) at a dose rate of 3 Gy/min.

**Table VI-I.** Calculated charged particle doses absorbed per nucleus

Ion species	Mean energy on target	LET	Dose per nucleus after standardization
	MeV/n	keV/ $\mu\text{m}$	Gy
Carbon	5.3	265	0.9
Nitrogen	5.1	363	1.2
Nickel	4.9	3530	11.9
Xenon	2.4	8679	29.2
Uranium	1.9	13438	45.3

$$D = E / m = (0.16 * \text{LET} * 18 \mu\text{m}) / (\rho_{\text{water}} * 855 \mu\text{m}^3)$$

#### 6.2.4 Immunofluorescence Assay

For the immunocytochemical staining experiments cells were fixed in 2% formaldehyde and permeabilized as described previously (Jakob *et al.* 2002). Solely before Mre11 staining the soluble protein fraction was pre-extracted (Jakob *et al.* 2003). Mouse monoclonal anti-RPA (p34) (Lab Vision, Wedel, Germany) and the secondary antibody 488 goat anti-mouse F(ab)2 conjugate (Invitrogen, Karlsruhe, Germany) were used at a dilution of 1:200 in 0.2% BSA in PBS and 1:400, respectively. For 4Pi microscopy the RPA antibody was combined with rabbit polyclonal anti-53BP1 (Ab-1; 1:500; Oncogene, VWR, Darmstadt, Germany) antibody, as indicated. Also for 4Pi microscopy, the anti-MRE11B rabbit polyclonal antibody (1:300; Novus-Biologicals, Abcam, Cambridge, UK) was used together with mouse monoclonal anti-phospho-(Ser139)-H2AX primary antibody (1:500; clone JBW301; Upstate Biotechnology, Hamburg, Germany) at the indicated dilutions. Secondary antibodies used were 5  $\mu\text{g}/\text{ml}$  of Atto 647N goat anti-mouse-IgG (Sigma-Aldrich Corporation, St. Louis, MO, USA) and Alexa 568 goat anti-rabbit IgG conjugate (Invitrogen, Karlsruhe, Germany). Cells were counterstained with 1  $\mu\text{M}$  ToPro3 (Invitrogen, Karlsruhe, Germany).

#### 6.2.5 Microscopy

Microscopic imaging was done on a Leica TCS confocal system equipped with a DM IRBE inverted microscope (lens: HCX PlanApo 63x/1.32) and an argon-krypton laser. From each sample, images containing in total 13 to 23 nuclei were taken as sets of 11 to 14 optical sections. The optical sections were recorded in increments of  $\sim 0.25 \mu\text{m}$  across the thickness of nuclei which was usually  $\sim 3 \mu\text{m}$ .

4Pi Microscopy was performed with a custom made 4Pi setup at the DKFZ (German Cancer Research Centre) in Heidelberg. The setup was based on a Leica confocal laser scanner TCS-SP2 equipped with two opposing HCX PL APO CS 100x/1.46 Oil (Leica



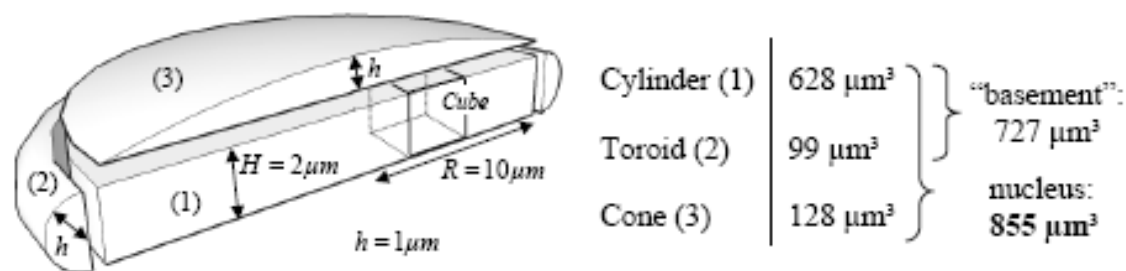


**Figure 6-1.** Illustration of the Cube and the geometrical assumptions underlying the scaling factors. The Cube is shown within a simplified geometrical model of a nucleus. Given dimensions were estimated based on the measurements of an average thickness ( $3 \mu\text{m}$ ) and area ( $320 \mu\text{m}^2$ ) of the analyzed nuclei. The volumes of the basement, the nucleus, the Cube and the CountCub allow for a calculation of the scaling factor for X-rays (85%; basement/nucleus) and LMI-induced foci numbers (67%; Cube/CountCub).

Microsystems, Mannheim, Germany) (Lang *et al.* 2007). The dyes Alexa568 and ATTO647 in the samples were excited with HeNe-Lasers at 543 nm and 633 nm, respectively. The resolution in xy was 170nm and axially 100nm. For imaging, the samples were mounted in 97% 2,2-thiodiethanol according to the procedure described in Staudt *et al.* (2007).

### 6.2.6 Quantitative image analysis

RPA foci were counted in average projections of acquired confocal stacks of X-ray-irradiated nuclei (up to 28 nuclei per dose), UVA laser-irradiated nuclei sensitized with BrdU ( $n = 53$ ) and charged particle-irradiated nuclei (up to 25 nuclei per ion species). The analysis program was developed in collaboration with the Department of Image Processing (R. Schäfer, D. Schubert, K.Sandau) at the University of Applied Science, Darmstadt (Germany) and programmed in IDL (V6.0; Research Systems Inc.). The software has been described elsewhere (Jakob *et al.* 2009a). Briefly, after segmentation of nuclei and extraction of signals above background, foci were detected using adaptive bimodal thresholds and fitted by 2D intensity projections of spheres with increasing radii.

The actually irradiated area was defined manually in each image and afterwards subdivided into areas of  $2 \times 2 \mu\text{m}$ . As the foci counting was performed in stack projections the area corresponds to a volume of  $2 \times 2 \times 3 \mu\text{m}$  considering an average nuclear height of  $3 \mu\text{m}$ . Thus, the measured foci number was related to this volume named counting cuboid (CountCub). Foci numbers related to the cubic volume (Cube;  $2 \times 2 \times 2 \mu\text{m}$ ) were then calculated based on the data obtained in CountCubs and introducing a scaling factor. Assuming a random distribution of RPA foci in depth after X-ray and laser irradiation the respective scaling factors for both radiation types depend only on geometrical assumptions illustrated by a simplified model of a nucleus (Fig. 6-1). For laser irradiation, the irradiated volume is mostly located in the center of the nucleus where the thickness is given by the average value of  $3 \mu\text{m}$ . Thus, the scaling factor for the number of laser-induced RPA foci per Cube is the ratio of the heights of the Cube and the nucleus that is  $2\mu\text{m}/3\mu\text{m}$  (67%). This is different for X-ray-induced foci being randomly distributed all over the nucleus. Here, the

volume ratio of the nuclear 'basement' (Fig. 6-1) and the whole nucleus has to be calculated yielding a scaling factor of 85%. For charged particle irradiation no scaling is needed as the Cube contains the same number of foci as the CountCub.

## 6.3 Results

### 6.3.1 The volume used for foci counting affects the estimation of localized doses

For an estimation of the absorbed X-ray equivalent dose in UVA laser experiments, we modified a previously used method of biological dosimetry (Bekker-Jensen *et al.* 2006). This method was based on the comparison of RPA foci numbers induced by UVA laser irradiation and different X-ray doses. According to the original assay (Bekker-Jensen *et al.* 2006), U2OS osteosarcoma cells were sensitized to UVA light by incorporation of BrdU for 24 h before irradiation and fixed 1 h post-irradiation. Irradiation-induced RPA foci were automatically counted in projections of the obtained confocal image stacks. The amount of RPA foci induced by the UVA laser system (337 nm Nitrogen laser) was comparable to that observed after an X-ray dose of 2 to 3 Gy (Fig. 6-2), consequently defined as the X-ray equivalent laser dose. This result is in agreement with the previously reported X-ray equivalent laser dose of 3 Gy using this type of approach (Bekker-Jensen *et al.* 2006). Therefore, the laser exposure of 0.3 MJ/m<sup>2</sup> used in this experiment was chosen as a standard setting for all subsequent UVA laser irradiations.

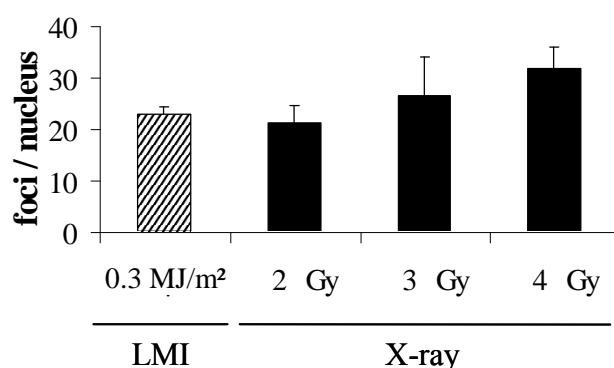


**Figure 6-2.** Amount of RPA foci per nucleus induced by UVA laser and X-ray irradiation. U2OS osteosarcoma cells were irradiated with a UVA laser and different doses of X-rays. The average amounts of RPA foci per nucleus recognized by the analyzing program and after subtraction of the level in mock-irradiated cells ( $3.5 \pm 0.3$  RPA foci;  $n = 95$ ) are depicted. Average values induced by a laser exposure of 0.3 MJ/m<sup>2</sup> are comparable to the RPA foci induction after 2 to 3 Gy of X-rays. Error bars indicate the standard error of the mean (SEM).

While the number of RPA foci per nucleus was similar after laser and X-ray irradiation, we observed clear differences in terms of signal intensity and spatial distribution of the respective foci. Laser-induced foci typically appeared brighter and denser compared to the broadly distributed and less intense RPA foci after X-ray irradiation (Fig. 6-3), giving the impression that UVA-LMI induced much more severe DNA damage than 3 Gy of X-rays. Therefore, we studied the suitability of the used dosimetry approach to reproduce higher and locally applied doses. For this purpose, we used accelerated charged particles that allow local deposition of a broad range of well-defined doses. To facilitate counting of charged particle-induced RPA foci along the ion trajectory, the irradiation was delivered at low angle (15°) between the cell layer and the beam direction as described earlier (Jakob *et al.* 2003). Using this irradiation geometry, a track of clearly distinguishable foci (Fig. 6-4; inset) could be assigned to a single

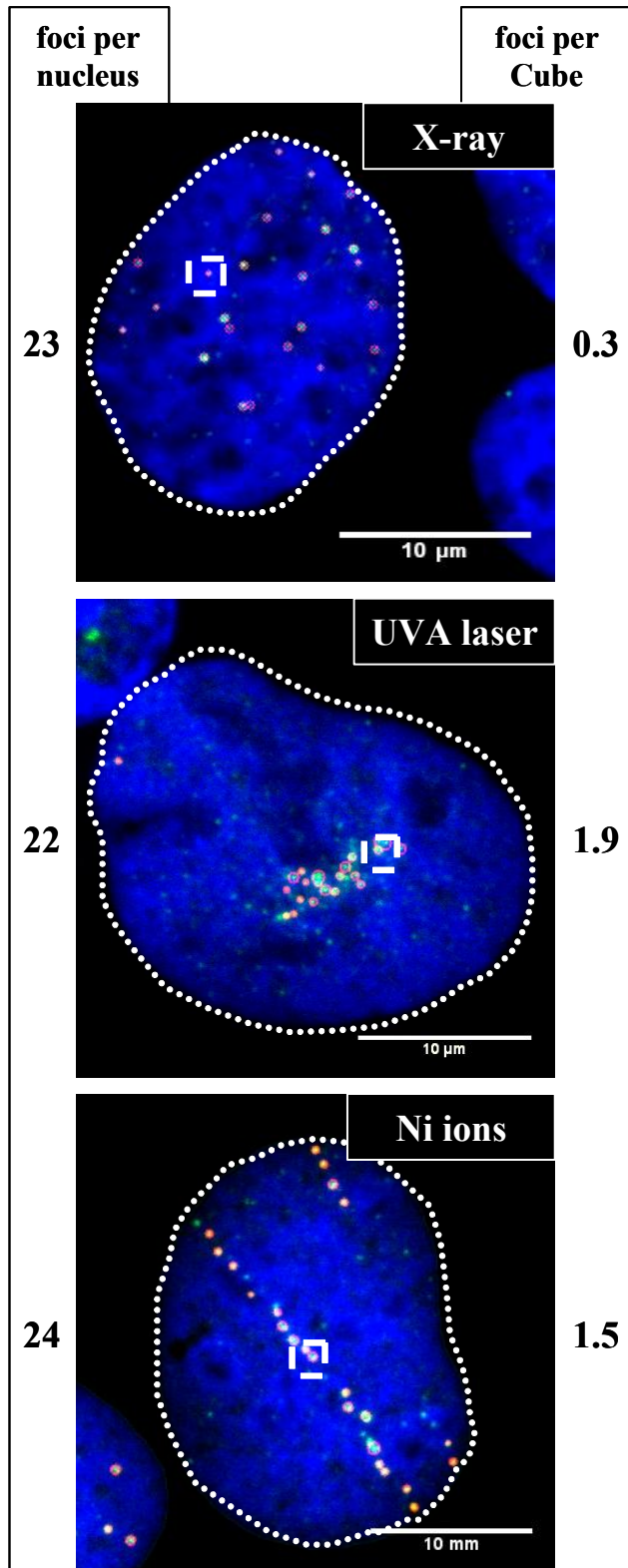


**Figure 6-3.** The fraction of the irradiated nuclear volume depends on the irradiation type. The depicted cell nuclei were irradiated with 2Gy of X-rays (top), UVA laser (center; 0.3 MJ/m<sup>2</sup>) and nickel ions (bottom). The RPA foci (green) that were recognized by the IDL program are marked with red circles. The number of foci within the nuclei (dotted line) was 23, 22 and 24, respectively. When applying the newly defined Cube of 2 x 2 x 2  $\mu$ m (indicated as dashed box in the depicted 2D average projection), the average numbers of counted foci per Cube are altered. The resulting average values for the respective irradiation types are indicated to the right of each depicted nucleus. Average projections of the original image stacks are shown. The DNA is counterstained with ToPro3 (blue).

ion traversal. The number of foci can be assumed to be linearly correlated to the length of the ion traversals (Jakob *et al.* 2009a). Thus, the nuclear dose was calculated based on the LET (defined as the deposited energy per track length) and the total length of all traversals in a nucleus. This assures a linear correlation between calculated nuclear particle dose and the number of foci induced by this dose. As the total traversal length varied from nucleus to nucleus, the total length of all traversals in a nucleus was standardized to the average value for

all analyzed nuclei (18  $\mu\text{m}$ ). As a result of the standardization, the calculated nuclear particle doses depend only on the respective LET (Tab. VI-I; dose formula) and range from 0.9 Gy (carbon ions) to 45.3 Gy (uranium ions). The resulting mean numbers of RPA foci induced per 18- $\mu\text{m}$  track length are depicted in Figure 6-4 for several ion species in comparison to the X-ray data. While the X-ray data were generally obtained in U2OS cells, for charged particle irradiation also normal human fibroblasts were used. However, neither cell line showed a significant difference in RPA foci induction as representatively shown for carbon ion irradiation (Fig. 6-4; first two columns). According to the counted RPA foci, the X-ray equivalent doses for the used ion species were well below 3 Gy. The actually deposited, standardized charged particle doses per nucleus (Tab. VI-I) are also depicted in Figure 6-3. For carbon and nitrogen ions, they were in the range of the X-ray equivalent doses estimated from RPA foci induction. However, for charged particles with higher LET and, therefore, higher lesion density, the deposited nuclear doses (nickel: 11.9 Gy, xenon: 29.2 Gy, uranium: 45.3 Gy) and the given X-ray equivalent dose (2 Gy) diverged dramatically. Clearly, the used method of biological dosimetry is not able to reproduce nuclear doses of high-LET charged particles but underestimates their dose deposition by a factor of 15 in the case of xenon ion irradiation.

One reason for the failure of this assay to reproduce high nuclear doses of charged particle irradiation can be assigned to the different spatial dose distribution of X-rays and charged particles. In contrast to X-rays, particles do not deposit their energy homogeneously but localize along the particle trajectory and hence in a small subvolume of the nucleus (Scholz *et al.* 1997; Jakob *et al.* 2003). However, in the hitherto applied assay, the RPA foci were counted throughout the whole nucleus.

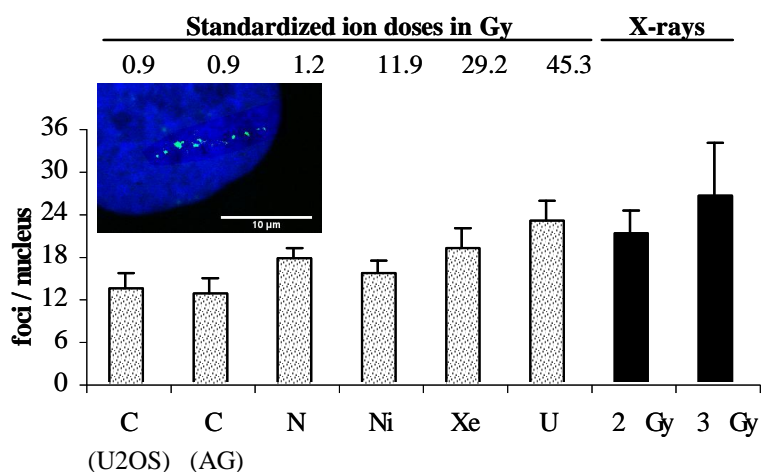


**Figure 6-4.** Amount of RPA foci per nucleus induced by charged particle and X-ray irradiation. The amount of RPA foci per nucleus induced by different ion species compared to the X-ray data from Fig. 1 allocates the nuclear charged particle doses at  $\sim 2$  Gy of X-rays or lower. The indicated calculated nuclear particle doses and the corresponding foci numbers per nucleus are standardized to a total length of all traversals per nucleus of 18  $\mu\text{m}$ . Error bars indicate the SEM. Inlay: U2OS cell nucleus irradiated with carbon ions under a low angle. The nucleus was hit by a single carbon ion as visualized by immunocytochemical staining of RPA (green). The RPA foci form typical streaks. The DNA is counterstained with ToPro3 (blue).

### 6.3.2 Estimation of a local laser dose equivalent by foci counting in reduced subnuclear volumes

In order to accommodate for the localized dose deposition of charged particles, we reduced the volume in which the RPA foci were counted. The dimensions of the newly defined cubic volume (Cube;  $2 \times 2 \times 2 \mu\text{m}$ ) were chosen considering the track structure of charged particles and the range of induced  $\delta$ -electrons (Krämer & Kraft 1994; Scholz *et al.* 1997). Figure 6-2 is a representative example illustrating the impact of the volume in which the X-ray-, UVA laser- and charged particle-induced RPA foci are counted. Within the depicted nuclei, similar foci numbers (23, 22 and 24 foci) were counted after different types of irradiation; X-rays, UVA laser and nickel ions, respectively. Accordingly, X-ray equivalent doses of 2 Gy would be defined for the laser and nickel ion irradiations, even though the nickel irradiation applies an actual nuclear dose of 20.7 Gy at the given total track length of  $31 \mu\text{m}$  within the depicted nucleus (Fig. 6-3; lower panel). In contrast, the foci numbers counted within the Cube were 0.3 (X-ray), 1.9 (laser) and 1.5 (nickel) foci per Cube for these particular nuclei, showing that the local LDE could be even higher than for nickel ion irradiation. Note that foci quantification is typically done in average projections comprising the whole nucleus in depth (here up to  $3 \mu\text{m}$ ). The resulting foci numbers were subsequently scaled according to the  $2 \mu\text{m}$  depth of the Cube (for details see Materials and methods section).

The mean numbers of RPA foci counted per Cube are depicted in Figure 6-5 for different X-ray and local charged particle doses. The particle doses absorbed within the Cube were calculated based on the dose definition formula (Tab. VI-II). The absorbed energy is the product

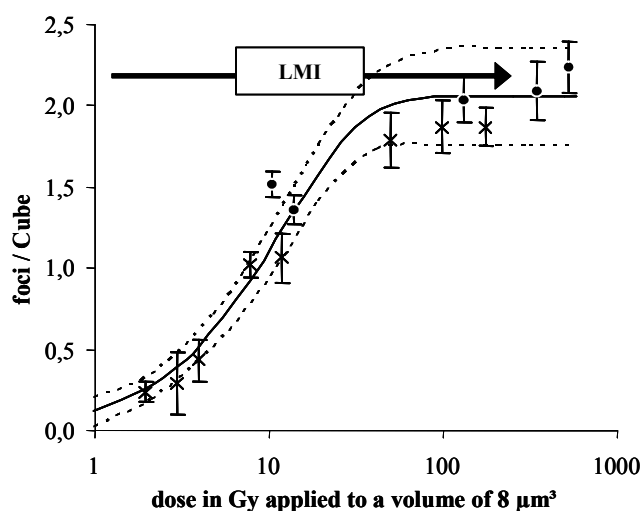


**Figure 6-5.** Dose-response curve for irradiation-induced RPA foci using a cubic volume ( $8 \mu\text{m}^3$ ) for foci quantification. Resulting dose-response curve over a logarithmical x-axis after application of the Cube volume. The monoexponential curve (solid line) is fitted in the charged particle and X-ray data points ( $R^2 = 0.96$ ). The allocation of the laser data points to the fit curve is indicated for a laser exposure of  $0.3 \text{ MJ/m}^2$  ( $2.2 \pm 0.2$  foci per Cube; arrow). Error bars indicate the standard error of the mean, whereas the dotted lines represent the 95% confidence interval of the fit curve.

Ion species	LET	Absorbed energy	Absorbed dose
	keV/ $\mu\text{m}$	$10^{-15} \text{ J}$	Gy
Carbon	265	85	10.7
Nitrogen	363	116	14.0
Nickel	3530	1073	134.1
Xenon	8679	2781	347.7
Uranium	13438	4306	583.2

$D = E / m$

of LET and the edge length of the Cube ( $2 \mu\text{m}$ ) and the mass ( $8 \text{ ng}$ ) is given by the respective volume and the density of water. A combined dose-response curve was fitted into the charged particle and X-ray data points. The monoexponential curve levels off at  $\sim 2.0$  foci per Cube with a 95% confidence interval of  $\pm 0.3$ . The fact that foci numbers above the fitted saturation level could still be counted indicates that the observed saturation is not due to a limited optical resolution of RPA foci. The mean RPA foci number induced by laser irradiation was  $2.2 \pm 0.2$  foci per Cube (Fig. 6-5; arrow) showing no significant difference to the fitted saturation level. Thus, the damage potential of laser irradiation seems to be in the range of high-LET charged particles corresponding to a locally applied dose of hundreds of Gray, confirming our hypothesis of a more severe damage induction after UVA-LMI than after a few Gray of X-rays. Unfortunately, the saturation behavior of the curve does not allow for an accurate definition of local LDEs.

### 6.3.3 High resolution 4Pi microscopy of RPA foci does not circumvent limitations in the laser dose estimation

Because charged particle irradiation produced far fewer RPA foci compared with the expected number of induced DSBs (Jakob *et al.* 2009a), we set out to explore if the limited resolution of the confocal microscope could account for the saturation of the RPA foci dose-effect curve. We attempted to resolve better the single lesions within the individual RPA foci by utilizing high-resolution 4Pi microscopy. Resolving possible substructures would increase the RPA foci number and thus, the dynamic range of the charged particle-induced foci dose-response, potentially allowing a more accurate local LDE definition.

The used 4Pi microscope setup provides a lateral resolution of  $170 \text{ nm}$  and an axial resolution of  $100 \text{ nm}$  by applying constructive interference illumination produced by two opposing high aperture

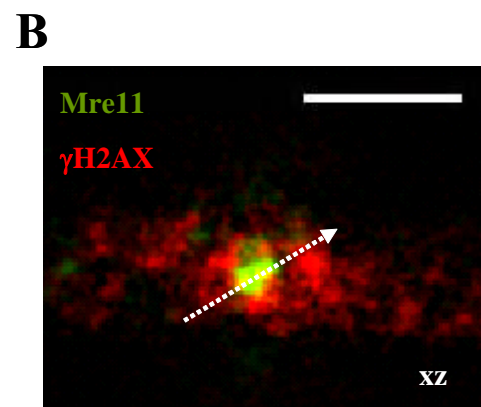
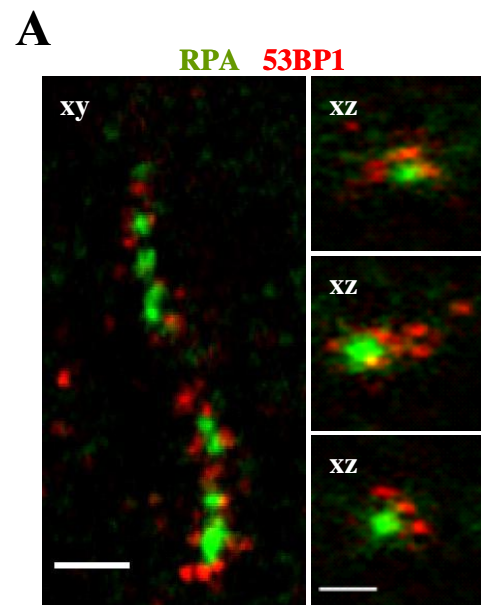


**Figure 6-6.** High-resolution 4Pi microscopy of a charged particle-induced RPA streak. (A) The high-resolution image of a xenon ion track shows a streak pattern of charged particle-induced RPA (green) and 53BP1 foci (red). Three RPA foci from the depicted streak are also given in the xz perspective showing no further substructure (resolution:  $170 \times 170 \times 100 \text{ nm}$ ). All three RPA foci are surrounded by several smaller 53BP1 foci, but both proteins do not co-localize. (B) A similar behavior is observed for Mre11 foci (green) and  $\gamma\text{H2AX}$  (red). The depicted Mre11 focus is surrounded by an intense  $\gamma\text{H2AX}$  signal that is reduced within the Mre11 focus (see profile). Scale bars:  $2 \mu\text{m}$ .

lenses. Thus, the axial resolution is ~5-fold higher than in conventional confocal systems. However, even with the improved resolution of 170 x 170 x 100 nm, a substructure of the RPA foci could not be observed (Fig. 6-6A). Therefore, more detailed imaging did not allow further specification of a local LDE, although the size of the RPA foci was far larger than this resolution limit.

However, high-resolution microscopy revealed a ~400 nm-sized substructure within individual 53BP1 foci, thus demonstrating the capability of the used system to resolve even smaller structures than the observed RPA foci. Interestingly, several of the resolved multiple 53BP1 spots surrounded a single RPA focus without co-localizing (Fig. 6-6A). Comparable behavior regarding the substructure and the lack of co-localization was observed using 4Pi microscopy for the DSB markers Mre11 after pre-extraction and the DSB-flanking H2AX phosphorylation at this high resolution (Fig. 6-6B).

#### 6.3.4 Recruitment of TRF1 and TRF2 after LMI but not after charged particle irradiation

Further support for a high local LDE came from the observation of the recruitment of telomere repeat-binding factors TRF1 and TRF2. These proteins are known for their interaction with telomeric regions and with repair-related proteins (reviewed by de Boeck *et al.* 2008). Recently, the DNA damage-induced phosphorylation of TRF2 (Tanaka *et al.* 2005) as well as its recruitment to laser-damaged sites were demonstrated in sensitized (Bradshaw *et al.* 2005; Williams *et al.* 2007) and non-sensitized cells (Williams *et al.* 2007). However, TRF2 recruitment to damage sites was not observed following IR exposures such as 5 Gy  $\gamma$ -rays or  $\alpha$ -particles. Even localized irradiation with multiple helium ions at the Columbia University microbeam facility (RARAF) failed to accumulate TRF2 (Williams *et al.* 2007). Here, using high LET (8679 keV/ $\mu$ m) xenon ions, no detectable amounts of TRF1 or TRF2 were recruited to the sites of ion traversals (Fig. 6-7B) in human fibroblasts (1BR3) stably expressing YFP-tagged TRF1 or TRF2, respectively. Note that a single xenon ion deposits a local dose of ~350 Gy (Tab. VI-II) to the Cube (8  $\mu$ m<sup>3</sup>) corresponding to an estimated induction of ~120 DSBs (Prise *et al.* 1998).

Although the high number of DSBs following charged particle irradiation was insufficient to induce TRF1 or TRF2 recruitment, both proteins were readily recruited to laser-irradiated sites within seconds as reported previously for TRF2 (Bradshaw *et al.* 2005; Williams *et al.* 2007) and shown here for TRF1 after UVA laser irradiation of non-sensitized cells (Fig. 6-7A) This might indicate an even higher amount of induced DSBs. For this experiment, the standard laser power (1.5  $\mu$ W) was increased 3-fold to compensate for the expected reduced damage induction in non-sensitized cells according to Williams *et al.* (2007), who monitored the recruitment of TRF2 in sensitized and non-sensitized cells using 800 nm two-photon LMI.



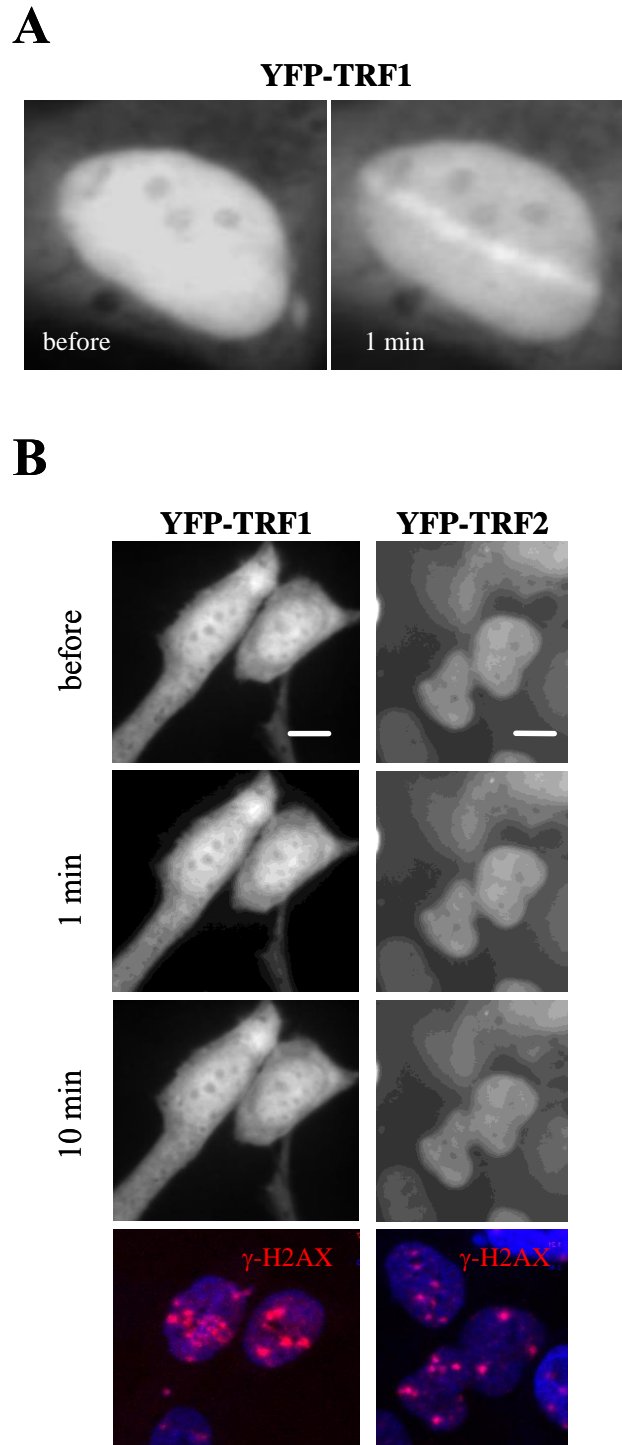


**Figure 6-7.** TRF1 and TRF2 recruitment after LMI but not charged particle irradiation. 1BR3 cells stably expressing YFP-tagged TRF1 or TRF2. (A) LMI induces the fast recruitment of YFP-TRF1. The irradiated nucleus is shown directly before and 1 min after the irradiation. (B) The same cell line irradiated with xenon ions does not show TRF1 recruitment within 10 min after irradiation (left panel). Hitting of the depicted nuclei was confirmed by subsequent immunostaining against  $\gamma$ H2AX (red; lower panel). Similar results were obtained with YFP-tagged TRF2 also stably expressed in 1BR3 cells (right panel). Scale bar: 10  $\mu$ m.

## 6.4 Discussion

The aim of this study was to compare the damage induction after UVA-LMI and IR in order to estimate the IR equivalent local laser dose deposited by a UVA-LMI system. We first used a commonly applied assay described by Bekker-Jensen *et al.* (2006) based on counting radiation-induced RPA foci. The nuclear LDE deposited in an irradiated mammalian nucleus by a 337 nm laser with a radiant exposure of 0.3 MJ/m<sup>2</sup> and prior incorporation of BrdU was found to be equivalent to 2-3 Gy (Fig. 6-1). This is in agreement with previously reported nuclear LDE values of 3 Gy comparing RPA foci numbers (Bekker-Jensen *et al.* 2006)], 6 – 9 Gy comparing  $\gamma$ H2AX foci numbers (Haince *et al.* 2008) or 5.25 Gy comparing  $\gamma$ H2AX signal intensities (Kruhlak *et al.* 2006).

Nevertheless, we felt these low nuclear LDE values might be misleading as the possible impact of the different spatial dose deposition of LMI and the used sparsely ionizing reference radiation was not taken into account. For example, high locally applied charged particle doses have been shown to produce more efficient DNA fragmentation compared to X-rays (Löbrich *et al.* 1996). Accordingly, an immunofluorescent comet assay monitoring fragment size distributions yielded a higher nuclear LDE of 20 Gy (Grigaravicius *et al.* 2009).

Since previous estimated nuclear LDEs based on radiation-induced foci formation were obtained disregarding the spatial dose distribution, we set up to test the validity of the RPA foci assay for well-known locally applied doses. For this purpose, we used densely ionizing charged particle irradiation allowing localized energy deposition similar to LMI and estimated its X-ray equivalent dose according to the previously described assay (Bekker-Jensen *et al.* 2006). Interestingly, despite depositing particle doses of up to 45 Gy per nucleus (Tab. VI-I), the assay yielded X-ray equivalent charged particle doses of only ~2 Gy (Fig. 6-4). Clearly, the difference of the irradiated volumes leads to a discrepancy between estimated and actually applied doses in the case of local irradiation. The assay used is based on the counting of radiation-induced RPA foci within the whole nucleus, but low energy charged particles deposit their energies only within a small confined sub-volume (Scholz *et al.* 1997; Jakob *et al.* 2003). Consequently, nuclear particle doses are systematically underestimated using this approach. Since energy is also locally applied in the case of LMI, the LDE will also be underestimated. To account for the differences in the irradiated nuclear volumes after X-rays, charged particles and LMI, we reduced the volume for foci quantification and defined a cubic volume of 2 x 2 x 2  $\mu$ m (Cube) to compensate for the radial symmetrical dose deposition of charged particles. The numbers of foci per Cube were quantified based on foci counting in average projections as commonly done. Since projections encompass the whole nucleus in depth (up to 3  $\mu$ m) but the Cube's height is only 2  $\mu$ m, scaling factors were introduced as described in detail in the Material and methods section.

Following the application of the Cube, the charged particle-induced RPA foci dose-response curve reached a plateau for the high locally applied doses of xenon and uranium ions (Fig. 6-5). Since the RPA foci induction after UVA-LMI was located in this saturation region the local LDE could only be estimated to be roughly in the range of a few hundred Gray. This estimation is in agreement with calculated laser doses based on standard absorption rates (Paull *et al.* 2000). In contrast, previous attempts of a local laser dose estimation using sparsely IR as the only reference, but applying volumes for foci counting 7-fold larger than the Cube, yielded lower values of 10 Gy (Bekker-Jensen *et al.* 2006) or 30 Gy (Hong *et al.*

2008). However, in these studies, the defined volumes for foci counting were designed to encompass the whole laser streak, thereby comprising significant proportions of unirradiated volume. The obtained local LDE values were, therefore, comparably low. In the present study, the used UVA-LMI could be attributed to dose values exceeding 100 Gy, but the accuracy of the estimation is still limited by the observed saturation of the RPA foci numbers with increasing dose deposition. As for single measurements, foci numbers often exceeded the mean values given here; a detection limit of the used image software can be excluded. Thus, the saturation is most probably based on biological effects. A possible depletion of the RPA protein, a key mechanism in the replication/repair switch (Wang *et al.* 1999), may only explain the observed saturation of the X-ray dose-response curve, as the total number of induced RPA foci is much higher than after charged particle irradiation and UVA-LMI. We investigated further whether the observed plateau in the number of charged particle-induced RPA foci was a result of the resolution limit of the confocal microscope that might be insufficient to resolve single lesions within RPA foci. In order to circumvent the limiting resolution of the confocal microscope, perhaps masking additional RPA foci, we performed high-resolution 4Pi microscopy aiming to reveal the substructure of individual foci. Although the RPA foci induced after xenon ion irradiation were generally larger than the resolution limit of the 4Pi microscope (170 nm lateral, 100 nm axial), a substructure could not be resolved (Fig. 6-6A). Hence, even high-resolution microscopy was not able to improve the estimation of the locally applied LDE.

While RPA foci could not be resolved further by 4Pi microscopy, interestingly, the damage marker 53BP1 showed a substructure of multiple smaller domains surrounding the RPA focus but remarkably without co-localizing. As 53BP1 specifically binds to a histone modification (Huyen *et al.* 2004) and RPA binds to ssDNA (Kim *et al.* 1992) most probably unwound from nucleosomes, this might explain the nearby but not overlapping foci. However, even high-resolution microscopy did not reveal separate RPA-marked ssDNA filaments. This observation supports the idea that the RPA foci do not mark the processing of separate individual DNA lesions after densely IR as suggested previously (Jakob *et al.* 2009a). Instead, multiple DNA damages originally induced in near vicinity within a chromatin domain might be processed subsequently at a common place resulting in a central RPA focus surrounded by several smaller 53BP1 stained regions (Fig. 6-6A). The finding that damage-induced histone modifications are flanking but not co-localizing with the actual sites of DSB repair was also observed after Mre11 and  $\gamma$ H2AX staining. 4Pi microscopy revealed that the focus of Mre11 remaining after *in situ* extraction is surrounded by a bright  $\gamma$ H2AX staining, whereas in its center, the  $\gamma$ H2AX signal appears less intense (Fig. 6-6B). Notably, the Mre11 protein involved in DSB end processing has exonuclease/endonuclease activity providing a potential basis for ssDNA formation, a prerequisite to RPA binding. The substructure observed for the phosphorylated form of histone H2AX is in agreement with previously described distribution of H2AX into microdomains using 4Pi microscopy (Bewersdorf *et al.* 2006).

A comparison of the laser exposure used in this study to values in the literature (Tab. VI-III) shows that the chosen setting for the UVA laser system (radiant exposure of 0.3 MJ/m<sup>2</sup>) is comparable with settings of similar UVA laser types. Thus, it can be excluded that the high local LDE found in the present study is a result of an inappropriately high laser power. It also reflects the validity of the presented estimation and applies to other UVA-LMI systems.

**Table VI-III.** Typically used UVA laser exposures<sup>a</sup>

Wavelength in nm	Radiant exposure in MJ/m <sup>2</sup>	References
337	0.1	Ref. in Kong <i>et al.</i> 2009
	<b>0.3</b>	<b>Present study</b>
	0.4	Kong <i>et al.</i> 2009
	0.5	Bekker-Jensen <i>et al.</i> 2006, Vogel <i>et al.</i> 2007, Kong <i>et al.</i> 2009
	1	Tashiro <i>et al.</i> 2000
390	10, 30	Paull <i>et al.</i> 2000

<sup>a</sup> In the case of pre-sensitization by BrdU incorporation.

Further support for a high locally applied LDE arises from the differences in the recruitment of the telomere repeat-binding factors TRF1 and TRF2 after charged particle irradiation and LMI. The TRF2 protein has been shown to accumulate after LMI in both pre-sensitized (Bradshaw *et al.* 2005; Williams *et al.* 2007) and non-sensitized cells (Williams *et al.* 2007), and recently, a function in strand invasion during non-telomeric homologous recombination repair of DSBs was proposed (Mao *et al.* 2007). Remarkably, no recruitment of TRF2 could be shown after IR even after local (20  $\mu\text{m}^2$ ) application of 416 Gy  $\alpha$ -particles using a microprobe setup for targeted irradiation (Williams *et al.* 2007). In our study, we used xenon ion irradiation applying an even more confined local dose of  $\sim 350$  Gy in a volume of 8  $\mu\text{m}^3$ . We also saw no accumulation of TRF1 or TRF2 (Fig. 6-7B) at sites of particle traversals. In contrast, LMI rapidly induced the recruitment of TRF2 (Bradshaw *et al.* 2005; Williams *et al.* 2007) and TRF1 (Fig. 6-7A). Different scenarios can be imagined to explain these contrasting results. The density of DSBs could be higher after two-photon LMI (Williams *et al.* 2007) or UVA-LMI (used here) than with heavy charged particles resulting in a detectable amount of accumulated proteins. This leads to the conclusion that the LDE of our laser system is much higher than 350 Gy under the conditions used (increased laser power and omitted sensitization). Despite the reported influence of sensitization treatments on the yielded damage spectra (Kong *et al.* 2009), we obtained comparable LDE estimations using either sensitization and standard laser settings or omitting sensitization and increasing the laser power. The ability of higher laser power to compensate for a reduced damaging capability has been shown previously for TRF2 recruitment following two-photon LMI (Williams *et al.* 2007).

Alternatively, possible differences in the induced damage spectra could also be a reason for the differential recruitment after LMI and charged particle irradiation, as discussed by Williams *et al.* (2007). According to the authors, the additional induction of UV-related damages after LMI might be responsible for the recruitment of TRF2. Regardless of the damage type, UVA- and two-photon LMI clearly generate conditions that permit TRF1 and TRF2 recruitment to laser-induced DNA damage sites. In this particular context, it is interesting that the mechanism of DSB induction classically described for UVA bulb irradiation does not explain the proposed high amount of DSBs induced by LMI (Peak & Peak

1990). Therefore, further damage induction related to non-linear absorption effects needs to be considered (Vogel *et al.* 2007; Kong *et al.* 2009). This might also be an explanation for the recruitment of TRF1 (see Fig. 6-7A) and TRF2 (Williams *et al.* 2007) showing that sensitization is not mandatory for damage induction if the laser power is increased. The occurrence of damage induced by non-linear laser absorption would make a direct comparison of repair data obtained after LMI and ionizing irradiation even more difficult.

In summary, in the present study, by considering the locally applied dose deposition, we estimated the local UVA-LDE to be in the range of a few hundred Gray. Due to the saturation of the foci dose-response curve, a more accurate specification of the local LDE could not be achieved, despite the application of very sophisticated techniques such as low angle ion irradiation and 4Pi microscopy. However, 4Pi microscopy does facilitate visualization of changes in the substructure of DSB markers like  $\gamma$ H2AX or 53BP1, which might allow further characterization of high local doses. Clearly, a more detailed knowledge of the laser-induced damage spectrum and the mechanism of damage generation is needed. Nevertheless, to at least improve understanding of comparability of data from different LMI systems, it would be useful to give information about LMI parameters as the totally applied laser energy, the spot size of the laser beam, the wavelength, pulse duration and the energy per laser pulse, as well as the use or lack of pre-sensitization treatments.



## Chapter Seven

### DNA lesions within heterochromatin induce phosphorylation of histone H2AX and are expelled to euchromatic regions

#### **7.1 Introduction**

DNA double-strand breaks (DSBs) have the potential to induce chromosomal aberrations and carcinogenesis. Their correct repair is crucial for genetic stability and depends on a functional damage signaling. An early step in the response to DSBs is the phosphorylation of the histone variant H2AX, forming  $\gamma$ H2AX, by the kinases ATM (Burma *et al.* 2001) and DNA-PKcs, DNA-dependent protein kinase catalytic subunit (Stiff *et al.* 2004). Using immunocytochemical staining methods  $\gamma$ H2AX can be visualized as distinct ionizing radiation-induced foci (IRIF) (Rogakou *et al.* 1999). Interestingly, despite the expected homogeneous damage induction, no  $\gamma$ H2AX IRIF could be detected in the center of heterochromatin compartments in human cell lines between 15 min and 2 h following irradiation (Cowell *et al.* 2007; Falk *et al.* 2008; Goodarzi *et al.* 2008; Vasireddy *et al.* 2009). Similar findings were found in murine embryonic fibroblasts (MEFs) in which  $\gamma$ H2AX signals were excluded from pericentromeric major satellite repeats, so-called chromocenters (Guenatri *et al.* 2004) after 30 min following  $\gamma$ -irradiation (Goodarzi *et al.* 2008; Noon *et al.* 2010) or neocarzinostatin treatment (Kim *et al.* 2007). To explain these observations, it has been postulated that the accessibility of the responsible kinases to these highly compacted chromatin regions might be hindered (Cowell *et al.* 2007; Goodarzi *et al.* 2009). However, in a recent study dextrans, whose size is comparable to DNA-PKcs and ATM, were shown to access chromocenters (Bancaud *et al.* 2009). Thus, the mechanism underlying the lack of  $\gamma$ H2AX signal in heterochromatic regions is currently unclear. Additionally, damage signals located adjacent to constitutive heterochromatin compartments are retarded in their repair kinetics (Goodarzi *et al.* 2008; Noon *et al.* 2010). Here, we investigate the cellular response to DSBs in and adjacent to heterochromatic regions using heavy ions as a tool to deliver spatially localized DSBs. By this means distinct and easily visualized IRIF are induced along the tracks of the traversing particles (Jakob *et al.* 2003). To produce localized DSBs directly within murine chromocenters targeted single ion irradiation was applied using the GSI microbeam facility. We demonstrate that, in contrast to widely held belief, H2AX is phosphorylated within this highly compacted chromatin regions and that damage sites are subsequently expelled to the chromocenter's periphery.

## 7.2 Material and methods

### 7.2.1 Cell culture

Wild-type and ATM-deficient murine embryonic fibroblasts (MEFs and ATM<sup>-/-</sup> MEFs, respectively) and human cervical carcinoma cells stably expressing GFP-tagged histone H2B (HeLa-H2B-GFP) were seeded on glass coverslips for ion irradiation at low angle. In the case of single ion irradiation MEFs were seeded on mylar foil in microbeam chambers as previously described (Heiss *et al.* 2006). Cells were grown at 37°C, 100% humidity and 5% CO<sub>2</sub> in either DMEM-medium (Biochrome, Berlin, Germany) supplemented with 4.5 g/l glucose with Na-pyruvate (wild-type and ATM<sup>-/-</sup> MEFs) or RPMI (HeLa-H2B-GFP). Both media contained 10% fetal calf serum (FCS) in addition. Cell lines were regularly checked to be free of mycoplasma contamination.

### 7.2.2 Irradiation

Ion irradiation at low angle was done at the UNILAC facility at the GSI Helmholtzzentrum für Schwerionenforschung as described previously (Jakob *et al.* 2003). Ion species used for low angle irradiation and their respective linear energy transfers (LETs): Carbon (200 keV/μm), xenon (high energy; 1350 keV/μm), nickel (3430 keV/μm), ruthenium (7060 keV/μm) and xenon (low energy; 8680 keV/μm). Note that the analysis of bending patterns is not affected by varying the ion species, since the patterns of the visualized ion-induced γH2AX streaks are strikingly similar (Jakob *et al.* 2009a).

For single ion irradiation, cells growing in a microprobe chamber were incubated with 0.1 μM Hoechst 33342 for one hour. Directly before single ion irradiation medium was replaced with 50 μl of DMEM-medium without phenol red supplemented with 1 mM HEPES buffer (Biochrome, Berlin, Germany) as described previously (Heiss *et al.* 2006). Ion species and their respective LETs applied in microprobe experiments: Carbon (290 keV/μm), sulfur (1560 keV/μm) and gold (12,260 keV/μm). Cells were kept sealed in the chamber for 30 min at the most and fixed directly after opening. Details on the irradiation procedure are given in Figure 7-1.

### 7.2.3 Immunofluorescence assay

For the immunocytochemical staining experiments cells were typically fixed in 2% formaldehyde and permeabilized as described previously (Jakob *et al.* 2002). Only for the measurement of repair kinetics and signal bending in ATM<sup>-/-</sup> MEFs, cells were fixed in ice cold methanol for 1 h and then permeabilized by 1 min incubation in ice cold acetone. Cells were blocked in 5% BSA/1% FCS/0.1% Tween20 in PBS overnight. Mouse monoclonal antibodies anti-phospho-(Ser139)-H2AX primary antibody (1:500; clone JBW301; Upstate Biotechnology, Hamburg, Germany), anti-RPA (p34) (1:200; Lab Vision, Wedel, Germany) and anti-ATM Protein Kinase pS1981 (1:200; Rockland, Gilbertsville, PA, USA) were diluted in 0.2% BSA in PBS as indicated. Rabbit polyclonal antibodies anti-XRCC1 (AHP 832; AbD Serotec, Düsseldorf, Germany) and anti-53BP1(Ab-1) (Calbiochem, Darmstadt, Germany) were used at a dilution of 1:500 or 1:400, respectively. Secondary antibodies (goat anti-mouse-FITC (Sigma Aldrich, Munich, Germany), Alexa goat 488 and 568 anti-mouse F(ab)2



conjugate and anti-rabbit IgG conjugates (all Invitrogen, Karlsruhe, Germany)) were used at a dilution of 1:400. For the DNA counterstaining either 1  $\mu\text{M}$  ToPro3 (Invitrogen, Karlsruhe, Germany) or 1  $\mu\text{g/ml}$  DAPI (Carl Roth, Karlsruhe, Germany) was used.

#### 7.2.4 Microscopy and image analysis

Image stacks for analysis following low angle ion or microprobe irradiation were acquired using a Leica TCS confocal system with an inverted DM IRBE (lens: HCX Plan Apo 63x/1.32) or a Nikon Xi epifluorescence microscope (lens: CFI Planapochromat VC 100x/1.4). The obtained image stacks were manually analysed in 3D to define ion-hit chromocenters. For each time point between 85 and 100 ion-hit chromocenters were analyzed. Image acquisition for  $\gamma\text{H2AX}$  repair measurements after low angle carbon ion irradiation was performed using a Zeiss Axiovert 200M epifluorescence microscope (lenses: 63x and 100x Plan-Neofluar). Acquired z-stacks were superimposed using the Huygens essential software (Scientific volume imaging, Netherlands) and chromocenter- and euchromatin-associated  $\gamma\text{H2AX}$  IRIF were enumerated in  $\sim 30$  nuclei for each of the analyzed repair time points.

All stack images typically consist of more than 20 slices with an increment of 0.2 to 0.28  $\mu\text{m}$ . These stacks were deconvolved if recorded with an epifluorescent microscope using Huygens essential.

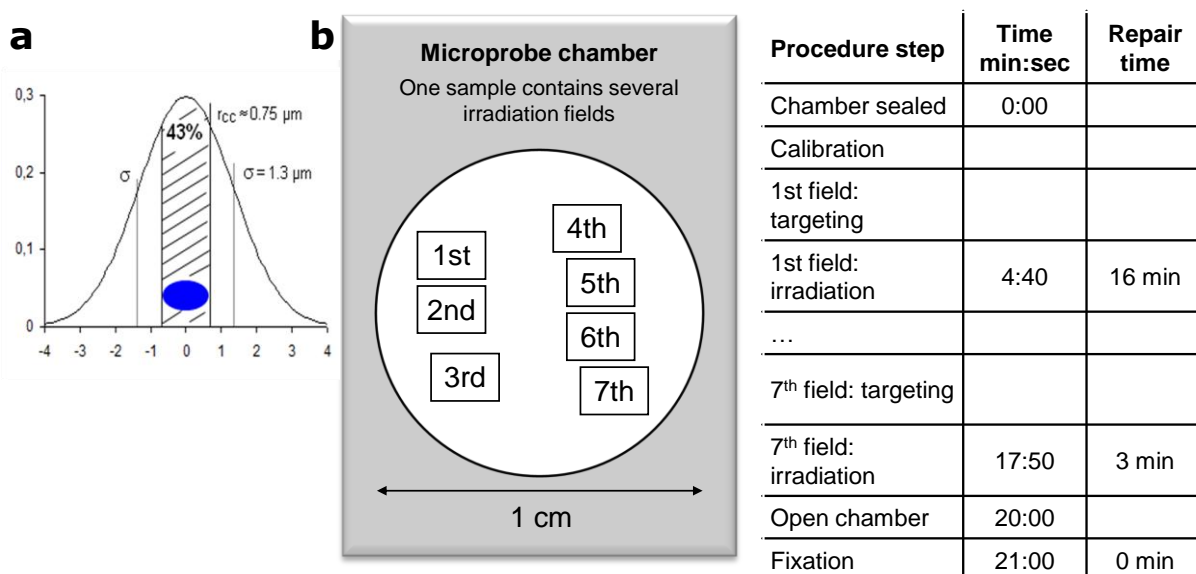


**Fig. 7-1.** (a) Schematic comparison of the microbeam accuracy ( $\sigma = 1.3 \mu\text{m}$ ) illustrated by a gaussian distribution and the typical diameter of a chromocenter ( $r_{\text{CC}} \approx 0.75 \mu\text{m}$ ; blue ellipse). According to these parameters about 43% of targeted chromocenters should exhibit internal signals. Central hits were expected in about 15% of targeted chromocenters ( $r_{\text{central}} \approx 0.5 \mu\text{m}$ ). Both values are in agreement to the here described signal distribution. (b) Targeted single ion irradiation. MEF cells were seeded on mylar foil in a microprobe chamber (left scheme) and 6-7 fields of view were targeted for irradiation. The course of the irradiation procedure is exemplarily shown (table): (i) The chamber was sealed with a glass coverslip after replacing the medium with medium (50  $\mu\text{l}$ ) containing 1mM Hepes buffer and was fit into the microprobe microscope (temperature controlled at 37°C), (ii) the microscope position was calibrated using reference marks on the mylar foil, (iii) the foil was screened for cells, chromocenters were manually targeted and the first field (typically containing 10 – 100 cells) was irradiated. After successive irradiation of several fields (iv – vi) the chamber was opened at most 30 min after sealing (vii) and cells were subsequently fixed using 2% formaldehyde (viii). Depending on the duration between irradiation and fixation different post-irradiation time points can be monitored within a single sample.

### 7.3 Results and discussion

We first applied ion irradiation at low angle as previously described (Jakob *et al.* 2003) to produce streak-shaped damage patterns corresponding to the linear tracks of heavy ions across cell nuclei. These damage streaks allowed the reconstruction of the initial linear particle trajectories representing the primary sites of damage induction. We used human HeLa tumor cells stably expressing a green fluorescent protein (GFP)-tagged histone H2B to directly visualize chromatin density and immunostained for  $\gamma$ H2AX at 15 min after ion exposure. Remarkably, the  $\gamma$ H2AX streaks revealed a deviation from linearity at regions of high chromatin density as shown for perinucleolar heterochromatin (Fig. 7-2a). Considering the linearity of the charged particle path within the cell, this bending of the  $\gamma$ H2AX streak indicated a displacement of the phosphorylated damage site relative to the initially induced DSB location. To confirm this observation in cell nuclei with larger heterochromatic compartments, we next exposed MEF cells to low angle ion irradiation allowing to discriminate ion-hit and non-hit chromocenters. Interestingly, the ion-hit chromocenters frequently showed  $\gamma$ H2AX signals bent around their borders (Fig. 7-2b). Such bending patterns were also observed for the damage response protein XRCC1 (Fig. 7-3). While these patterns are in line with the previously observed exclusion of  $\gamma$ H2AX from heterochromatin, they also suggest a relocation of the damage from the initial induction site in the center of the heterochromatic compartment to its periphery, as the particle path is linear.

The direction of this relocation appears to be random, but can be divided into two main orientations: either perpendicular to the ion traversal (Fig. 7-2c) resulting in a bent pattern, or along the ion trajectory forming an interrupted streak (Fig. 7-2d). Both bent and interrupted streaks represent external  $\gamma$ H2AX signals. However, also internal signals within chromocenters could be found (Fig. 7-2e). The relative frequencies of external and internal  $\gamma$ H2AX signals were analyzed for different time points post-irradiation. At the earliest observation time of 15 min, already  $71\pm 7\%$  of the ion-hit chromocenters showed external signals. Accordingly, only  $29\pm 5\%$  exhibited internal signals (Fig. 7-2e). Thus, 15 min post-irradiation the majority of ion-hit chromocenters already exhibited externalized signals indicating that the relocation of the original damage represents a fast process. Such a small scale relocation would still be in line with previously reported positional stability of DNA lesions (Soutoglou *et al.* 2007; Jakob *et al.* 2009b).

We next analyzed earlier time periods utilizing a recently developed heavy ion microprobe (Heiss *et al.* 2006) that allowed us to directly target the chromocenters for irradiation. The unique submicrometer precision of the in-house system enabled the aimed irradiation of subnuclear compartments like chromocenters (typically  $\sim 1\text{-}2\ \mu\text{m}$  in diameter) with single ions as specified in Figure 7-1a. MEF nuclei were live stained with Hoechst and chromocenters were manually targeted (red crosses in Fig. 7-4a) using a microscope system. Per cell sample multiple fields of view containing up to 100 cells each were selected for ion exposure (Fig. 7-1b). The irradiation of one field took three seconds at most and up to nine fields per sample were successively irradiated with time lags of one to three minutes. Since all cells within a sample were then fixed at once, each field represents a different post-irradiation time point.

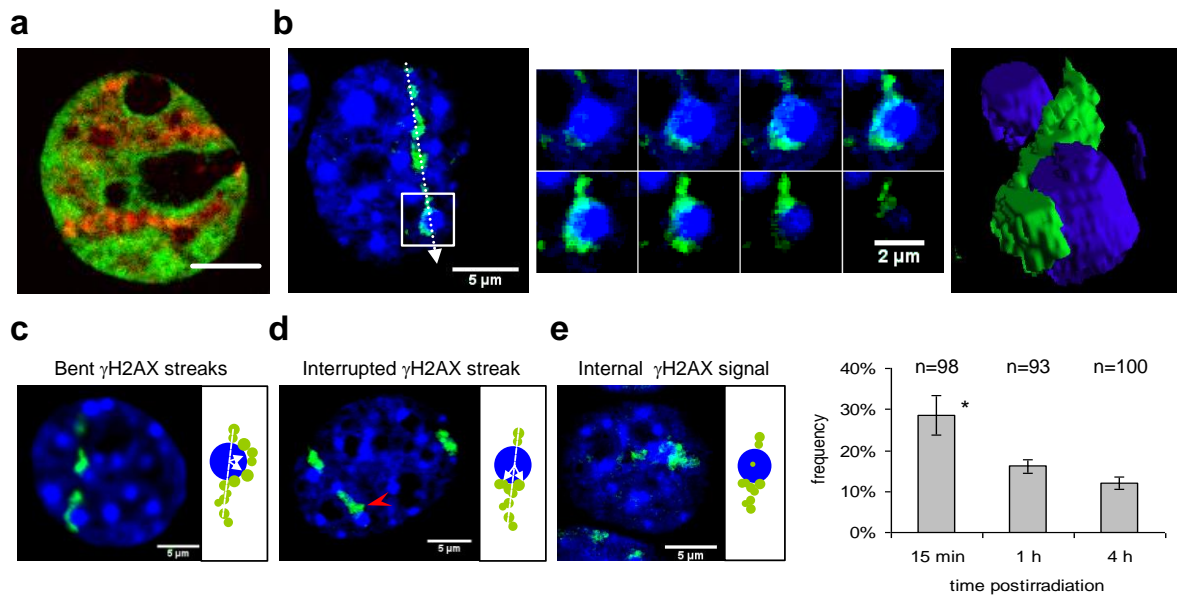


**Fig. 7-2.** Bending of linear ion-induced  $\gamma$ H2AX streaks indicates early chromatin density-dependent damage relocation. (a) HeLa cells expressing GFP-tagged histone H2B were ion-irradiated at low angle and immunostained for  $\gamma$ H2AX after 15 min. Chromatin is visualized by H2B-GFP intensity (green), brighter staining indicating higher density as observed around nucleoli. The depicted linear  $\gamma$ H2AX streaks (red) show a slight but consistent bending following the course of bright perinucleolar chromatin staining. Scale bar: 5  $\mu$ m. (b) Single slice image of a MEF nucleus (left) irradiated with xenon ions to induce linear damage streaks as visualized by  $\gamma$ H2AX immunostaining (green) 1 h post-irradiation. Intense DNA-stained regions (DAPI; blue) represent heterochromatic compartments (chromocenters). The original ion track (arrow) was derived from 3D analysis of the confocal image stack allowing interpolation of the  $\gamma$ H2AX streak and chromocenters traversed by the interpolated trajectory were defined as ion-hit. 3D analysis is exemplarily shown for an ion-hit chromocenter (box) as a montage of different z-planes ( $\Delta = 0.2 \mu$ m, middle panel) and a rendered 3D-image (right). Three different types of  $\gamma$ H2AX patterns, each shown in a MEF nucleus and as a schematic drawing, were observed at ion-hit chromocenters: bent streaks (c), interrupted streaks (d) and internal signals (e, left panel). Bent and interrupted streaks represent external signals, only distinguished by the direction of damage translocation indicated by arrows in the schemes (c and d). The analyzed distribution of the patterns over time post-irradiation is given for internal signals that are complementary to external signals (e, right panel). The probability to find internal  $\gamma$ H2AX signals within ion-hit chromocenters was significantly reduced from 15 min to 1 h post-irradiation ( $p < 0.05$  using t-test; asterisk). Error bars represent the standard error of the mean (SEM) of four independent experiments,  $n$  is the number of analyzed ion-hit chromocenters.

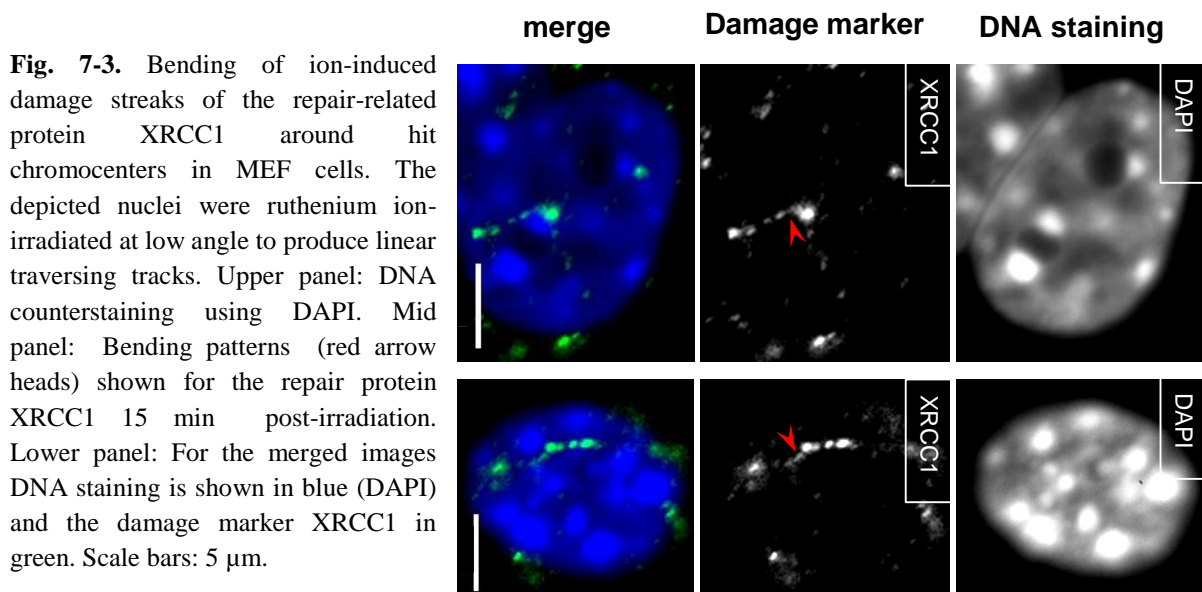


**Fig. 7-3.** Bending of ion-induced damage streaks of the repair-related protein XRCC1 around hit chromocenters in MEF cells. The depicted nuclei were ruthenium ion-irradiated at low angle to produce linear traversing tracks. Upper panel: DNA counterstaining using DAPI. Mid panel: Bending patterns (red arrow heads) shown for the repair protein XRCC1 15 min post-irradiation. Lower panel: For the merged images DNA staining is shown in blue (DAPI) and the damage marker XRCC1 in green. Scale bars: 5  $\mu$ m.

Ion-induced DNA damages were visualized by immunostaining against  $\gamma$ H2AX and XRCC1. Representative light-optical sections of ion-induced  $\gamma$ H2AX and XRCC1 IRIF are shown for samples at 7 and 5 minutes after irradiation of chromocenters with 4.8 MeV/n  $^{197}\text{Au}$ - or  $^{32}\text{S}$ -ions, respectively (Fig. 7-4). Interestingly, XRCC1 signals were indeed detected in the center of targeted chromocenters which co-localized with  $\gamma$ H2AX (Fig. 7-4a) or ATMpS1981, the activated form of ATM (Bakkenist & Kastan 2003) (p-ATM, Fig. 7-4b). Hence, in contrast to the widely held view,  $\gamma$ H2AX signals exist within heterochromatin compartments at early times post-irradiation. This response is clearly not restricted to late S-phase, as previously reported for MCF7 cells in connection with a replication-related opening of the chromatin increasing its accessibility to repair factors (Cowell *et al.* 2007). Thus damage response proteins appear to be generally able to access even highly compacted chromatin regions, contrary to previous assumptions (Cowell *et al.* 2007; Goodarzi *et al.* 2009). Supporting the notion that accessibility is not precluded in heterochromatin, a study in NIH 3T3 mouse embryonic fibroblasts demonstrates that dextrans, comparable in size to XRCC1 and the H2AX-phosphorylating kinases ATM and DNA-PKcs can access chromocenters (Bancaud *et al.* 2009).

XRCC1 co-localizes with  $\gamma$ H2AX but forms comparatively smaller IRIF (Bekker-Jensen *et al.* 2006). Due to the smaller IRIF size and the previously reported rapid recruitment of

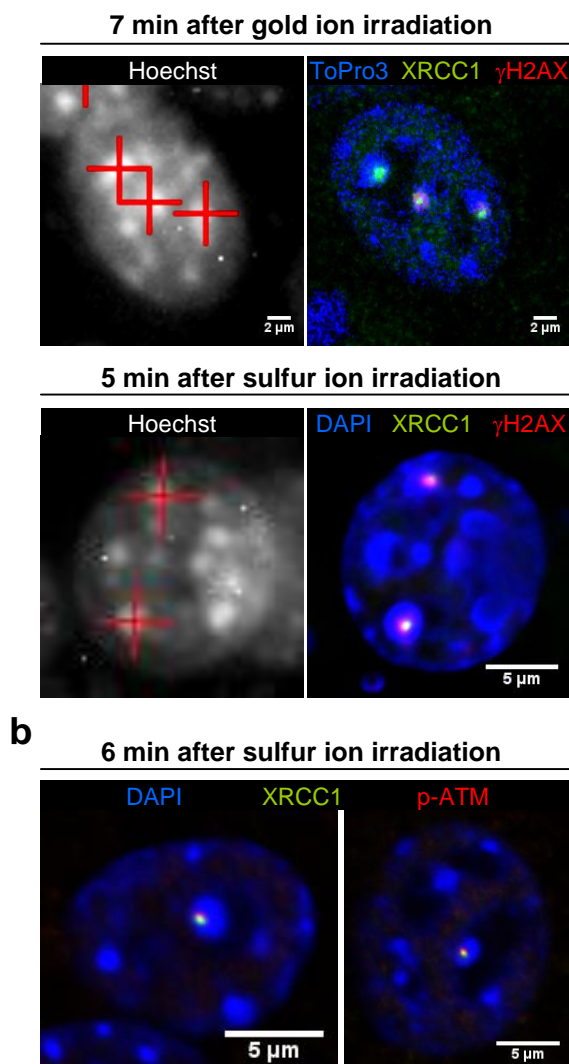


**Fig. 7-4.** H2AX and ATM are phosphorylated and XRCC1 accumulates at damage sites within heterochromatic chromocenters directly after single ion-irradiation. Depicted MEF nuclei were irradiated with single ions of the indicated species and then fixed and immunostained at the given time points post-irradiation. (a) The left-hand images show nuclei of living MEF cells stained with Hoechst 33342 (grey scale) directly before irradiation. Chromocenters are easily visible as regions of bright DNA staining. Red crosses are the target marks for aimed single ion irradiation. The right-hand images show the same nuclei after fixation at the indicated time point post-irradiation and immunostaining. DNA damage-induced foci of the repair factors XRCC1 (green) and  $\gamma$ H2AX (red) are clearly visualized at the sites of ion traversal. Both proteins co-localize within each of the targeted chromocenters. The DNA (blue) was stained using either ToPro3 (upper panel) or DAPI (lower panel). (b) Single ion-hit chromocenter in an irradiated MEF nucleus stained for XRCC1 (green) and p-ATM (red) confirming the damage response within heterochromatin. DNA was stained with DAPI (blue).

XRCC1 to ion-induced damage sites (Tobias *et al.* 2010) this repair protein appeared to be suitable to monitor the expected short range damage relocation at early times post-irradiation. The relative position of a focus was defined by the intensity profile of the surrounding DNA signal. Three different types of XRCC1 focus positions were defined relative to the targeted chromocenter: centrally, intermediately and peripherally located IRIF (Fig. 7-5a). Bending of signal patterns was the recognition feature for initially central ion hits and only these were defined as “completely expelled”. Foci adjacent to chromocenters that did not show bending were considered to be off target (about 60% of all nuclear hits consistent with the microbeam accuracy described by Heiss *et al.* 2006). The relative frequency of each position was calculated for the first 20 minutes following single ion irradiation and the data were pooled in three time intervals (Fig. 7-5b). The fraction of ion-hit chromocenters with centrally located XRCC1 signals decreased from  $28\pm 8\%$  at 3-8 min post-irradiation to  $8\pm 5\%$  for the time period of 9-13 min and to  $\sim 2\%$  for the latest time interval from 14-20 min (Fig. 7-5b). This significant time-dependent reduction of centrally located foci clearly demonstrates the dynamic relocation. Accordingly, within the same time period of 20 min, the relative frequency of peripheral IRIF increased from  $34\pm 3\%$  to  $70\pm 4\%$  (Fig. 7-5b). These data clearly show that XRCC1 signals initially located in the center are expelled to the chromocenters' border within the first 20 minutes following irradiation.

Even in the earliest period (3-8 min), centrally and intermediately located XRCC1 signals represented only 66% of the ion-hit chromocenters (Fig. 7-5b) indicating that the dynamic process of damage relocation had already affected the position of the damage site at these early time points. At later times (14-20 min) these signals were less frequently observed ( $\sim 30\%$ ) consistent with the frequency of internal signals found 15 min after low angle ion irradiation (Fig. 7-2e).

The described relocation process appears to be almost completed one hour after damage induction, because no significant differences in the frequency of measured internal  $\gamma$ H2AX signals could be found between 1 h (16%) and 4 h (12%) post-irradiation (Fig. 7-2e). The mainly external localization of  $\gamma$ H2AX signals observed in our study agrees with previous measurements using sparsely ionizing radiation [15 min (Falk *et al.* 2008), 30 min (Cowell *et al.* 2007; Falk *et al.* 2008; Noon *et al.* 2010) or 1 h (Vasireddy *et al.* 2009; Noon *et al.* 2010) post-irradiation] or after 1 h treatment with neocarzinostatin (Kim *et al.* 2007). Following irradiation with 1 GeV/u  $^{56}\text{Fe}$ -ions Costes *et al.* (2007) described a significantly preferred localization of IRIF at the border of intensively stained DNA regions that was suggestive of a small range translocation of the damage sites (Costes *et al.* 2007). In the present study we provide direct experimental evidence for a chromatin density-dependent relocation process that explains these previous observations.

We presumed that the internal  $\gamma$ H2AX signals observed even hours after irradiation might correspond to parts of the  $\gamma$ H2AX stained domain flanking the actual break sites [about one Mbp up- and down-stream (Rogakou *et al.* 1998; Nakamura *et al.* 2010)]. To address this possibility, we compared the relative positions of co-localizing XRCC1 and  $\gamma$ H2AX signals. We frequently observed that although XRCC1 was clearly expelled from the chromocenter, the  $\gamma$ H2AX signal was present over an extended area ranging from the middle of the chromocenter, where irradiation occurred, to its periphery, where the DSBs were expelled,

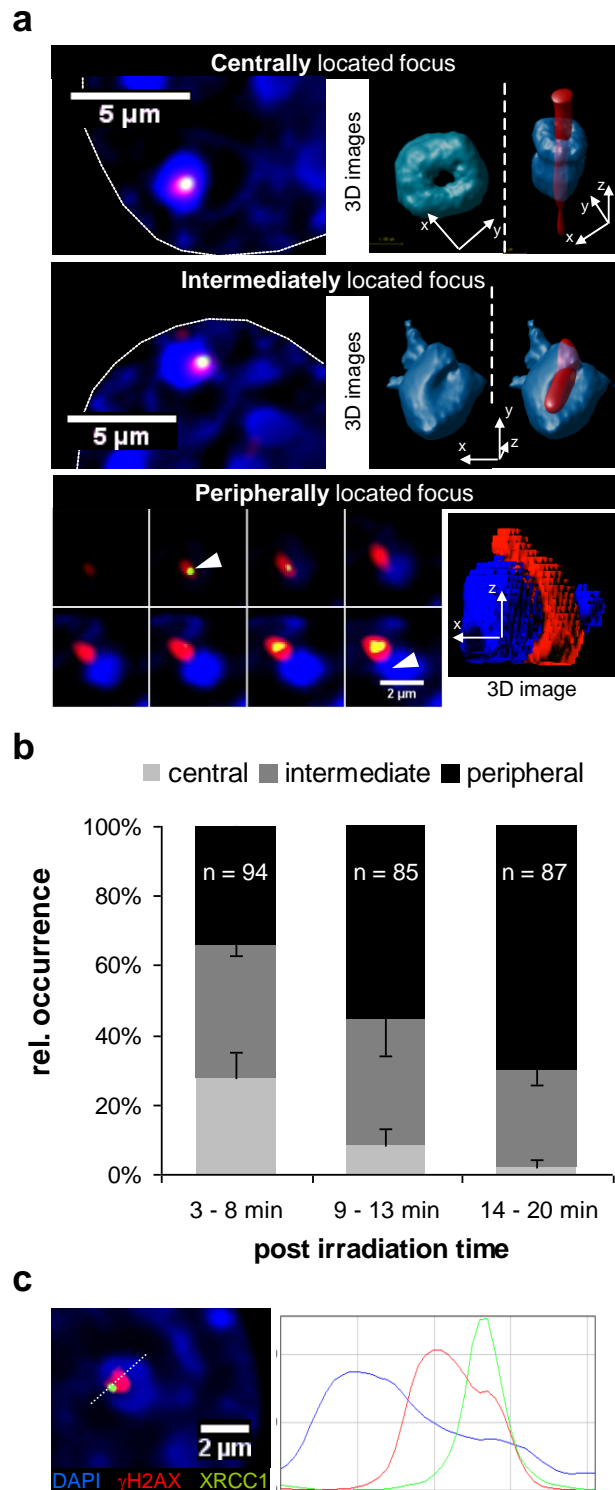


**Fig. 7-5.** Relocalization dynamics of damage sites centrally induced within chromocenters. **(a)** Definition of different radiation-induced foci positions relative to the ion-hit chromocenter. The depicted MEF chromocenters were stained for XRCC1 (green),  $\gamma$ H2AX (red) and DNA counterstained with DAPI (blue) at 5-7 min after microprobe irradiation. Upper panel: Co-localizing XRCC1 and  $\gamma$ H2AX IRIF are centrally located within a chromocenter as illustrated in the projection (left) and rendered surface images (right). Mid panel: Co-localizing XRCC1 and  $\gamma$ H2AX IRIF are located off-centered within the chromocenter (rendered surface images, right) defining the IRIF as intermediately located. Lower panels: Gallery of consecutive light-optical sections ( $\Delta = 0.2 \mu\text{m}$ ) showing the xy position of the damage sites marked by XRCC1 and  $\gamma$ H2AX foci. Arrow heads (frames 2 and 8) determine the initial positions of the damage induced at the ion traversal. The displacement between the damage (foci) and its original induction site (arrow head) shown in frame 8 demonstrates the relocation of the damage from the center to the periphery of the chromocenter. The resulting bending of the  $\gamma$ H2AX signal surrounding the chromocenter is additionally shown in a rendered 3D image. **(b)** Analysis of the time-dependent localization of XRCC1 and  $\gamma$ H2AX IRIF (positions defined in **a**) relative to single ion-targeted chromocenters. Relative frequencies are given for the indicated post-irradiation periods. For each interval the total number of ion-hit chromocenters from three independent experiments is indicated. Error bars represent the SEM. **(c)**  $\gamma$ H2AX signaling appears to pursue the relocation of the XRCC1-marked damage site. The depicted MEF nucleus (left) was fixed 16 min after ion hitting and stained for XRCC1 (green),  $\gamma$ H2AX (red) and counterstained with DAPI (blue). The XRCC1 focus appears expelled, whereas the  $\gamma$ H2AX signal ranges from the center to the periphery of the chromocenter with the  $\gamma$ H2AX intensity peak located between the XRCC1 peak and the center of the chromocenter as shown in the intensity profile (right) along the dotted line.

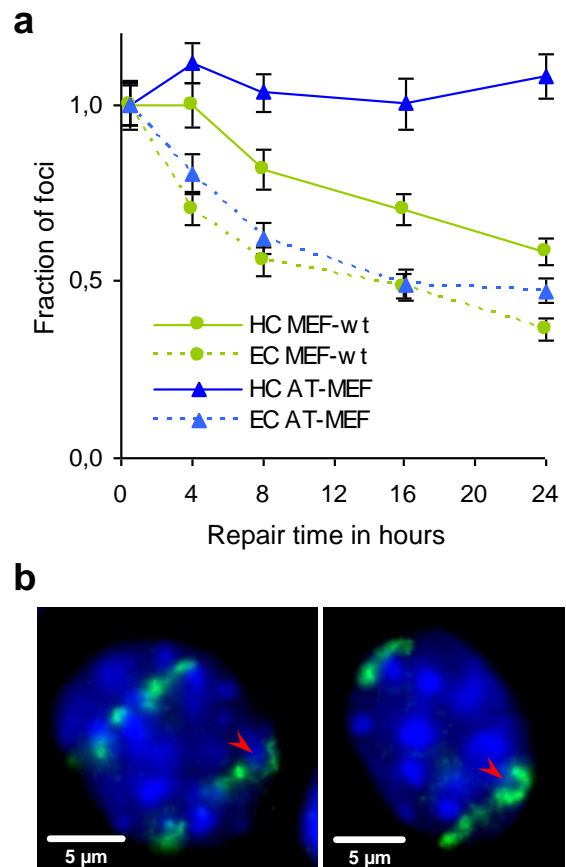
thus suggesting that remaining internal  $\gamma$ H2AX signals reflect chromatin regions adjacent to the break sites extending into the interior of a chromocenter.

To gain mechanistic insight into this dynamic process we next addressed the consequences underlying DSB movement from the interior to the periphery of a chromocenter. It was recently described that following  $\gamma$ -irradiation of normal human fibroblasts and MEFs, DSBs associated with heterochromatic (Noon *et al.* 2010) or gene-poor pericentromeric regions

(Falk *et al.* 2008) and chromocenters (Goodarzi *et al.* 2008) are repaired with slower kinetics than DSBs in euchromatic DNA. Moreover, repair of these breaks requires the concerted action of ATM and the mediator proteins, 53BP1, MDC1, and RNF8/168, to phosphorylate and inactivate the heterochromatin building factor, KAP-1 (Goodarzi *et al.* 2008; Noon *et al.* 2010). In light of our finding that DSBs associated with heterochromatin at later times (>15 min) post irradiation represent breaks which were mainly induced inside heterochromatic regions and expelled to their periphery, we tested whether these breaks are also repaired in an ATM-dependent manner and with slower kinetics than euchromatic DSBs, similar to the observations after  $\gamma$ -irradiation. For this, we used the low angle irradiation set-up allowing the visualization and enumeration of individual foci along the damage streaks.

We sub-divided  $^{12}\text{C}$ -ion-induced IRIFs into chromocenter- and euchromatin-associated foci in MEFs and assessed DSB repair kinetics in these distinct chromatin compartments (Fig. 7-6a). Euchromatin-associated foci were repaired with kinetics similar to the repair of DSBs in normal human fibroblasts following heavy ion irradiation with comparable lesion density (Asaithamby *et al.* 2008). In contrast, repair of chromocenter-associated DSBs was significantly slower during the first 4 h post-irradiation. Similar results were obtained using a slightly modified evaluation based on measuring the length of the streak-shaped  $\gamma\text{H2AX}$  signals associated with chromocenters instead of counting IRIF (Fig. 7-7). At later time points, no significant difference in the repair kinetics of euchromatin- and chromocenter-associated DSBs was observed. We also analyzed  $\text{ATM}^{-/-}$  MEFs and obtained repair kinetics for euchromatic DSBs similar to those of wt-MEFs (Fig. 7-6a). Strikingly, however,  $\text{ATM}^{-/-}$

**Fig. 7-6.** Chromatin-density and absence of ATM influence the repair kinetics of carbon ion-induced DSBs. **(a)** Normalized repair kinetics for  $\gamma\text{H2AX}$  foci following low angle carbon ion irradiation. The number of  $\gamma\text{H2AX}$  foci was enumerated in stationary phase wild-type (green) and  $\text{ATM}^{-/-}$  MEF cells (blue) at the indicated time points after ion exposure. Foci were discriminated to be either associated with the intensively DAPI stained heterochromatic chromocenters (HC) or with euchromatic regions (EC) using software-aided visual inspection. In wild-type MEFs a delayed repair of HC-associated damages is observed for the first 4 h post-irradiation (solid green line), whereas in  $\text{ATM}^{-/-}$  MEFs the repair of HC-associated DSBs is abolished (solid blue line). For each time point  $\sim 30$  nuclei were analyzed. Error bars represent the SEM. **(b)** Depicted  $\text{ATM}^{-/-}$  MEF nuclei were carbon ion irradiated at low angle. Staining for  $\gamma\text{H2AX}$  (green) shows bending patterns around ion-hit chromocenters 30 min post-irradiation. DNA was stained using DAPI (blue).



MEFs showed a complete lack of repair for chromocenter-associated foci indicating that ATM is required for the repair of those DSBs that were induced by 9.2 MeV/n carbon ions inside heterochromatic compartments and subsequently expelled to the periphery of the chromocenters. Thus, it is likely that also DSBs induced by  $\gamma$ -irradiation which localize adjacent to heterochromatic regions and require ATM for repair (Goodarzi *et al.* 2008) represent breaks that were induced inside heterochromatic regions and then expelled. Since ATM's function during heterochromatic DSB repair involves the inactivation of the heterochromatin building factor, KAP-1 (Goodarzi *et al.* 2008; Ziv *et al.* 2006), we tested if ATM knock-out cells show alterations in the relocation of heterochromatin-associated DSBs. As an indicator for this process we used the bending of  $\gamma$ H2AX signals around chromocenters following irradiation with linear tracks of carbon ions. Bent signal patterns similar to those of wt-MEFs were clearly observed 30 min after damage induction in ATM<sup>-/-</sup> MEFs suggesting that the relocation process during heterochromatic DSB repair is largely independent of ATM (Fig. 7-6c).

Taken together, our studies uncover that the DSBs repaired in an ATM-dependent manner are those expelled from the interior to the periphery of heterochromatic regions. The relocation process does not appear to require ATM, but in the absence of ATM these breaks remain unrepaired at the periphery of heterochromatic regions. Since cells deficient in 53BP1, MDC1 and RNF8/168 also exhibit unrepaired DSBs in the periphery of heterochromatic regions (Noon *et al.* 2010), it is likely that these mediators of the ATM signaling response are equally dispensable for the relocation process. It is, however, possible that ATM and the signaling mediators are needed during the relocation process to maintain the fine-structure of the chromatin surrounding DSBs, a function which might be necessary for the repair of these lesions. Such a model would be consistent with ATM's role in regulating KAP-1 during chromatin remodeling (Ziv *et al.* 2006).

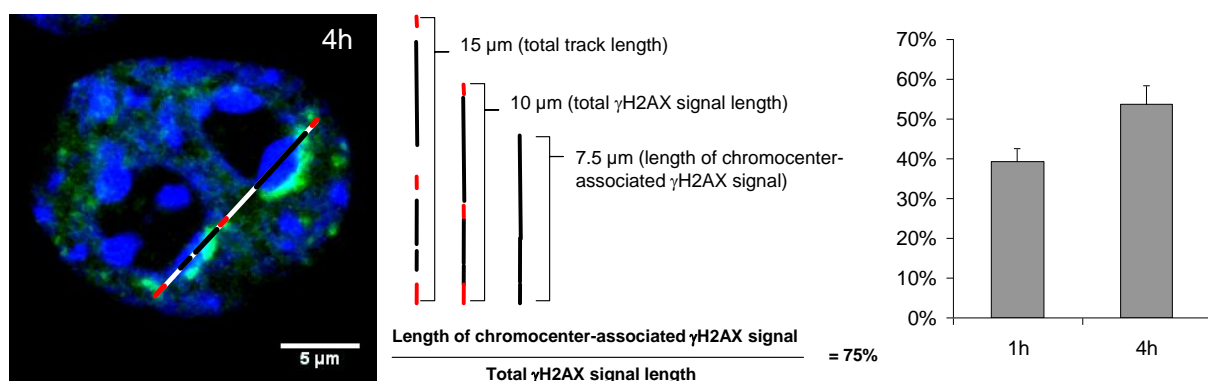


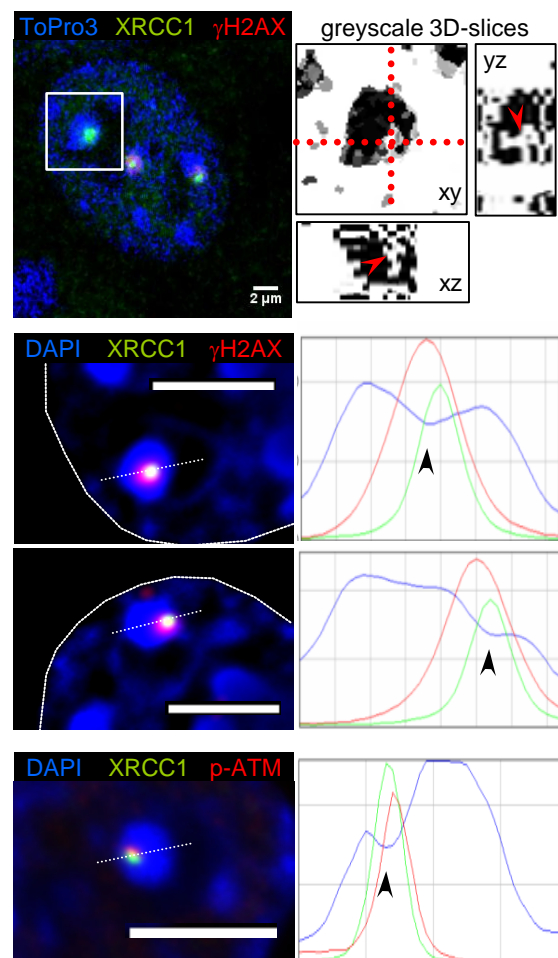
**Fig. 7-7.** Chromocenter- and euchromatin-associated DNA damages exhibit differential repair kinetics. The depicted MEF nucleus was traversed by a high energy xenon ion. DNA is stained with ToPro3 (blue) and the damage marker  $\gamma$ H2AX is shown as green signal 4 h post-irradiation. The ion trajectory is indicated by a white line interrupted by black and red sections indicating chromocenter- and euchromatin-associated fractions of the visible streak signal, respectively. The corresponding lengths of the total track (15  $\mu$ m), the visible  $\gamma$ H2AX streak (10  $\mu$ m) and the chromocenter-associated section (7.5  $\mu$ m) are also visualized. For the depicted nucleus the chromocenter-associated streak fraction (75%) was exemplarily calculated. The mean fraction of  $\gamma$ H2AX streak lengths associated to chromocenters increased from 1h to 4h post-irradiation indicating that chromocenter-associated  $\gamma$ H2AX signals persisted longer compared to euchromatic signals in the analyzed time interval.



We next aimed to shed light on the forces responsible for lesion movement in heterochromatic DNA. A recent study by Kruhlak *et al.* using UVA laser microirradiation reported a damage-induced locally confined chromatin decondensation (Kruhlak *et al.* 2006) presumably creating significant alterations in the balance of physical forces inside a confined heterochromatic compartment. The authors also showed that the monitored decondensation was independent of ATM and  $\gamma$ H2AX (Kruhlak *et al.* 2006). A local chromatin decondensation appearing as a protrusion of damage signals into lower density chromatin was also described after exposure of human cells to  $\gamma$ -rays (Falk *et al.* 2007). In this study decreased chromatin staining intensities were related to changes in histone modifications although without defining heterochromatic regions. To directly assess damage-induced chromatin structure alterations we analyzed the DNA staining patterns after ion irradiation and observed significantly depleted ToPro3 or DAPI signals at the sites of ion hits (Fig. 7-8) suggesting that local decondensation of the chromatin does indeed occur. Furthermore, signal depletion was observed both at centrally and intermediately located IRIF (Fig. 7-5c and Fig. 7-8) indicating that the decondensed chromatin regions also relocated from the interior to the periphery of ion-hit chromocenters. We hypothesize that a configuration of less condensed chromatin enclosed by highly compacted heterochromatin is energetically disadvantageous, and the resulting net forces could drive the relocation process.

Such forces would also explain the observed concerted relocation of multiple nearby DSBs. Although several DSBs are expected to be induced within a single chromocenter (e.g.

**Fig. 7-8.** DNA staining is depleted at damage sites within heterochromatic compartments. Depicted are chromocenters (corresponding to the MEF nuclei shown in Fig. 7-4) immunostained 5-7 min after targeted irradiations with single ions as indicated. Upper panel: 3D analysis of an ion-hit chromocenter (box) showing depleted DNA staining along the whole ion traversal (red arrows within the binary threshold 3D-slice images; red dotted lines indicate the positions of the depicted xz- and yz-plane). Mid and lower panel: Intensity profiles measured along the respective dotted lines in single slice images of ion-irradiated chromocenters confirm that DNA staining (blue) is depleted (black arrows) at the damage site marked by XRCC1 (green) and  $\gamma$ H2AX or p-ATM (red). Note that independent of the DNA stain (ToPro3 or DAPI) and the ion species (gold (upper panel) or sulfur ions (lower three panels)) a depletion in the DNA staining intensity clearly co-localizes with the damage markers. All scale bars: 5  $\mu$ m.



~20 DSBs after sulfur ion irradiation; calculated as described by Jakob *et al.* 2003) these damages jointly relocate to form the bent damage patterns. Damage patterns representing a differential relocation of the individual lesions, such as halo signals completely surrounding the ion-hit compartments, were extremely rare (1 out of 266 analyzed ion-hit chromocenters). Further support for a physically-driven relocation arises from a recent study indicating that entropic forces resulting from the self-governed biophysical process of macromolecular crowding can promote and stabilize self-organization of chromocenters at low cellular energy costs and without the need for discrete boundaries such as membranes (Bancaud *et al.* 2009).

In conclusion, we have utilized single-ion irradiation allowing the localized induction of DSBs within chromocenters and have shown that these lesions, in contrast to the common belief, induce phosphorylation of H2AX and recruitment of repair proteins within highly compacted heterochromatin. Strikingly, we describe a relocation process of damaged sites from the center to the periphery of irradiated chromocenters within ~20 min post-irradiation. This relocation process does not require the DSB signaling factor ATM. However, DSBs relocated from the center to the periphery of heterochromatic regions remain unrepaired in ATM knock-out cells, suggesting that ATM and its associated signaling mediators are required to maintain the chromatin structure during the relocation process. Finally, we demonstrate the local decondensation of chromatin at the sites of ion hits potentially creating the driving physical force underlying lesion movement in heterochromatin.

## Bibliography

- Asaithamby A, Uematsu N, Chatterjee A, Story MD, Burma S and Chen DJ (2008) Repair of HZE-particle-induced DNA double-strand breaks in normal human fibroblasts. *Radiat Res* **169**:437-446.
- Aten JA, Stap J, Krawczyk PM, Van Oven CH, Hoebe RA, Essers J and Kanaar R (2004) Dynamics of DNA double-strand breaks revealed by clustering of damaged chromosome domains. *Science* **303**:92-95.
- Bakkenist CJ and Kastan MB (2003) DNA damage activates ATM through intermolecular autophosphorylation and dimer dissociation. *Nature* **421**:499-506.
- Ballarini F, Alloni D, Facoetti A, Ottolenghi A (2008) Heavy-ion effects: from track structure to DNA and chromosome damage. *New J Phys* **10**:075008.
- Bancaud A, Huet S, Daigle N, Mozziconacci J, Beaudouin J and Ellenberg J (2009) Molecular crowding affects diffusion and binding of nuclear proteins in heterochromatin and reveals the fractal organization of chromatin. *EMBO J*. **28**:3785-3798.
- Bannister AJ, Zegerman P, Partridge JF, Miska EA, Thomas JO, Allshire RC & Kouzarides T (2001) Selective recognition of methylated lysine 9 on histone H3 by the HP1 chromo domain. *Nature* **410**:120-124.
- Barkas, WH. (ed.): Nuclear research emulsions (vol I) (Academic Press, New York, 1963).
- Bassing CH, Chua KF, Sekiguchi J, Suh H, Whitlow SR, Fleming JC, Monroe BC, Ciccone DN, Yan C, Vlasakova K, Livingston DM, Ferguson DO, Scully R and Alt FW.(2002) Increased ionizing radiation sensitivity and genomic instability in the absence of histone H2AX. *Proc. Natl. Acad. Sci. U S A* **99**:8173-8178.
- Bekker-Jensen S, Lukas C, Melander F, Bartek J, Lukas J (2005) Dynamic assembly and sustained retention of 53BP1 at the sites of DNA damage are controlled by Mdc1/NFBD1. *J Cell Biol* **170**:201-211.
- Bekker-Jensen S, Lukas C, Kitagawa R, Melander F, Kastan MB, Bartek J and Lukas J (2006) Spatial organization of the mammalian genome surveillance machinery in response to DNA strand breaks. *J. Cell Biol.* **173**:195-206.
- Berns MW, Wang Z, Dunn A, Wallace V and Venugopalan V (2000) Gene inactivation by multiphoton-targeted photochemistry. *Proc. Natl. Acad. Sci. U S A* **97**:9504-9507.
- Bethe, HA (1930) Zur Theorie des Durchgangs schneller Korpuskularstrahlung durch Materie. *Ann. Phys.* **5**:325.
- Bewersdorf J, Bennett BT and Knight KL (2006) H2AX chromatin structures and their response to DNA damage revealed by 4Pi microscopy. *Proc. Natl. Acad. Sci. U S A* **103**:18137-18142.
- Bloch, F (1933) Stopping power of mater for swiftly moving charged particles. *Ann. Phys.* **16**: 287.
- de Boeck G, Forsyth RG, Praet M and Hogendoorn PCW (2008) Telomere-associated proteins: cross-talk between telomere maintenance and telomere-lengthening mechanisms. *J. Pathol.* **217**:327-344.
- Bornfleth H, Edelmann P, Zink D, Cremer T, Cremer D (1999) Quantitative motion analysis of subchromosomal foci in living cells using four-dimensional microscopy. *Biophys J* **77**:2871-2886.
- van den Bosch M, Bree RT, Lowndes NF (2003) The MRN complex: coordinating and mediating the response to broken chromosomes. *EMBO Rep* **4**:844-849.
- Boyle S, Gilchrist S, Bridger JM, Mahy NL, Ellis JA & Bickmore WA (2001) The spatial organization of human chromosomes within the nuclei of normal and emerin-mutant cells. *Hum. Mol. Genet.* **10**:211-219.
- Bradshaw PS, Stavropoulos DJ and Meyn MS (2005) Human telomeric protein TRF2 associates with genomic double-strand breaks as an early response to DNA damage. *Nat. Genet.* **37**:193-197.
- Branco MR, Pombo A (2007) Chromosome organization: new facts, new models. *Trends Cell Biol* **17**: 127-134.
- Burma S, Chen BP, Murphy M, Kurimasa A and Chen DJ (2001) ATM phosphorylates histone H2AX in response to DNA double-strand breaks. *J. Biol. Chem.* **276**:42462-42467.

- Celeste A, Petersen S, Romanienko PJ, Fernandez-Capetillo O, Chen HT, Sedelnikova OA, Reina-San-Martin B, Coppola V, Meffre E and Nussenzweig A (2002) Genomic instability in mice lacking histone H2AX. *Science* **296**:922–927.
- Celeste A, Fernandez-Capetillo O, Kruhlak MJ, Pilch DR, Staudt DW, Lee A, Bonner RF, Bonner WM and Nussenzweig A (2003) Histone H2AX phosphorylation is dispensable for the initial recognition of DNA breaks. *Nat. Cell Biol.* **5**:675–679.
- Chubb JR, Boyle S, Perry P, Bickmore WA (2002) Chromatin motion is constrained by association with nuclear compartments in human cells. *Curr Biol* **12**:439-445.
- Cornforth MN (1998) Radiation-induced damage and the formation of chromosomal aberrations. In: J.A. Nickoloff and M. Hoekstra, Editors, *DNA Damage and Repair*, Humana Press, NJ, pp. 559–585.
- Cornforth MN, Greulich-Bode KM, Loucas BD, Arsuaga J, Vázquez M, Sachs RK, Brückner M, Molls M, Hahnfeldt P, Hlatky L and Brenner DJ (2002) Chromosomes are predominantly located randomly with respect to each other in interphase human cells. *J Cell Biol* **159**:237-244.
- Cornforth MN (2006) Perspectives on the formation of radiation-induced exchange aberrations. *DNA Repair* **5**: 1182-1191.
- Costes SV, Ponomarev A, Chen JL, Nguyen D, Cucinotta FA and Barcellos-Hoff MH (2007) Image-based modeling reveals dynamic redistribution of DNA damage into nuclear sub-domains. *PLoS Comput Biol* **3**:e155.
- Cowell IG, Sunter NJ, Singh PB, Austin CA, Durkacz BW and Tilby MJ (2007)  $\gamma$ H2AX foci form preferentially in euchromatin after ionising-radiation. *PLoS One* **2**:e1057.
- Cremer T, Kreth G, Koester H, Fink RH, Heintzmann R, Cremer M, Solovei I, Zink D and Cremer C (2000) Chromosome territories, interchromatin domain compartment, and nuclear matrix: an integrated view of the functional nuclear architecture. *Crit. Rev. Eukaryot. Gene Expr.* **10**:179–212.
- Cremer T & Cremer C (2001) Chromosome territories, nuclear architecture and gene regulation in mammalian cells. *Nat. Rev. Genet.* **2**:292-301.
- Cucinotta FA, Durante M (2006) Cancer risk from exposure to galactic cosmic rays: implications for space exploration by human beings. *Lancet Oncol* **7**: 431-435.
- Desai N, Davis E, O'Neill P, Durante M, Cucinotta FA and Wu H (2005) Immunofluorescence detection of clustered gamma-H2AX foci induced by HZE-particle radiation. *Radiat. Res.* **164**:518–522.
- Dimitrova N, Chen YC, Spector DL, de Lange T (2008) 53BP1 promotes non-homologous end joining of telomeres by increasing chromatin mobility. *Nature* **456**:524-528.
- Downs JA, Nussenzweig MC & Nussenzweig A (2007) Chromatin dynamics and the preservation of genetic information. *Nature* **447**:951-958.
- Durante M, Cucinotta FA (2008) Heavy ion carcinogenesis and human space exploration. *Nature Rev Cancer* **8**:465-472.
- Edelmann P, Bornfleth H, Zink D, Cremer T, Cremer C (2001) Morphology and dynamics of chromosome territories in living cells. *Biochim Biophys Acta* **1551**:M29-M39.
- Falk M, Lukasova E, Gabrielova B, Ondrej V, Kozubek S (2007) Chromatin dynamics during DSB repair. *Biochim Biophys Acta* **1773**:1534-1545.
- Falk M, Lukasova E and Kozubek S (2008) Chromatin structure influences the sensitivity of DNA to  $\alpha$ -radiation. *Biochim. Biophys. Acta* **1783**:2398-2414.
- Fernandez-Capetillo O, Celeste A and Nussenzweig A (2003) Focusing on foci: H2AX and the recruitment of DNA-damage response factors. *Cell Cycle* **2**:426–427.
- Ferreira J, Paoletta G, Ramos C & Lamond AI (1997) Spatial organization of large-scale chromatin domains in the nucleus: a magnified view of single chromosome territories. *J. Cell Biol.* **139**:1597-1610.

- Friedberg EC (1995) Out of the shadow and into the light: the emergence of DNA repair. *Trends Biochem. Sci.* **20**:381.
- Friedland W, Paretzke HG, Ballarini F, Ottolenghi A, Kreth G and Cremer C (2008) First steps towards systems radiation biology studies concerned with DNA and chromosome structure within living cells. *Radiat Environ Biophys* **47**:49-61.
- Georgakilas AG (2007) Processing of DNA damage clusters in human cells: current status of knowledge. *Mol. Biosyst.* **4**:30-35.
- Goodarzi AA, Noon AT, Deckbar D, Ziv Y, Shiloh Y, Löbrich M and Jeggo PA (2008) ATM signaling facilitates repair of DNA double-strand breaks associated with heterochromatin. *Mol. Cell* **31**:167-177.
- Goodarzi AA, Noon AT and Jeggo PA (2009) The impact of heterochromatin on DSB repair. *Biochem. Soc. Trans.* **37**:569-576.
- Görisch SM, Wachsmuth M, Ittrich C, Bacher CP, Rippe K and Lichter P (2004) Nuclear body movement is determined by chromatin accessibility and dynamics. *Proc Natl Acad Sci USA* **101**:13221-13226.
- Goodhead DT (1994) Initial events in the cellular effects of ionizing radiations: clustered damage in DNA. *Int. J. Radiat. Biol.* **65**:7-17.
- Grigaravicius P, Rapp A and Greulich KO (2009) A direct view by immunofluorescent comet assay (IFCA) of DNA damage induced by nicking and cutting enzymes, ionizing <sup>137</sup>Cs radiation, UV-A laser microbeam irradiation and the radiometric drug bleomycin. *Mutagenesis* **24**:191-197.
- Guenatri M, Bailly D, Maison C and Almouzni G (2004) Mouse centric and pericentric satellite repeats form distinct functional heterochromatin. *J. Cell Biol.* **166**:493-505.
- Gueven N, Becherel OJ, Kijas AW, Chen P, Howe O, Rudolph JH, Gatti R, Date H, Onodera O, Taucher-Scholz G and Lavin MF (2004) Aprataxin, a novel protein that protects against genotoxic stress. *Hum Mol Genet* **13**:1081-1093.
- Haince JF, McDonald D, Rodrigue A, Déry U, Masson JY, Hendzel MJ and Poirier GG (2008) PARP-1-dependent kinetics of recruitment of MRE11 and NBS1 proteins to multiple DNA damage sites. *J. Biol. Chem.* **283**:1197-1208.
- Heiss M, Fischer BE, Jakob B, Fournier C, Becker G and Taucher-Scholz G (2006) Targeted irradiation of mammalian cells using a heavy-ion microprobe. *Radiat. Res.* **165**:231-239.
- Hinz JM, Yamada NA, Salazar EP, Tebbs RS & Thompson LH (2005) Influence of double-strand break repair pathways on radiosensitivity throughout the cell cycle in CHO cells. *DNA Repair (Amst.)* **4**:782-792.
- Hlatky L, Sachs RK, Vazquez M, Cornforth MN (2002) Radiation-induced chromosome aberrations: insights gained from biophysical modeling. *Bioessays* **24**:714-723.
- Holley WR and Chatterjee A (1996) Clusters of DNA induced by ionizing radiation: formation of short DNA fragments. I. Theoretical modeling. *Radiat. Res.* **145**:188-199.
- Hong Z, Jiang J, Lan L, Nakajima S, Kanno S, Koseki H and Yasui A (2008) A polycomb group protein, PHF1, is involved in the response to DNA double-strand breaks in human cell. *Nucleic Acids Res.* **36**:2939-2947.
- Horn PJ & Peterson CL (2002) Molecular biology. Chromatin higher order folding--wrapping up transcription. *Science* **297**:1824-1827.
- Huyen Y, Zgheib O, DiTullio Jr. RA, Gorgoulis VG, Zaccharatos P, Petty TJ, Sheston EA, Mellert HS, Stavridi ES and Halazonetis TD (2004) Methylated lysine 79 of histone H3 targets 53BP1 to DNA double-strand breaks. *Nature* **432**:406-411.
- Jackson SP (2002) Sensing and repairing DNA double-strand breaks. *Carcinogenesis* **23**:687-696.
- Jakob B, Scholz M and Taucher-Scholz G (2002) Characterization of CDKN1A (p21) binding to sites of heavy-ion-induced damage: colocalization with proteins involved in DNA repair. *Int. J. Radiat. Biol.* **78**:75-88.

- Jakob B, Scholz M and Taucher-Scholz G (2003) Biological imaging of heavy charged-particle tracks. *Radiat. Res.* **159**:676-684.
- Jakob B, Rudolph JH, Gueven N, Lavin MF and Taucher-Scholz G (2005) Live cell imaging of heavy-ion-induced radiation responses by beamline microscopy. *Radiat. Res.* **163**:681-690.
- Jakob B and Taucher-Scholz G (2005) Interaction of heavy ions with nuclear chromatin: Spatitemporal investigations of biological response in a cellular environment. *Nucl. Instrum. Methods Phys. Res. B* **245**:292-297.
- Jakob B, Splinter J and Taucher-Scholz G (2009a) Positional stability of damaged chromatin domains along radiation tracks in mammalian cells. *Radiat. Res.* **171**:405-418.
- Jakob B, Splinter J, Durante M and Taucher-Scholz G (2009b) Live cell microscopy analysis of radiation-induced DNA double-strand break motion. *Proc. Natl. Acad. Sci. U S A* **106**:3172-3177.
- Jenner TJ, Fulford J & O'Neill P (2001) Contribution of base lesions to radiation-induced clustered DNA damage: implication for models of radiation response. *Radiat. Res.* **156**:590-593.
- Jowsey P, Morrice NA, Hastie CJ, McLauchlan H, Toth R and Rouse J (2007) Characterisation of the sites of DNA damage-induced 53BP1 phosphorylation catalysed by ATM and ATR. *DNA Repair* **6**:1536-1544.
- Kegel P, Riballo E, Kühne M, Jeggo PA and Löbrich M (2007) Xirradiation of cells on glass slides has a dose doubling impact. *DNA Repair (Amst.)* **6**:1692-1697.
- Karlsson KH and Stenerlöv B (2004) Focus formation of DNA repair proteins in normal and repair-deficient cells irradiated with high-LET ions. *Radiat. Res.* **161**:517-527.
- Kim C, Snyder RO and Wold MS (1992) Binding properties of Replication Protein A from human and yeast cells. *Mol. Cell. Biol.* **12**:3050-3059.
- Kim J-A, Kruhlak M, Dotiwala F, Nussenzweig A and Haber E (2007) Heterochromatin is refractory to  $\gamma$ -H2AX modification in yeast and mammals. *J. Cell Biol.* **178**:209-218.
- Kong X, Mohanty SK, Stephens J, Heale JT, Gomez-Godinez V, Shi LZ, Kim JS, Yokomori K and Berns MW (2009) Comparative analysis of different laser systems to study cellular responses to DNA damage in mammalian cells. *Nucleic Acids Res.* **37**:e68.
- Krämer M and Kraft G (1994) Calculations of heavy-ion track structure. *Radiat. Environ. Biophys.* **33**:91-109.
- Kraft G, Krämer M and Scholz M (1992) LET, track structure and models. A review. *Radiat. Environ. Biophys.* **31**:161-180.
- Kraft G & Krämer M (1993) Linear energy transfer and track structure. *Adv. Radiat. Biol.* **17**:1-51.
- Kraft G (2000) Tumor therapy with heavy charged particles. *Prog. Part. Nucl. Phys.* **45**:473-544.
- Kruhlak MJ, Celeste A, Dellaire G, Fernandez-Capetillo O, Muller WG, McNally JG, Bazett-Jones DP and Nussenzweig A (2006) Changes in chromatin structure and mobility in living cells at sites of DNA double-strand breaks. *J. Cell Biol.* **172**:823-834.
- Küpper K, Kölbl A, Biener D, Dittrich S, von Hase J, Thormeyer T, Fiegler H, Carter NP, Speicher MR, Cremer T & Cremer M (2007) Radial chromatin positioning is shaped by local gene density, not by gene expression. *Chromosoma*. **116**:285-306.
- Lang M, Engelhardt J and Hell SW (2007) 4Pi microscopy with linear fluorescence excitation. *Opt. Lett.* **32**:259-261.
- Limoli CL and Ward JF (1993) A new method for introducing double-strand breaks into cellular DNA. *Radiat. Res.* **134**:160-169.
- Lisby M, Mortensen UH and Rothstein R (2003) Colocalization of multiple DNA double-strand breaks at a single Rad52 repair centre. *Nat. Cell Biol.* **5**:572-577.
- Lisby M and Rothstein R (2004) DNA damage checkpoint and repair centers. *Curr. Opin. Cell Biol.* **16**:328-334.

- Löbrich M, Cooper PK and Rydberg D (1996) Non-random distribution of DNA double-strand breaks induced by particle irradiation. *Int. J. Radiat. Biol.* **70**:493-503.
- Lukas C, Bartek J, Lukas J (2005) Imaging of protein movement induced by chromosomal breakage: tiny lesions pose great global challenges. *Chromosoma* **114**:146-154.
- Mao Z, Seluanov A, Jiang Y and Gorbunova V (2007) TRF2 is required for repair of nontelomeric DNA double-strand breaks by homologous recombination. *Proc. Natl. Acad. Sci. U S A* **104**:13068-13073.
- Mari PO, Florea BI, Persengiev SP, Verkaik NS, Brüggewirth HT, Modesti M, Giglia-Mari G, Bezstarosti K, Demmers JAA, Luidert TM, Houtsmuller AB, van Gent DC (2006) Dynamic assembly of end-joining complexes requires interaction between Ku70/80 and XRCC4. *Proc. Natl. Acad. Sci. USA* **103**:18597-18602.
- Marshall WF, Straight A, Marko JF, Swedlow J, Dernburg A, Belmont A, Murray AW, Agard DA and Sedat JW (1997) Interphase chromosomes undergo constrained diffusional motion in living cells. *Curr Biol* **7**:930-939.
- Meaburn KJ, Misteli T, Soutoglou E (2007) Spatial genome organization in the formation of chromosomal translocations. *Semin Cancer Biol* **17**:80-90.
- Mearini G, Fackelmayer FO (2006) Local chromatin mobility is independent of transcriptional activity. *Cell Cycle* **5**:1989-1995.
- Meldrum RA, Botchway SW, Wharton CW and Hirst GJ (2003) Nanoscale spatial induction of ultraviolet photoproducts in cellular DNA by three-photon near-infrared absorption. *EMBO Rep.* **4**:1144-1149.
- Mohanty SK, Rapp A, Monajembashi S, Gupta PK and Greulich KO (2002) Comet assay measurements of DNA damage in cells by laser microbeams and trapping beams with wavelengths spanning a range of 308 nm to 1064 nm. *Radiat. Res.* **157**:378-385.
- Mortusevicz O, Rothbauer U, Cardoso MC and Leonhardt H (2006) Differential recruitment of DNA Ligase I and III to DNA repair sites. *Nucleic Acids Res.* **34**:3523-3532.
- Mortusevicz O, Amé JC, Schreiber V and Leonhardt H (2007) Feedback-regulated poly(ADP-ribosylation) by PARP-1 is required for rapid response to DNA damage in living cells. *Nucleic Acids Res.* **35**:7665-7675.
- Nakamura AJ, Rao VA, Pommier Y and Bonner WM (2010) The complexity of phosphorylated H2AX foci formation and DNA repair assembly at DNA double-strand breaks. *Cell Cycle* **9**:Epub ahead of print.
- Nelms BE, Maser RS, MacKay JF, Lagally MG, Petrini JH (1998) In situ visualization of DNA double-strand break repair in human fibroblasts. *Science* **280**:590-592.
- Newman HC, Prise KM & Michael BD (2000) The role of higher-order chromatin structure in the yield and distribution of DNA double-strand breaks in cells irradiated with X-rays or alpha-particles. *Int. J. Radiat. Biol.* **76**:1085-1093.
- Nikiforova MN, Stringer JR, Blough R, Medvedovic M, Fagin JA and Nikiforov YE (2000) Proximity of chromosomal loci that participate in radiation-induced rearrangements in human cells. *Science* **290**: 138-141.
- Noon AT, Shibata A, Rief N, Löbrich M, Stewart GS, Jeggo PA and Goodarzi AA (2010) 53BP1-dependent robust localized KAP-1 phosphorylation is essential for heterochromatic DNA double-strand break repair. *Nat. Cell Biol.* **12**:177-184.
- Paap B, Wilson DM 3rd and Sutherland BM (2008) Human abasic endonuclease action on multilesion abasic clusters: implications for radiation-induced biological damage. *Nucleic Acids Res.* **36**:2717-2727.
- Paull TT, Rogakou EP, Yamazaki V, Kirchgessner CU, Gellert M and Bonner WM (2000) A critical role for histone H2AX in recruitment of repair factors to nuclear foci after DNA damage. *Curr. Biol.* **10**:886-895.
- Peak JG and Peak MJ (1990) Ultraviolet light induces double-strand breaks in DNA of cultured human P3 cells as measured by neutral filter elution. *J. Photochem. Photobiol.* **52**:387-393.
- Prise KM, Ahnström G, Belli M, Carlsson J, Frankenberg D, Kiefer J, Löbrich M, Michael BD, Nygren J, Simone G (1998) A review of DSB induction data for varying quality radiations. *Int. J. Radiat. Biol.* **74**:173-184.

- Rogakou EP, Pilch DR, Orr AH, Ivanova VS and Bonner WM (1998) DNA double-stranded breaks induce histone H2AX phosphorylation on serine 139. *J. Biol. Chem.* **273**:5858–5868.
- Rogakou EP, Boon C, Redon C and Bonner WM (1999) Megabase chromatin domains involved in DNA double-strand breaks in vivo. *J. Cell Biol.* **146**:905-916.
- Rydberg B, Löbrich M & Cooper PK (1994) DNA double-strand breaks induced by high-energy neon and iron ions in human fibroblasts. I. Pulsed-field gel electrophoresis method. *Radiat. Res.* **139**:133-141.
- Rydberg B (1996) Clusters of DNA damage induced by ionizing radiation: formation of short DNA fragments. II. Experimental detection. *Radiat. Res.* **145**:200–209.
- Rydberg B (2001) Radiation-induced DNA damage and chromatin structure. *Acta Oncol.* **40**:682–685.
- Sachs RK, Chen AM, Brenner DJ (1997) Proximity effects in the production of chromosome aberrations by ionizing radiation. *Int J Radiat Biol* **71**:1-19.
- Sancar A, Lindsey-Boltz LA, Unsal-Kacmaz K & Linn S (2004) Molecular mechanisms of mammalian DNA repair and the DNA damage checkpoints. *Annu. Rev. Biochem.* **73**:39-85.
- Sardoni N, Langer S, Fauth C, Bernardi G, Cremer T, Turner BM & Zink D (1999) Nuclear organization of mammalian genomes. Polar chromosome territories build up functionally distinct higher order compartments. *J. Cell Biol.* **146**:1211-1226.
- Sartori AA, Lukas C, Coates J, Mistrik M, Fu S, Bartek J, Baer R, Lukas J and Jackson SP (2007) Human CtIP promotes DNA end resection. *Nature* **450**:509-514.
- Savage JRK (1993) Interchange and intra-nuclear architecture. *Environ Mol Mutagen* **22**:234-244.
- Scholz M, Kellerer AM, Kraft-Weyrather W and Kraft G (1997) Computation of cell survival in heavy ion beams for therapy. *Radiat. Environ. Biophys.* **36**:59-66.
- Schulz-Ertner D, Tsujii H (2007) Particle radiation therapy using proton and heavier ion beams. *J Clin Oncol* **25**:953-964.
- Soutoglou E, Misteli T (2007) Mobility and immobility of chromatin in transcription and genome stability. *Curr Opin Genet Dev* **17**:435-442.
- Soutoglou E, Dorn JF, Sengupta K, Jasin M, Nussenzweig A, Ried T, Danuser G and Misteli T (2007) Positional stability of single doublestrand breaks in mammalian cells. *Nat. Cell Biol.* **9**:675–682.
- Staudt T, Lang M, Medda R, Engelhardt J and Hell SW (2007) 2,2'-Thiodiethanol: a new water soluble mounting medium for high resolution optical microscopy. *Microsc. Res. Tech.* **70**:1-9.
- Stewart GS, Wang B, Bignell CR, Taylor AM and Elledge SJ (2003) MDC1 is a mediator of the mammalian DNA damage checkpoint. *Nature* **421**:961–966.
- Stiff T, O'Driscoll M, Rief N, Iwabuchi K, Löbrich M and Jeggo PA (2004) ATM and DNA-PK function redundantly to phosphorylate H2AX after exposure to ionizing radiation. *Cancer Res.* **64**:2390-2396.
- Sun HB, Shen J & Yokota H (2000) Size-dependent positioning of human chromosomes in interphase nuclei. *Biophys. J.* **79**:184-190.
- Sutherland BM and Griffin KP (1981) Absorption spectrum of DNA for wavelengths greater than 300 nm. *Radiat. Res.* **86**:399-409.
- Sutherland BM, Bennett PV, Sidorkina O and Laval J (2000) Clustered DNA damages induced in isolated DNA and in human cells by low doses of ionizing radiation. *Proc. Natl. Acad. Sci. USA* **97**:103–108.
- Tanaka H, Mendonca MS, Bradshaw PS, Hoelz DJ, Malkas LH, Meyn MS and Gilley D (2005) DNA damage-induced phosphorylation of the human telomere-associated protein TRF2. *Proc. Natl. Acad. Sci. U S A* **102**:15539-15544.
- Tashiro S, Walter J, Shinohara A, Kamada N and Cremer T (2000) Rad51 accumulation at sites of DNA damage and in postreplicative chromatin. *J. Cell Biol.* **150**:283-291.



- Taucher-Scholz G, Heilmann J & Kraft G (1996) Induction and rejoining of DNA double-strand breaks in CHO cells after heavy ion irradiation. *Adv. Space Res.* **81**:83-92.
- Taucher-Scholz G and Jakob B, Ion irradiation as a tool to reveal the spatiotemporal dynamics of DNA damage response processes. In *Genome Integrity* (D. H. Lankenau, Ed.), pp. 453–478. Springer, Berlin, 2006.
- Thévenaz E, Ruttimann UE and Unser M (1998) A pyramid approach to subpixel registration based on intensity. *IEEE Trans. Image Process* **7**:27-41.
- Tobias F, Durante M, Taucher-Scholz G and Jakob B (2009) Spatiotemporal analysis of DNA repair using charged particle radiation. *Mutat. Res.* (epub ahead of print).
- Uematsu N, Weterings E, Yano K, Morotomi-Yano K, Jakob B, Taucher-Scholz G, Mari PO, van Gent DC, Chen BP and Chen DJ (2007) Autophosphorylation of DNA-PKcs regulates its dynamics at DNA double-strand breaks. *J. Cell Biol.* **177**:219-229.
- Vasireddy RS, Karagiannis TC and El-Osta A (2009)  $\gamma$ -radiation-induced  $\gamma$ H2AX formation occurs preferentially in actively transcribed euchromatic loci. *Cell. Mol. Life Sci.* **67**:291-294.
- Vogel A, Lorenz K, Horneffer V, Hüttmann G, von Smolinski D and Gebert A (2007) Mechanisms of laser-induced dissection and transport of histologic specimens. *Biophys. J.* **93**:4481-4500.
- Wang Y, Zhou XY, Wang H, Huq MS and Iliakis G (1999) Roles of Replication Protein A and DNA-dependent Protein Kinase in the regulation of DNA replication following DNA damage. *J. Biol. Chem.* **274**:22060-22064.
- Ward JF (1988) DNA damage produced by ionizing radiation in mammalian cells: identities, mechanisms of formation, and reparability. *Prog. Nucleic Acid Res. Mol. Biol.* **35**:95-125.
- Ward JF (1994) The complexity of DNA damage: relevance to biological consequences. *Int. J. Radiat. Biol.* **66**:427–432.
- Ward JF (1995) Radiation mutagenesis: the initial DNA lesions responsible. *Radiat. Res.* **142**:362-368.
- Ward IM, Minn K, Jorda KG and Chen J (2003) Accumulation of checkpoint protein 53BP1 at DNA breaks involves its binding to phosphorylated histone H2AX. *J. Biol. Chem.* **278**:19579–19582.
- Wiesmeijer K, Krouwels IM, Tanke HJ, Dirks RW (2008) Chromatin movement visualized with photoactivable GFP-labeled histone H4. *Differentiation* **76**:83-90.
- Williams ES, Stap J, Essers J, Ponnaiya B, Luijsterburg MS, Krawczyk PM, Ullrich RL, Aten JA and Bailey SM (2007) DNA double-strand breaks are not sufficient to initiate recruitment of TRF2. *Nat. Genet.* **39**:698-699.
- Wu H, Durante M, Lucas JN (2001) Relationship between radiation-induced aberrations in individual chromosomes and their DNA content: effects of interaction distance. *Int J Radiat Biol* **77**:781-786.
- Zink D & Cremer T (1998) Cell nucleus: chromosome dynamics in nuclei of living cells. *Curr. Biol.* **8**:R321-324.
- Zink D, Fischer AH & Nickerson JA (2004) Nuclear structure in cancer cells. *Nat. Rev. Cancer* **4**:677-687.
- Ziv Y, Bielopolski D, Galanty Y, Lukas C, Taya Y, Schultz DC, Lukas J, Bekker-Jensen S, Bartek J and Shiloh Y (2006) Chromatin relaxation in response to DNA double-strand breaks is modulated by a novel ATM- and KAP-1 dependent pathway. *Nat. Cell Biol.* **8**:870-876.



---

## Curriculum Vitae

### Personal information

#### **Jörn Splinter**

Randweg 29  
64297 Darmstadt  
phone: 06151 4926496  
mobile: 0171 4535694  
email: splinter.joern@web.de

Date of birth: February 27<sup>th</sup>, 1980  
Place of birth: Darmstadt  
Citizenship: german



### Education

Oct. 2000 – Feb. 2007 **Diploma in Physics** at the TU Darmstadt, Germany  
Oct. 2002 – Apr. 2004 **Intermediate Diploma in Genetics** (major at the faculty of biology)  
Aug. 1990 – Jun. 1999 **Abitur** at the Lichtenbergschule Darmstadt, Germany

### Work experience

Mar. 2007 – Feb. 2010 **PhD student** in the department of Biophysics at GSI Helmholtzzentrum for heavy ion research, Darmstadt, Germany  
Mar. 2007 – Dec. 2009 **Temporary job as tour guide** for the Public Relation department of the GSI Helmholtzzentrum  
Oct. 2002 – Jan. 2006 **Student assistant** at the faculty of Physics, TU Darmstadt, Germany

### Languages

**German** first language  
**English** fluent  
**French** elementary

Darmstadt, 15<sup>th</sup> March 2010

---

  
Jörn Splinter

---

## Eidesstattliche Erklärung

Hierdurch erkläre ich an Eides Statt, daß ich bisher noch keinen Promotionsversuch unternommen habe.

Datum: 08.03.2010

.....  


( Unterschrift )